Institutional Repository - Research Portal
Dépôt Institutionnel - Portail de la Recherche
researchportal.unamur.be
University of Namur

THESIS / THÈSE

DOCTOR OF SCIENCES

Non-gravitational and chaotic aspects of dynamics of small Solar System bodies

Murawiecka, Magda

Award date:
2019

Awarding institution:
University of Namur

Link to publication

General rights
Copyright and moral rights for the publications made accessible in the public portal are retained by the authors and/or other copyright owners and it is a condition of accessing publications that users recognise and abide by the legal requirements associated with these rights.

- Users may download and print one copy of any publication from the public portal for the purpose of private study or research.
- You may not further distribute the material or use it for any profit-making activity or commercial gain
- You may freely distribute the URL identifying the publication in the public portal ?

Take down policy
If you believe that this document breaches copyright please contact us providing details, and we will remove access to the work immediately and investigate your claim.

Download date: 05. May. 2023

UNIVERSITÉ DE NAMUR

FACULTÉ DES SCIENCES

DÉPARTEMENT DE MATHÉMATIQUE

Non-gravitational and chaotic aspects of dynamics of small Solar System bodies

Thèse présentée par
Magda Murawiecka
pour l'obtention du grade
de Docteur en Sciences

Composition du Jury :

Sławomir BREITER
Daniel CASANOVA
Daniel HESTROFFER
Anne LEMAITRE (Promoteur)
Anne-Sophie LIBERT (Présidente du Jury)

Septembre 2019

Graphisme de couverture : ©Presses universitaires de Namur
©Presses universitaires de Namur & Magda Murawiecka
Rempart de la Vierge, 13
B-5000 Namur (Belgique)

Toute reproduction d'un extrait quelconque de ce livre,
hors des limites restrictives prévues par la loi,
par quelque procédé que ce soit, et notamment par photocopie ou scanner,
est strictement interdite pour tous pays.

Imprimé en Belgique

ISBN : 978-2-39029-079-7
Dépôt légal : D/2019/1881/30

Les aspects non-gravitationelles and chaotiques dans la dynamique des petites corps du Systeme Solaire

par Magda Murawiecka

Résumé : Cette thèse comprend plusieurs sujets liés au domaine du mouvement orbital des débris spatiaux et de la dynamique rotationnelle des astéroïdes. Les débris spatiaux ont récemment reçu une attention considérable car ils représentent une menace pour les satellites actifs et les missions humaines. Par conséquent, des perturbations de plus en plus petites sont considérées dans les modèles de determination précise de leurs orbites. L'effet thermique Yarkovsky-Schach, développé dans cette thèse, en est un exemple, et des simulations numériques des orbites de débris spatiaux, tenant compte de cet effet, ont été réalisées pour un ensemble pertinent de conditions initiales. L'importance relative de cette force a été mise en évidence sur des échelles de temps très longues. Par ailleurs, ce travail a également considéré le mouvement d'objets en orbite terrestre sous l'influence de résonances tesserales et lunisolaires. Plusieurs cartes de stabilité ont été réalisées grâce à un indicateur de chaos variationnel, le MEGNO, et elles ont été comparées avec celles publiées dans la littérature. Des structures stables, qui apparaissent plus nettement grâce au MEGNO, y ont été identifiées et discutées. Cette étude a permis de détecter et d'étudier un problème lié à l'integration numérique des orbites chaotiques ; en effet, en utilisant un intégrateur numérique avec un pas de temps fixe, plusieurs "observables" ne sont pas calculés de manière correcte, et dépendent clairement du pas choisi, rendant leurs estimations contestables. La dernière partie s'intéresse au problème de la stabilité de la rotation autour de l'axe principal d'inertie pour les astéroïdes soumis à l'effet YORP et à une dissipation d'énergie inélastique. La thèse propose un modèle approximatif décrivant les petits déplacements de l'axe principal dans l'angle de nutation et détermine les conditions à satisfaire pour que l'axe instantané de rotation atteigne un équilibre.

Non-gravitational and chaotic aspects of dynamics of small Solar System bodies

by Magda Murawiecka

Abstract: This thesis has taken on several subjects related to the orbital dynamics of space debris and rotational dynamics of asteroids. Space debris have received a considerable attention in recent years due to the threat they pose to active satellites and manned missions. As a result, smaller and smaller perturbations are taken into account for precise orbit determination. The Yarkovsky-Schach effect is an example of such small perturbation. We have performed numerical simulations with the effect with various initial conditions. The force relative significance is only revealed over long timescales. Furthermore, we also considered the motion of an object under the tesseral and lunisolar resonances. With the application of a variational chaos indicator, MEGNO, several stability maps were constructed and compared with literature. Some stable structures were singled out and discussed. A related problem of numerical integration issues in case of chaotic orbits was also examined. If a numerical integrator with a fixed time step is used, several observables are shown to be

inaccurately computed, and to depend on the chosen time step. Lastly, in case of asteroids, we investigated the question of stability of principal axis rotation under the YORP torque and inelastic energy dissipation. We developed an approximate model for small departures from the principal axis in nutation angle and searched for conditions that should be met so that the instantaneous rotation axis is driven back to the stable position.

Thèse de doctorat en Sciences Mathématiques (Ph.D. thesis in Mathematics)
Date: 10/09/2019
Département de Mathématique
Promoteur (Advisor): Anne LEMAITRE

Acknowledgements

First and foremost, I would like to express my gratitude towards my advisor Anne Lemaitre, for giving me the opportunity to conduct this work, and for her continued support, guidance and kindness during these five years. My deepest appreciation goes to Sławomir Breiter, who was an important mentor over the past years, for his patience and expertise. Our collaboration was a valuable part of this work. I am also very grateful to the remaining members of the jury: Anne-Sophie Libert, Daniel Casanova and Daniel Hestroffer, who accepted to evaluate my work. Their constructive remarks and suggestions helped to improve the quality of this manuscript. Furthermore, I would like to thank my colleagues Benoit Noyelles and Alexis Petit for their considerable help with many issues I encountered in my numerical simulations – I could always count on their cordiality and competence. My collaboration with Jerome Daquin was both rewarding and amicable. I would also like to thank the whole Department of Mathematics for welcoming me in Namur.

I received a lot of encouragement from Antoine, whom I would like to thank for his thoughtfulness and faith in me. Finally, my deep gratitude is due to my family for their constant support, despite the distance between us.

Contents

Introduction

60 years of space exploration has brought forth a multitude of new possibilities and technological advancements, as well as great progress in scientific knowledge. We are now able to determine the Earth gravity field with high precision, whereas placement of the telescopes on orbit has allowed to eliminate the atmospheric effects and to explore new radiation bands. However, the space around the Earth has been consequently filled with pieces of debris, and the process is hard to control. The protection against collisions and impacts require precise knowledge on the multitude of minuscule forces that affect their motion. Some of these forces and phenomenons had already been explored quite thoroughly in the domain of small natural bodies dynamics: asteroids, comets, meteoroids. The uniformity of dynamics of all small bodies allows the transfer of expertise between these domains.

0.1 Space debris

The term "space debris" covers a multitude of objects. Initially referring to natural bodies, like meteoroids, it is mainly used nowadays to describe artificial objects on the orbit around the Earth that serve no function. Quoting ESA Space Debris Office, these objects are classified as follows:

- "Payloads, space object designed to perform specific function in space excluding launch functionality. This includes operational satellites as well as calibration objects.
- Payload mission related objects, space objects released as space debris which served a purpose for the function of a payload. Common examples include covers for optical instruments or astronaut tools.
- Payload fragmentation debris, space objects fragmented or unintentionally released from a payload as space debris for which their genesis can be traced back to a unique event. This class includes objects created when a payload explodes or when it collides with another object.

- Payload debris, space objects fragmented or unintentionally released from a payload as space debris for which the genesis is unclear but orbital or physical properties enable a correlation with a source.
- Rocket body, space object designed to perform launch related functionality; This includes the various orbital stages of launch vehicles, but not payloads which release smaller payloads themselves.
- Rocket mission related objects (RM), space objects intentionally released as space debris which served a purpose for the function of a rocket body. Common examples include shrouds and engines.
- Rocket fragmentation debris, space objects fragmented or unintentionally released from a rocket body as space debris for which their genesis can be traced back to a unique event. This class includes objects created when a launch vehicle explodes.
- Rocket debris, space objects fragmented or unintentionally released from a rocket body as space debris for which the genesis is unclear but orbital or physical properties enable a correlation with a source."

(ESA, b). The very beginning of space exploration is also the beginning of accumulation of space debris. The fourth man-made object that was sent in space, Vanguard 1 launched from Cape Canaveral on March 17, 1958, remains on its orbit to this date, along with upper stage of its launch vehicle, and is expected to stay there for at least 200 more years (NASA, a). Together with two other Vanguard satellites, launched in 1959, they remain the oldest artificial objects orbiting the Earth. Since then, the number of debris has only grown. In June 1961, the first unintended explosion in space created almost 300 pieces of debris when Ablestar launch vehicle blew up after deploying its payload (Portree and Loftus Jr, 1999). The tests of anti-satellite systems (ASAT in short) conducted by the Soviet Union between 1968 and 1982 created about 700 pieces of debris big enough to be tracked, almost half of which still remain in orbit. The US ASAT test in 1985 created thousands of debris, although due to low altitude of target object, they have already burnt in the atmosphere (Portree and Loftus Jr, 1999). In 2007, China conducted an anti-satellite missile test by shooting down a defunct weather satellite, Fengyun 1C, on a Sun-synchronous orbit at an altitude of around 850 km. The collision led to the biggest single-event space debris creation in history, resulting in at least 4 000 pieces of trackable size, half of which still remain in orbit, and an estimated 40 000 smaller debris particles (Lambert, 2018). They quickly spread around the satellite original orbit, and over time, they also scattered in altitude, ranging from around 700 km up to 3000 km. In 2009, the high velocity collision between an active US commercial satellite Iridium 33 and a defunct Soviet Kosmos-2251 satellite created almost 1 900 pieces of debris. Some of them already decayed and burnt in the atmosphere, but most of Iridium fragments is expected to stay on orbit for at least 100 years, while Kosmos pieces should be gone in 10-20 years (Weeden, 2010). Tracking these fragments revealed a much greater dispersion of Kosmos fragments than expected, showing that the methods put in work are still inaccurate. In

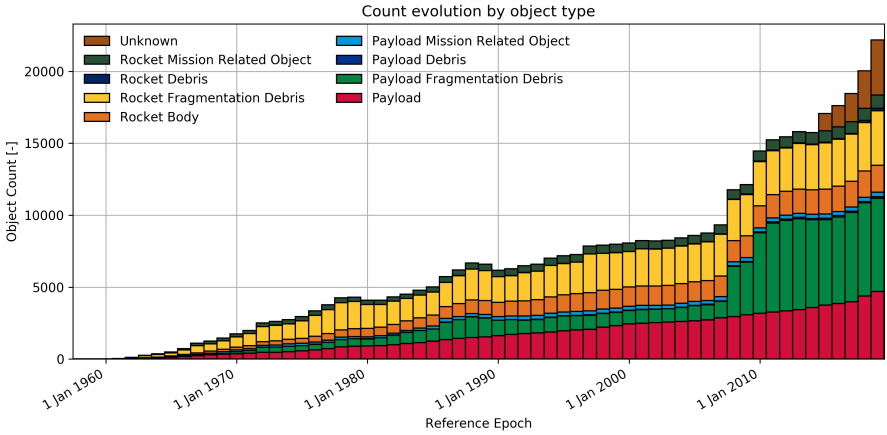

Figure 0.1 – Space debris population since 1960. One can see that the majority of debris are defunct satellites and tools, the products of their fragmentation, or products of rocket transformation. In recent years, the ”unknown” category has emerged to contain all the objects of unkown characteristics. *Image credit: ESA*

2012, Russian Briz-M upper stage exploded on-orbit, creating almost a hundred pieces of debris on an eccentric orbits, crossing the ISS orbit (Celestrak). An explosion of an US weather satellite, DMSP-F13, in 2015 created around a hundred small and over 50 000 milimeter-size pieces (Space.com, a). As recently as in March this year, an Indian ASAT test created around 400 trackable debris on low orbits (Space.com, b). Since 1961, around 290 in-orbit explosions took place, creating more than 750 000 pieces of debris larger than 1 cm (ESA, d). The main cause is the fuel or other energy sources left in rocket stages or satellites. During many manned missions to ISS, various objects were lost in space, e.g. tools, or even a Hasselblad camera. Droplets of fuel or flakes of paint, detached from old satellites surface due to its erosion by micro particles, are among the most numerous pieces of debris. Rocket bodies and upper stages were commonly left in space after they served their purpose. Fig. 0.1 summarizes the growth of space debris population since the beginning of the space age.

In an attempt to control the population, various space debris catalogues have been established. Since the appearance of Sputnik on the night sky, the US Department of Defense has maintained a catalogue of all man-made objects on the orbit around the Earth. NASA maintains a civilian database of orbital elements in the format of two-line elements set (TLE). These catalogues allow to predict and possibly prevent future collisions or atmospheric re-entries. Many laws and measures were also set up through the years. For example, after the 1996 explosion of HAPS upper stage rocket that produced around 700 pieces of debris and was caused by excess fuel left in the tank, a new procedure was implemented: spent stages perform a propellant depletion maneuver, which allows them to both use up the remaining fuel and attain a decaying

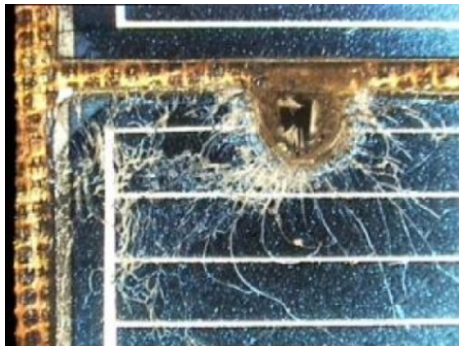

Figure 0.2 – Solar array of Hubble Space Telescope penetrated by a small piece of debris. The size of the hole is 2.5 mm. *Image credit: ESA*

orbit, on which they will burn in atmosphere in a (relatively) short time (ESA, a). It is recommended to move defunct satellites to graveyard orbits at their end of life, where they will not pose a danger to active satellites. Nonetheless, despite all the efforts to reduce the risk, collisions still occur. In 1996, a French military satellite Cerise was hit by a piece of debris from an Ariane rocket, and severely damaged (Johnson et al., 2008). The ISS performs debris avoidance maneuvers once per year on average (NASA, b). Due to high speeds at which objects travel through space, the consequences of an impact of even a very small piece of debris on an active satellite or space station can be very serious (e.g. Fig. 0.2).

Space debris can be found in any of the usually discriminated orbital regimes: Low Earth Orbits (LEO, below 2 000 km of altitude), Medium Earth Orbits (MEO, 2 000-35 786 km from Earth surface), or around the Geostationary Earth Orbits altitude (GEO, around 35 786 km). The current number of tracked space debris is about 22 300, but the estimations by statistical models put this number around 34 000, if only pieces big enough to be detected are considered ($>$ 10 cm); in addition, there are around 129 000 000 objects of smaller size (ESA, c). Most of them occupy the orbits between 800 and 1 000 km of altitude, and around 1 400 km (ESA, d), therefore remaining in the crowded LEO regime. The current predictions say that the number of space debris will steadily increase, which will in turn lead to more collisions between them, or them and active satellites. The pieces created in such events will then further raise the probability of subsequent collisions and the whole phenomenon may become self-sustained; this scenario is known as the Kessler syndrome (ESA, d). Its avoidance is necessary for the future of space missions and technologies. For this reason, several active debris removal strategies have been proposed, including laser methods and remotely controlled vehicles, but the costs of such undertakings are very high.

In order to be able to anticipate a collision in space, orbits of the objects have to be determined with highest possible precision. Most important forces acting on a body revolving around the Earth include:

- Earth gravity field – Earth gravitational field is far from being regular. The

asymmetries give rise to the geopotential perturbations, which are usually modelled in terms of spherical harmonics expansion. The biggest influence comes from the second degree harmonic J_2, related to planet oblateness, but for the model to be realistic, many high degree harmonics need to be included. The most advanced gravitational models nowadays contain spherical harmonics coefficients up to degree 2190 and order 2159 (EGM2008; NGA). In general, the higher the altitude of the object, the smaller the effect of the geopotential.

- atmospheric drag – as most of the debris orbit the Earth on relatively low altitudes, they pass through the higher levels of the atmosphere, which causes them to experience a drag-like force, depending on their speed relative to the medium. This leads to the altitude loss and eventual re-entry of an object in LEO. The density of the air depends on solar activity and geomagnetic storms, and can be described by several models in place (Petit and Lemaitre, 2016).

- other bodies attraction – the Sun and the Moon exert a substantial gravitational pull, the importance of which raises with altitude. Various timescales involved in their relative motion lead to an emergence of lunisolar resonances, which can stabilize an orbit or inspire chaotic behaviours. Out of the Solar System planets, Jupiter gravity should also be considered, although its magnitude is several orders smaller.

- solar radiation pressure – particularly relevant for pieces of debris with high area-to-mass ratio, the pressure of the Sun photons is small, but accumulates over the years and can generate large changes in the orbit.

Additionally, a multitude of smaller forces come in play when a higher precision of orbit determination is required. Some of them are the Poynting-Robertson effect (a braking effect the forward-coming solar radiation has on small particles), solar wind, the magnetic forces and, last but not least, the Yarkovsky effect, which is mainly considered in this thesis. The Yarkovsky effect consists of a small thrust that a body receives when it reradiates the solar radiation absorbed beforehand. This tiny force does not average to zero over one orbit if the object crosses Earth shadow, and instead accumulates over longer timescales. A more detailed description of the effect and its consequences are the subject of the first chapter of this thesis.

The dynamics of space debris is additionally complicated by orbital resonances. The Earth vicinity is transected by a net of lunisolar and tesseral resonances. Various orbital perturbations, including small forces, can drive space debris into these resonances, which can have ambivalent consequences. Some resonances have a stabilizing effect and could be therefore used as graveyard orbits, ensuring that the debris will stay in the region for a very long time; contrarily, other ones are chaotic, and the debris that arrive inside of them are reset on a distinct orbit, which may put them in more occupied regions of space, raising the threat to operating satellites. The analysis of the problem of resonances around the Earth is provided in the second chapter of this thesis.

The chaotic character of the resonances slips into numerical tools applied to their investigation. With the sensitivity of orbit calculation to the initial conditions, the nu-

merical uncertainties inherent to any orbit propagation scheme may lead to erroneous determination of the trajectory. It is therefore important to recognize which quantities can be evaluated accurately despite this issue. These considerations are developed in the third chapter of the thesis.

Within the space debris considerations of this thesis, the NIMASTEP software (Numerical Integration of Motion of Artificial Satellites orbiting a TElluric Planet) – the UNamur in-house numerical orbit propagation software, created by N. Delsate during his PhD thesis (Delsate, 2011; Delsate and Compère, 2012) – was used and upgraded. The software allows to track the motion of a satellite or a piece of space debris in the gravity field of a terrestial planet, an asteroid, or an arbitrary shape approximated by a triaxial ellipsoid, and to take into account a number of forces: the non-homogeneity of the gravitational potential, the gravity of a third body (Sun, Moon or any of the planets), the solar radiation pressure (including the effects of the shadow), the atmospheric drag (contribution of A. Petit as part of his PhD thesis (Petit, 2017)). The osculating equations of motion are integrated in Cartesian coordinates, and a number of integrators with either a constant step size (Runge-Kutta of order 4, Adams-Bashforth-Moulton of order 10) or a variable one (Runge-Kutta-Fehlberg of order 4(5), Runge-Kutta of order 8(5,3), Bulirsch-Stoer method) can be used. Two tools for the analysis of chaotic orbits are available: MEGNO indicator and frequency analysis (discussed more in Ch. 2). Software parallelization that allows for a simultaneous propagation of a large number of space debris was realized by A. Petit (Petit, 2017).

In the course of this thesis, we improved the capabilities of the software by implementing the Yarkovsky-Schach effect into it (vide Ch. 1).

The second UNamur internal software, SYMPLEC, developed by Ch. Hubaux in his PhD thesis (Hubaux et al., 2012; Hubaux, 2013), was also used (Ch. 3). The software uses symplectic algorithms in order to accurately propagate the dynamics over long timescales, considering central body harmonics of the potential, third body attraction, and solar radiation pressure.

0.2 Asteroids

Asteroids share many dynamical characteristics with space debris or satellites. They are located primarily in the Main Belt between Jupiter and Mars orbits, where another planet could have formed. They range in size from meters to hundreds of kilometers, the biggest one being Vesta at around 530 km in diameter. Their motion is governed by Sun central attraction and perturbed by Jupiter and, to lesser extent, other planets. The many resonances with Jupiter mean motion either accumulate the bodies around certain values of semi-major axis or push them onto more eccentric orbits, forming several groups of bodies that cross trajectories with Mars or Earth. Some of them may end up on collision course with the Earth. Two other mechanisms that deliver asteroids into resonant zones are collisions and the Yarkovsky effect. Working over sufficiently big timescales, the Yarkovsky effect is particularly influential on the dynamics of bodies from meter-sized meteoroids up to around 40 km in diameter.

The Yarkovsky effect depends on rotational parameters which in turn are not constant. The rotation of an asteroid on an orbit around the Sun undergoes variations due to several factors. Collisions between bodies and close approaches with the planets are important aspects, but the most prominent one is the YORP effect, a rotational counterpart of the Yarkovsky effect. The solar radiation, reflected off the object surface and absorbed and then re-emitted in infrared wavelengths, creates a tiny torque, which can substantially affect the rotation period and the obliquity of the spin axis. While tiny, the effect has already been observed for several asteroids (e.g. Taylor et al. (2007); Ďurech et al. (2012)). The YORP effect creates clusters of asteroids in similar spin-orbit resonant states within families (so-called Slivan states; Vokrouhlický et al. (2003)). It is the phenomenon that shapes the distribution of spin rates and pole orientations of small asteroids – it pushes the obliquities towards the limit values of 0°or 180°(although this is less obvious for prograde rotators as many spin-orbit resonances perturb their distribution) (Vokrouhlický et al., 2015). On Fig. 0.3, the spin rate distribution of 462 Main Belt and Mars-crossing asteroids, ranging in size from 3 to 15 kilometers, is presented. It is visibly uniform, except for a large amount of slow rotators; this is because the YORP effect drives bodies towards extreme values of the rotation period. At the other limit, when size-dependent fission values of the rotation period are reached, mass shedding or break-up slows down the angular momentum gain. This process may lead to creating binary asteroids (Walsh et al., 2008) or asteroids pairs. Observational evidence confirms this to be the most ubiquitous manner in which the binary systems emerge, as for most of binaries, the primary rotates very fast, and the total angular momentum of the system is close to fission value (Walsh and Jacobson, 2015). The similar case are the split pairs of asteroids – pairs of individual asteroids that do not have a common center orbiting the Sun, but show enough dynamical similarities to conclude that they once formed one object.

If the YORP effect produces a slowdown of the asteroid rotation, its period may become long enough for the body to enter tumbling rotation. Most asteroids rotate in the principal axis mode, i.e. their spin axis is aligned with the biggest inertia axis. This is a stable state of minimal rotational energy. Besides the YORP effect, close approaches to inner planets and collisions can disrupt this spin state and set bodies up on non-principal axis rotation, when the energy is excited, and the angular momentum vector drifts away from any of the body axes. The vast majority of asteroids is observed to rotate in a principal axis mode, which is in contradiction with models that indicate that the YORP effect tends to sustain tumbling rotation rather than mitigate it (e.g.Vokrouhlický et al. (2007); Breiter et al. (2011)). Although some part of the problem can be explained by observational inability to differentiate between mild tumbling (with the angle between the angular momentum vector and body shortest axis smaller than around 15°) and principal axis rotation, the amount of non-principal axis rotators that we detect should still be much higher. It is possibly due to some simplifications made in modelling the YORP effect; for example, many models assume zero thermal conductivity. Another probable explanation involves the damping mechanism resulting from inelastic energy dissipation. In short, the centrifugal acceleration that arises in wobbling rotation periodically exerts some tension on each body fragment. As the related deformations are not perfectly elastic (meaning that the body element does not

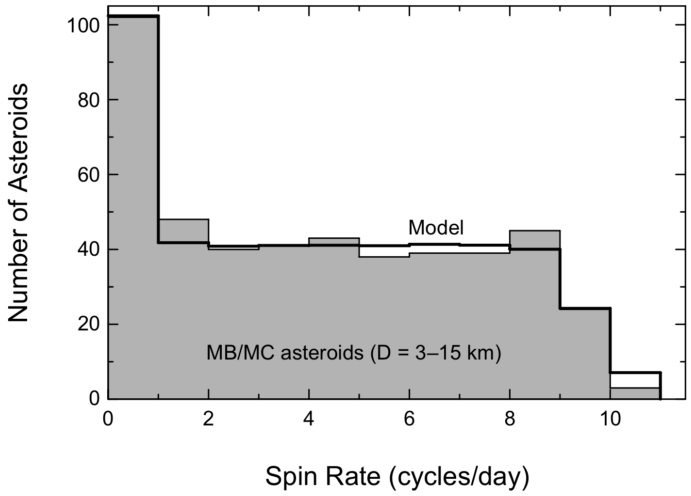

Figure 0.3 – Spin rate values for 462 asteroids in the Main Belt and on Mars-crossing orbits, in the size range between 3 to 15 kilometers. The excess on the left side are the bodies with the period of 1 day or longer, whereas the linear decrease on the right are bodies attaining rotational rates high enough to break down. The black line provides the values obtained with a simple YORP model. *from Vokrouhlický et al. (2015)*

retain its previous form and position once the deforming force ceases), some portions of energy are dissipated in form of heat in every cycle. This causes a decrease of the kinetic energy of rotation. The instantaneous rotation axis evolves towards the principal axis, where the tensions and deformations do not induce any energy loss.

The joint action of energy dissipation and the YORP effect is the subject of the fourth chapter of this thesis.

0.3 Subject of this thesis

While the knowledge about space debris motion advances quickly, there are still many unaswered questions. The dynamics inside resonant zones is complicated and not fully understood yet, with chaotic behaviours obscuring our comprehension, and additionally undercutting the applicability of some tools. At the same time, these zones have an important application and can provide a valid solution to the increasingly urgent problem of space debris and the threat they pose to active satellites.

Many aspects of the dynamics are common among the asteroids and satellites or space debris. The Yarkovsky effect is a major factor in case of small natural bodies; the fact that its influence on space debris orbit is rather small only stems from the relevance of different timescales in the two cases. It is still significant in applications requiring precisely determined orbits. The YORP effect also exists in the rotational motion of satellites or space debris, although the lack of data on their shapes and rotation states is a major hindrance. However, in the domain of asteroids, it plays a

substantial role, with more and more aspects to consider. Its interplay with energy dissipation needs to be clarified in order to explain some contradictions between current models and observational data.

Chapter 1

Yarkovsky effect on space debris

The Yarkovsky effect seems to be a relatively new problem in the dynamics of asteroids and satellites, but it was first proposed over a century ago. In 1901 Ivan O. Yarkovsky, a Russsian civil engineer of Polish origin, described in a self-published pamphlet how heating a prograde-rotating planet should produce a transverse acceleration in its motion (Yarkovsky, 1901). Back then, the ether hypothesis was still popular, so he was not able to calculate this effect accurately. Nevertheless, his idea was rediscovered and reintroduced after 50 years by E. Öpik (Öpik, 1951). The effect was studied in the following years, but some major developments were achieved in the 1980s and the 1990s, largely in the field of space geodesy. It was first detected by French accelerometer CACTUS on-board the slowly spinning CASTOR satellite (Boudon et al., 1979). A lot of progress was made in the framework of analysis of LAGEOS orbit residuals (e.g. Farinella et al. (1990); Métris et al. (1997)). The program involved two spherical satellites that served as laser ranging benchmarks for Earth geodynamical studies, and that were placed on very stable orbits in the MEO region. The precision with which the orbits were known is what allowed to study their tiny perturbations. A large part of LAGEOS orbit variations was associated to the Yarkovsky effect that occurs when the body crosses Earth shadow; this variant is usually referred to as the Yarkovsky-Schach effect. The shadow passage is crucial as, without it, the force averages to zero on one orbit. The Yarkovsky-Schach effect is the subject of this chapter.

Because the effect is weak, but systematic, it finds its applicability mainly in the domain of dynamics of natural small Solar System bodies, considering the long timescales that are customary in this context. It provided an explanation to several dynamical issues (e.g. dispersion of asteroid families (e.g. Bottke et al. (2001)), meteorite delivery (e.g. Farinella et al. (1998))). Most of the studies nowadays continue to focus on asteroids. However, the arising technological applications and challenges in the domain of satellite and space debris dynamics call for more rigorous orbit determination and recognition of small forces. Some proposed solutions to the space debris

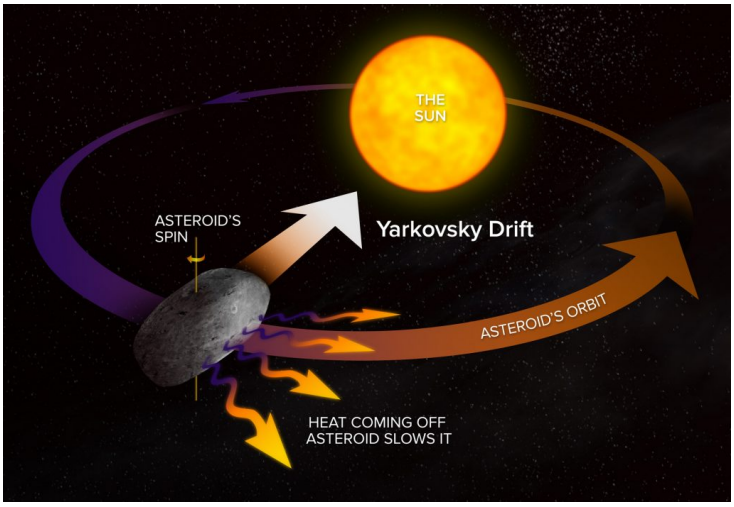

Figure 1.1 – Illustration of the Yarkovsky effect mechanism. *Source: NRAO*

problem also rely on very high precision of established orbits.

In this chapter, we discuss the modelling and consequences of the Yarkovsky-Schach effect on satellites and space debris.

1.1 The Yarkovsky effect

When solar radiation travelling through space hits the surface of a rotating body, two processes take place: it is either absorbed or reflected by this surface. The momentum of reflected photons is partially transferred to the body. The absorbed particles deposit the whole of their momentum in the body, but also heat it, causing it to emit thermal radiation. Neither the absorption nor the scattering of solar radiation produces any long-term dynamical effects in orbital motion that can be attributed to the recoil force resulting from thermal reemission. As the body thermal properties cause it to reemit absorbed heat after some time (usually referred to as ”thermal lag”), the direction of this emission differs from the direction to the Sun. The orbital effect depends on whether the body exhibits a prograde or retrograde rotation. In the first case, the emission occurs in the same direction in which the body moves along its orbit, and has thus a braking effect on body motion. This leads to a decrease of the semi-major axis and shrinking of the orbit (Fig. 1.1). A reversed result can be observed in case of retrograde rotation – the body receives an additional thrust from the reemission and its orbit expands as the semi-major axis grows. While small, this change in semi-major axis can alter the orbit significantly if enough time is allowed, which is what makes this secular effect important in studies exploring long-term dynamics or aiming at precise orbit determination.

To calculate the Yarkovsky effect, the net radiation energy and momentum ex-

change for all parts of the body need to to be considered. This is achieved by computing these components on a small surface element and then integrating over the whole surface of the body. The energy budget is necessary for the surface temperature solution and serves as a boundary condition. It can be written, in general, as

$$\epsilon\,\sigma\,T^4 + K\,\hat{n}\cdot\nabla T = (1-A)\max(0,\hat{n}\cdot\hat{r}_s)\,\Phi, \tag{1.1.1}$$

with the following physical parameters: ϵ is the emissivity, σ is the Stefan-Boltzmann constant, T is the temperature and ∇T its surface gradient, K is the surface thermal conductivity, A – the albedo, and Φ the solar flux. $\hat{n}$ is an outward-oriented normal vector to the surface element $\mathrm{d}\vec{S} = \hat{n}\,\mathrm{d}S$, whereas $\hat{r}_s$ is the unit vector directed towards the Sun. The right-hand side of the above equation is the total energy absorbed by the given surface element; the first expression on the left represents the thermally emitted energy, and the second – the energy carried away by conduction. In general, the emissivity and albedo coefficients are functions of the scalar product $(\hat{n}\cdot\hat{r}_s)$. However, most models adopt the Lambert's law to describe the emissivity and reflection processes, which removes this dependance and renders ϵ and A constant.

One of the main issues in computing the Yarkovsky effect is the determination of the surface temperature of the given body, which requires solving the heat diffusion problem. The heat conduction theory provides a description of the energy change in a volume element resulting from the heat flux through its boundary, in the form of Fourier heat equation in the body frame:

$$\rho\,C_p\frac{\partial T}{\partial t} = \nabla\cdot(K\,\nabla T), \tag{1.1.2}$$

with ρ being body density and C_p its specific heat capacity. These parameters, along with K, are generally dependent on temperature and position of the considered volume element in the body, but can be approximated as constant (calculated at body mean temperature) in case of small temperature variations.

The periodicity of the temperature changes with the fundamental frequency ν (due to the orbital motion with frequency n or rotation with frequency ω) allows for simplification of the problem by introducting the scale length $l_\nu = \sqrt{K/(\rho\,C_p\,\nu)}$, which expresses the characteristic penetration depth of the temperature variations. Secondly, the boundary condition (1.1.1) can be linearized by assuming that the temperature variations can be described as a small increment ΔT from the mean value T_0. Then $T = T_0 + \Delta T$, with $|\Delta T| \ll T_0$, can be substituted into (1.1.1), producing $T^4 \approx T_0^4 + 4\,T_0^3\Delta T$, where the terms of $\mathscr{O}(\Delta T^2)$ are neglected. With these simplifications, an analytical solution can be found provided the shape of considered body is simple. If the aim is to study the Yarkovsky effect on more realistic shapes, one needs to refer to numerical modelling in order to ensure the temperature regularity over the entire volume of the body.

The temperature variations depend mainly on thermal properties of the body in question - namely, the heat capacity and thermal conductivity of surface material. The asteroids, covered mainly with regolith, will heat up differently than space debris, made of metal and artificial materials; various types of space debris will also heat up differently.

Once the temperature can be evaluated, one can proceed to calculate the Yarkovsky force. As mentioned above, the impinging or reflected photons do not generate any long-term orbital effects, and therefore we only consider the contribution from the thermal reemission. With the assumption of Lambert's law for ϵ, the force is given, for an infinitesimal surface element dS, by

$$\mathrm{d}\vec{f}_{ther} = -\frac{2}{3}\frac{\epsilon\,\sigma T^4}{c}\hat{n}\,\mathrm{d}S, \tag{1.1.3}$$

(c is the speed of light) (Vokrouhlický and Bottke, 2010). The surface integral (over the whole body) of this infinitesimal force gives the net effect for the entire body. As far as the Yarkovsky effect is considered, simple shape models, including spherical ones, already produce a good approximation of the orbital evolution.

The most important consequence of the Yarkovsky force is the secular change in semi-major axis. The usual approach is to distinguish between two components of $\vec{f}_{ther}$: one aligned with spin axis direction (the fundamental frequency of which is the orbital motion), usually called the seasonal part, and one in the equatorial plane of the body (depending on the rotation rate), referred to as diurnal effect. They have a general form

$$\left(\frac{\mathrm{d}a}{\mathrm{d}t}\right)_{seasonal} = \frac{4}{9}\frac{(1-A)\pi R^2}{mc}\Phi F_n \sin^2\varepsilon, \tag{1.1.4}$$

$$\left(\frac{\mathrm{d}a}{\mathrm{d}t}\right)_{diurnal} = -\frac{8}{9}\frac{(1-A)\pi R^2}{mc}\Phi F_\omega \cos\varepsilon, \tag{1.1.5}$$

(Vokrouhlický and Bottke, 2010), where R is the radius of the body, m its mass and ε the obliquity of its spin axis (angle between the orbit normal and the spin axis direction). The F_n and F_ω functions depend on the thermal parameters and the size of the body; more precisely, on the ratio of the radius to the penetration depth, which is different for seasonal and diurnal parts as it depends on the frequency of temperature change. Since the rotation rate is generally higher than the orbital one, the seasonal wave penetrates deeper than the diurnal one. The F functions scale in such a way that the total effect is generally proportional to $1/R$. It is negligible for asteroids bigger than approx. 30 km of radius and disappears for small particles (below millimeter size), where the Poynting-Robertson effect (related to the isotropic re-emission of the absorbed solar radiation) dominates the dynamics.

The important feature of equations (1.1.4) and (1.1.5) is the spin axis obliquity dependence. The diurnal component of the effect is proportional to $\cos\varepsilon$, which means, considering that the F functions are always negative, that $\frac{\mathrm{d}a}{\mathrm{d}t}$ can be either negative (for $\varepsilon < 90^\circ$) or positive (in case of retrograde rotation), reaching the maximum when the spin axis is perpendicular to the orbit plane, $\varepsilon \approx 0^\circ$ and $\varepsilon \approx 180^\circ$, and virtually disappearing in case of $\varepsilon \approx 90^\circ$. The seasonal effect always produces an inward secular migration of the orbit due to proportionality to $\sin^2\varepsilon$ ($\frac{\mathrm{d}a}{\mathrm{d}t}$ negative), with maximum in case of spin axis laying in the orbital plane and minimum for $\varepsilon = 0^\circ$ and $\varepsilon = 180^\circ$.

For the asteroids, the diurnal component is usually more significant than the seasonal one. In artificial satellite studies, it is common to use the so-called fast-rotation

approximation, which ignores diurnal components completely, even though the torques present in the near-Earth environment may slow down the rotation to the values that would violate this assumption.

In satellite motion, the secular perturbations in semi-major axis only arise if the satellite or space debris crosses the shadow of the Earth (or the central body in general). This causes a disruption in the solar flux arriving on the object surface, where it has time to cool down and heat up again once the body exits the shadow. Without this variation in the thermal force, it would average out during one orbit. This variant of the Yarkovsky effect was proposed as an explanation of eclipse-related spikes in semi-major axis residuals of LAGEOS satellite, and was dubbed the Yarkovsky-Schach effect.

The Yarkovsky effect is a minuscule force, but its cummulative character allows it to have a substantial impact on the orbit. The Yarkovsky-Schach variant, that is the main point of interest in this chapter, is of magnitude of several picometers per second squared. Fig. 1.2 demonstrates how it compares to other forces acting on satellites and space debris. Nevertheless, along with the technical advancement and a growing need for more precise determination of the artificial satellites orbits, such tiny forces become more and more relevant. They can be important for some of the space debris removal strategies or in geodynamical studies. Also, slow orbit decay or growth can, given enough time, put inactive satellites and debris in resonant zones, where they could stay for centuries (on the so-called ”graveyard orbits”) or, on the contrary, end up on chaotic orbits (as demonstrated by Lhotka et al. (2016) for the Poynting-Robertson effect).

1.2 Method

The model that was used in our numerical simulations is that of Farinella and Vokrouhlický (1996). This choice was dictated by the fact that, as opposed to others (to the author's best knowledge), it does not rely on the fast rotation assumption. It was developed mainly to predict the orbital elements variations of the LAGEOS orbit once the fast rotation approximation becomes invalid, as the rotation slows down rapidly due to the magnetic dissipation effects. The authors show that in this case, the equatorial components that are no longer negligible have a significant impact on the semi-major axis residuals and therefore should not be ignored. They also produce an effect on the orbital inclination, though the variations in eccentricity are already explained by the spin-axis component of the force.

Even though there is not much data on space debris attitude, one can assume that most of them experience tumbling rotation due to either their origin in crashes between debris, or the multitude of torques present in the space environment (Earth, Sun, Moon gravitation, interactions with the atmosphere, outgassing or leakages, impact of micrometeoroids, eddy currents, or the YORP effect). However, as the model we use is based on the assumption of sphericity of the considered body, we do not consider this problem here. The satellite is assumed to possess homogeneous physical properties, and to reside on a low-eccentricity orbit. There are three essential

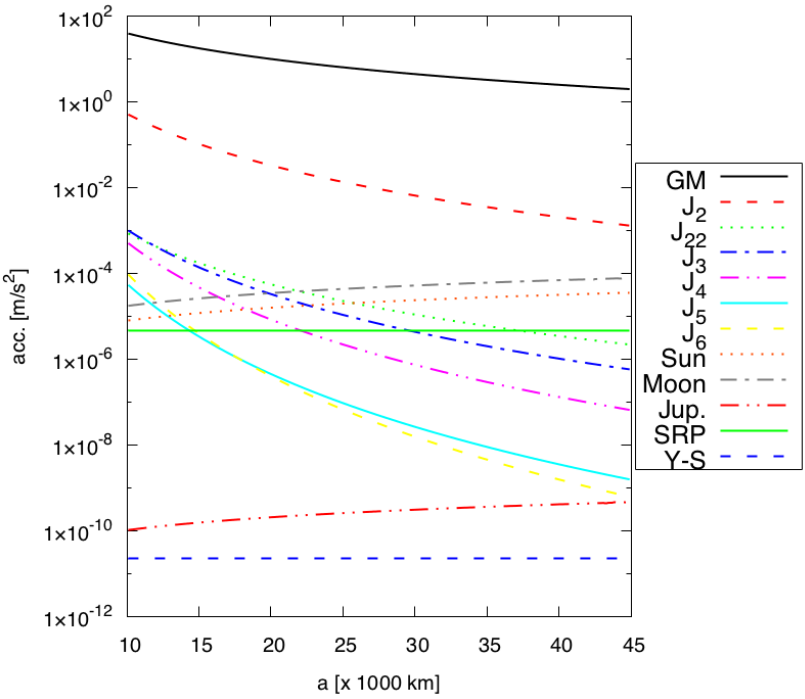

Figure 1.2 – Order of magnitude of several major Earth satellite perturbations as a function of orbit semi-major axis a (in order as listed in plot legend: GM, $J_2 - J_6$ geopotential harmonics, Sun, Moon and Jupiter gravitational attraction, solar radiation pressure (with A/m set to 0.1 m^2/kg) and the Yarkovsky-Schach effect). The plot was created using simplified formulae from Montenbruck and Gill (2000).

timescales in the problem: the period of rotation P_{rot}, the orbital period P_{orb} and the thermal relaxation time τ_r (the time between the absorption and re-emission of the sunlight). If the spin period is shorter than the thermal relaxation time, there are no diurnal components of Yarkovsky acceleration and the force is always directed along the spin axis. However, as shown by Farinella and Vokrouhlický (1996), when the rotation is slow enough, these components may be significant.

The problem of calculating the temperature variations distribution on the satellite surface is approached as follows. The linearization of temperature variations is used in the heat diffusion equation and the energy budget equation. Therefore, (1.1.2) takes the form

$$K\nabla^2\Delta T = \rho\, C_p \frac{\partial \Delta T}{\partial t}, \tag{1.2.1}$$

and the energy conservation

$$4\,\epsilon\,\sigma T_0^3 \Delta T + K\hat{n}\cdot\nabla\Delta T = (1-A)\Delta\Phi, \tag{1.2.2}$$

where $\Delta\Phi$ is used in place of $\max(0,\hat{n}\cdot\hat{r}_s)\Phi$. The authors further proceed to use the method proposed by Rubincam (1987) to solve the above equations by the use of Fourier transform and get ΔT as an integral of the flux change

$$\Delta T(t,\hat{n}) = \frac{3(1-A)}{\rho C_p R}\int_{t'<t}\Delta\Phi(t')\mathrm{e}^{-\nu_R(t-t')}\mathrm{d}t', \tag{1.2.3}$$

evaluated over time span between a retarded moment of time t' and t, related to the rotational motion of the object. The idea is that the surface element $\mathrm{d}S'$ at moment t' eventually becomes identical with $\mathrm{d}S$ at moment t, for which the ΔT is calculated. The exponential factor characterizes the thermal relaxation process, where ν_r is the inverse of the thermal relaxation time:

$$\nu_r = \frac{1}{\tau_r} = \frac{12\,\epsilon\,\sigma\,T_0^3}{\rho C_p R}. \tag{1.2.4}$$

Knowing the temperature field on the surface, the acceleration $\vec{a}$ is derived as (with the assumption of Lambert's emission law)

$$\vec{a}(t) = -\frac{8}{3}\frac{\epsilon\,\sigma}{mc}T_0^3\int_{t'<t}\Delta T(t,\hat{n})\,\hat{n}\,\mathrm{d}S, \tag{1.2.5}$$

integrated over the whole surface.

The local reference frame is defined with $\vec{e}_z$ along the spin axis of the object, $\vec{e}_x$ in such a way that it is perpendicular to $\vec{e}_z$ and the xz plane contains the direction to the Sun $\vec{r}_s$, and $\vec{e}_y$ complements the orthogonal right-handed system. Then, θ_r describes the angle between the spin axis and $\vec{r}_s$ in the body-centered frame. Using satellite longitude along the orbit λ instead of the time, $\lambda = nt+\lambda_0$, the force components in the defined reference frame are

$$a_x = \gamma\frac{\sin\theta_r}{1+r^2\sigma_r^2}(\hat{C}(r,\bar{e})\Psi_C(\lambda,r) - \hat{S}(r,\bar{e})\Psi_S(\lambda,r)), \tag{1.2.6}$$

$$a_y = \gamma\frac{\sin\theta_r}{1+r^2\sigma_r^2}(\hat{C}(r,\bar{e})\Psi_S(\lambda,r) + \hat{S}(r,\bar{e})\Psi_C(\lambda,r))), \tag{1.2.7}$$

$$a_z = \gamma\cos\theta_r\Psi_z(\lambda). \tag{1.2.8}$$

r is the ratio between the orbital and rotational periods, $r = P_{orb}/P_{rot}$, and σ_r – the ratio between the thermal relaxation time and the orbital period, $\sigma_r = \tau_r/P_{orb}$. All the physical constants are encapsulated in the parameter γ:

$$\gamma = -\frac{16\pi}{3}\frac{\sigma\Phi(1-A)\;\epsilon\;R\,\tau_r\,T_0^3}{mc\,\rho\,C_p}. \tag{1.2.9}$$

The auxiliary constants are

$$\hat{C} = \frac{1-\bar{e}\cos(2\pi r)}{1-2\bar{e}\cos(2\pi r)+\bar{e}^2}, \tag{1.2.10}$$

$$\hat{S} = \frac{\bar{e}\sin(2\pi r)}{1 - 2\bar{e}\cos(2\pi r) + \bar{e}^2}, \tag{1.2.11}$$

with $\bar{e} = \exp(-\frac{2\pi}{\sigma_r})$. The Yarkovsky acceleration depends explicitly on the orbital longitude through the so-called "shadow factors" – functions related to entry into and exit from Earth shadow:

$$\begin{aligned}\Psi_C(\lambda) = &(1 - \bar{e}(\cos(2\pi r) - r\sigma_r \sin(2\pi r)))\psi_{shad}(\lambda) \\ &+ \mathrm{e}^{\Delta_1/\sigma_r}(\xi_1^- \cos(r\Delta_1) + \xi_1^+ \sin(r\Delta_1)) \\ &- \mathrm{e}^{\Delta_2/\sigma_r}(\xi_2^- \cos(r\Delta_2) + \xi_2^+ \sin(r\Delta_2)),\end{aligned} \tag{1.2.12}$$

$$\begin{aligned}\Psi_S(\lambda) = &(r\sigma_r - \bar{e}(\sin(2\pi r) + r\sigma_r \cos(2\pi r)))\psi_{shad}(\lambda) \\ &- \mathrm{e}^{\Delta_1/\sigma_r}(\xi_1^- \cos(r\Delta_1) - \xi_1^+ \sin(r\Delta_1)) \\ &+ \mathrm{e}^{\Delta_2/\sigma_r}(\xi_2^- \cos(r\Delta_2) - \xi_2^+ \sin(r\Delta_2)),\end{aligned} \tag{1.2.13}$$

where

$$\Delta_1 = \begin{cases} \lambda_1 - \lambda, & \text{for } \lambda_1 < \lambda, \\ \lambda_1 - \lambda - 2\pi, & \text{for } \lambda_1 > \lambda, \end{cases} \qquad \Delta_2 = \begin{cases} \lambda_2 - \lambda, & \text{for } \lambda_2 < \lambda, \\ \lambda_2 - \lambda - 2\pi, & \text{for } \lambda_2 > \lambda, \end{cases} \tag{1.2.14}$$

with λ_1 and λ_2 being the orbital longitudes corresponding to the entry into Earth shadow and the exit from it, respectively. ψ_{shad} is the usual shadow function and is equal to 0 when the satellite is in the shadow and to 1 outside of it. Lastly, we also have

$$\xi_i^- = \begin{cases} \cos(2\pi r) - r\sigma_r \sin(2\pi r), & \text{for } \lambda_i > \lambda, \\ 1, & \text{for } \lambda_i < \lambda, \end{cases} \tag{1.2.15}$$

$$\xi_i^+ = \begin{cases} \sin(2\pi r) + r\sigma_r \cos(2\pi r), & \text{for } \lambda_i > \lambda, \\ r\sigma_r, & \text{for } \lambda_i < \lambda. \end{cases} \tag{1.2.16}$$

a_z coincides, as expected, with the Yarkovsky effect in the fast rotation approximation, when the equatorial components disappear.

We programmed the above equations for the acceleration in the NIMASTEP software, described in the Introduction, and tested the code against the results presented in Farinella and Vokrouhlický (1996). The implementation also required the computation of λ_1 and λ_2. Following the approach of Afonso et al. (1989), it amounts to solving the eclipse equation

$$\tan^2\lambda \left(R_2^2 + \frac{1}{a^2} - 1\right) + \tan\lambda\,(2R_1R_2) + \left(R_1^2 + \frac{1}{a^2} - 1\right) = 0, \tag{1.2.17}$$

where the two auxiliary quantities are $R_1 = \vec{r}_1 \cdot \vec{s}$, $R_2 = \vec{r}_2 \cdot \vec{s}$ – scalar products of unit vectors $\vec{r}_1$ from the Earth to satellite orbit ascending node and $\vec{r}_2$ perpendicular to it in the orbital plane, and $\vec{s}$ pointing from the Earth to the Sun. The discriminant of the

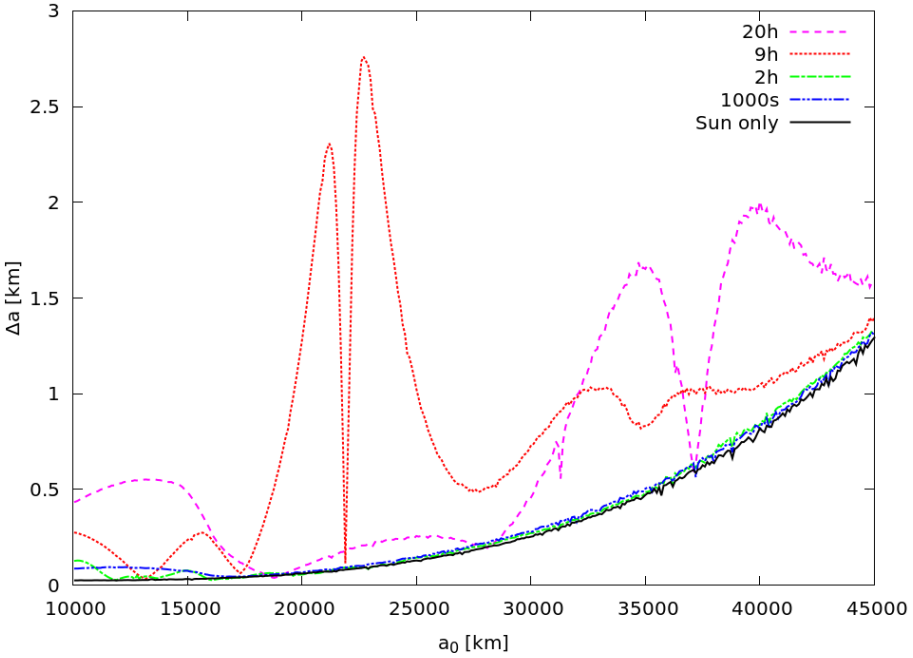

Figure 1.3 – Variation in semi-major axis due to the Yarkovsky effect, depending on its initial value and the rotation period. The orbits were propagated over 400 y timespan.

above equation bigger than 0 gives four solutions for λ, but two of them should be discarded as they correspond to the pseudo-shadow (the shadow around $\vec{s}$ rather than $-\vec{s}$).

Most of the sparse studies dealing with the Yarkovsky effect on artificial satellites aim to explain the orbital residuals found in the observational data of LAGEOS and similar satellites. The point of this study was therefore to invert this trend and try to carry out numerical simulations for various orbits and rotational states.

1.3 Results

In the following, we adopted the value of $\gamma/P_{rot} = -8.85 \times 10^{-10}$. It corresponds to a spherical satellite of radius $R = 0.3$ m with $\rho = 2.7$ g/cm^3. The obliquity of the spin axis is set to 45°unless stated otherwise; similarly, the initial values of the orbital elements are: $e = 0.01$, $i = 0.01°$, $\Omega = \omega = M = 0.0$. All integrations were performed with the Runga-Kutta-Fehlberg integrator of order 5 with variable stepsize.

In Fig. 1.3, the variations of the semi-major axis Δa are shown, as well as the way they depend on the initial semi-major axis a_0. The integration time was 400 y, and various rotation periods were used, ranging from 1000 s to 20 h (the first one basically corresponding to the fast rotation approximation). As the orbital inclination

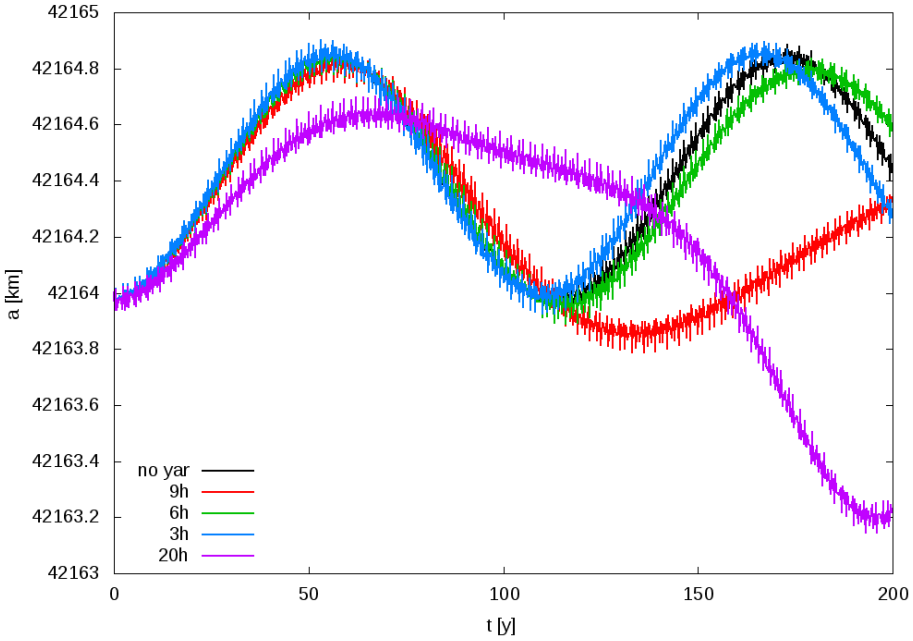

Figure 1.4 – Temporal evolution of space debris on a geostationary orbit, depending on rotation rate.

is close to 0, various semi-major axes a_0 are indicative of the portion of orbit that the body spends in Earth shadow, with bigger a_0 values meaning shorter relative time of incoming solar radiation cut. The only perturbations that are considered are the gravitational attraction of the Sun and the Yarkovsky-Schach effect, as the two forces cannot be separated within our implementation. The Sun-only-related curve is also plotted for reference (in black). This clarifies that the increase of semi-major axis change with a_0 is due to Sun gravity. Slower rotation produces bigger Δa, due to the fact that reducing the rotation rate leads to the appearance of diurnal components and overall stronger perturbation. The effect is small for lower orbits, with biggest values for longest rotation periods. The maximum of Δa = 2.76 km is reached at $a_0 = 22\,700$ km for the rotation period of 9 h; this is attributed to a longer shadow passage than at a_0 around 40 000 km (the peak of 20 h period curve).

The time evolution of a sample orbit close to the geostationary altitude is shown in Fig. 1.4, on a timescale of 200 y. The black curve is again due to Sun gravity only. The differences between the trajectories result solely from different rotation periods taken for the object; they were chosen to span a wide range of values. The curves representing shorter rotation periods (6 h – green and 3 h – blue) take longer to diverge from the Sun-related one, starting after around 120 y; differences for objects of approx. 9 h rotation period can be noted already after approx. 70 y, whereas those with slowest rotation (20 h) start to deviate almost immediately after the beginning

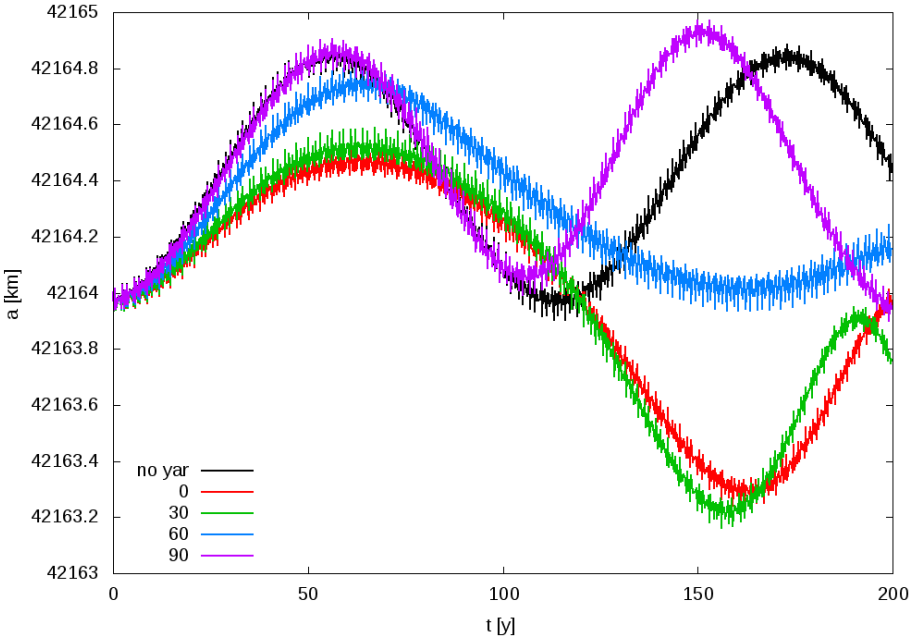

Figure 1.5 – Analogous as in Fig 1.3 but with colors decoding the obliquity ε of the object spin axis. The rotation period is 20 h.

of the integration. At this distance from the Earth, the rotation period of 20 h is the closest to the orbital one, it is therefore expected to be associated with the biggest Δa, in light of Fig. 1.3. This effect is again related to the diurnal components.

The differences in the spin axis obliquity also have an impact on the thermal force (Fig. 1.5). The most considerable departure from reference trajectory is observed for an obliquity equal to 30°. As the inclination is close to zero and the orbit is in the equator plane, the values of ε close to that of the Earth obliquity would maximize the value of $\sin\theta_r$ in (1.2.6)-(1.2.7), leading to elevated values of diurnal components a_x, a_y. The opposite can be said about $\varepsilon = 60°$ and $\varepsilon = 90°$: the contribution of the equatorial part decreases and the overall perturbation is weaker.

The inclination of the satellite or space debris orbit play a significant role. Fig. 1.6 shows that the biggest impact on the semi-major axis occurs at $i \approx 15° - 35°$, with the maximum of $\Delta a \approx 5.8$ km at $i \approx 23°$. This result is related to the Sun – Earth – satellite orbit geometry – an object on the orbit with this inclination spends a significant amount of time in the shadow, which causes highest temperature amplitudes on its surface. Nevertheless, most space debris are accumulated in orbit regions of lower or higher inclinations, where the Yarkovsky-Schach effect has a minimal impact. For higher inclinations, the object does not cross the shadow at all, so the effect is irrelevant in long-term considerations.

Some variations arise in other orbital elements. Farinella and Vokrouhlický (1996)

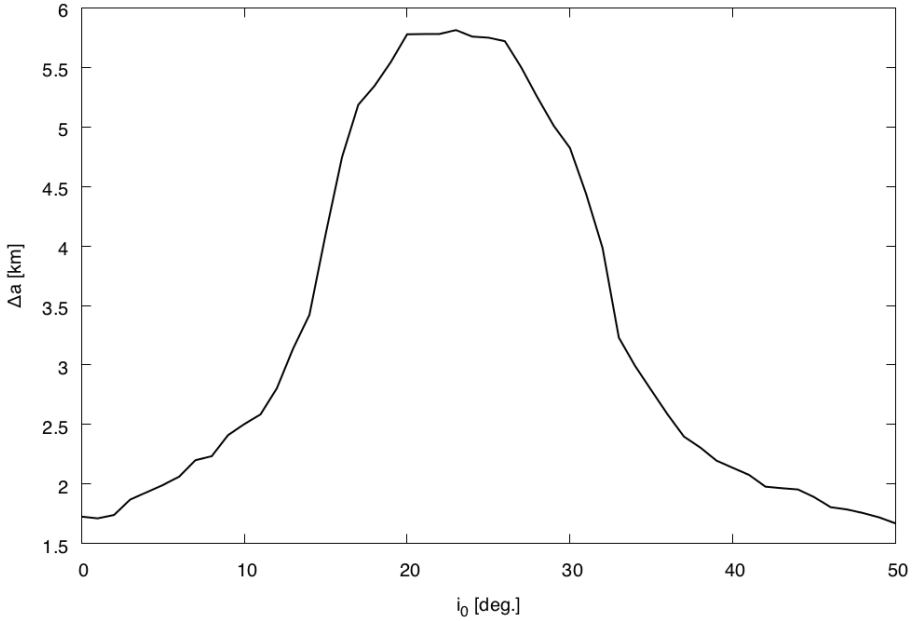

Figure 1.6 – Variations in the semi-major axis vs. orbit inclination. The initial value of semi-major axis is 42 164 km, and the rotation period is 20 h. The integration time is 200 y.

pointed out that the equatorial components do not modify the results obtained for eccentricity with fast rotation approximation; nevertheless, the overall effect is still observed (Fig. 1.7). Similarly to Sun-perturbed-only case, the change in eccentricity depends weakly on the initial semi-major axis after some distance is reached. The situation is similar when the thermal force is introduced, but this semi-major axis value is smaller. There is no difference between various rotation periods as the only significant component of the force is the one aligned with spin axis, independent of rotation. There is no effect on eccentricity for larger orbits. The generated Δe is of the order of 10^{-3} after 200 y. A significant effect can be observed in inclination if enough time is allowed (200 y again, Fig. 1.8), although it seems to be due to the seasonal part only. The Yarkovsky-Schach force produces an additional variation of several degrees. Some small variations can also be detected in the argument of perigee (Fig. 1.9).

1.4 Conclusions

The results presented in this chapter confirmed the tiny magnitude of the Yarkovsky-Schach effect on space debris or satellite orbits. Extensively large integration timescales need to be used in order to clearly distinguish the impact of the force in the results. With that in mind, some variations of several kilometers in semi-major axis are de-

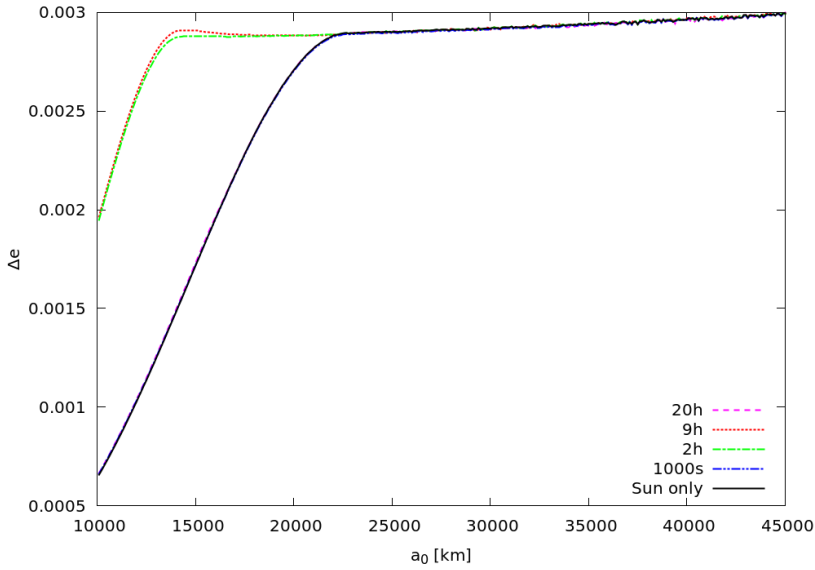

Figure 1.7 – Variations in eccentricity as a function of the initial value of the semi-major axis, plotted for various rotation periods of the debris. The curve representing the Sun-induced motion coincides with that of $P_{rot} = 20$ h.

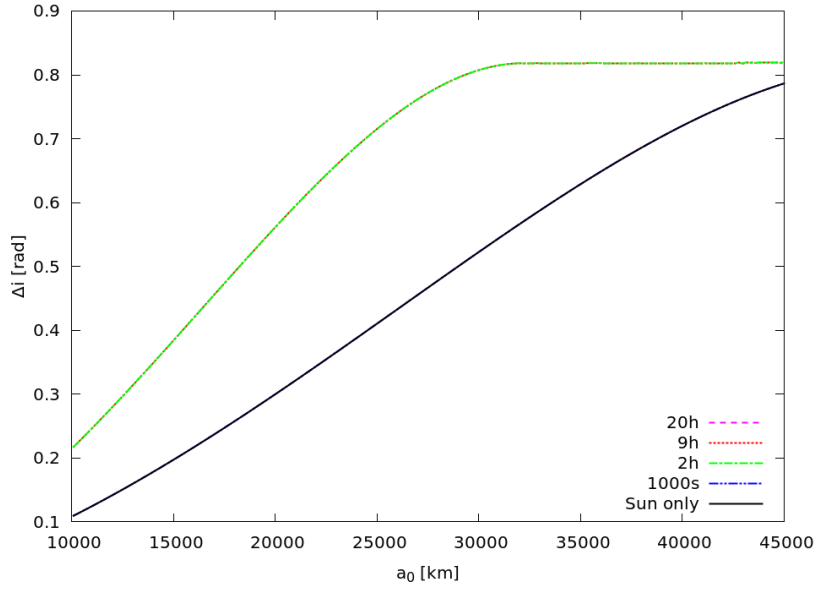

Figure 1.8 – Same as above, but for variations in inclination. All the thermal force-perturbed trajectories are gathered together.

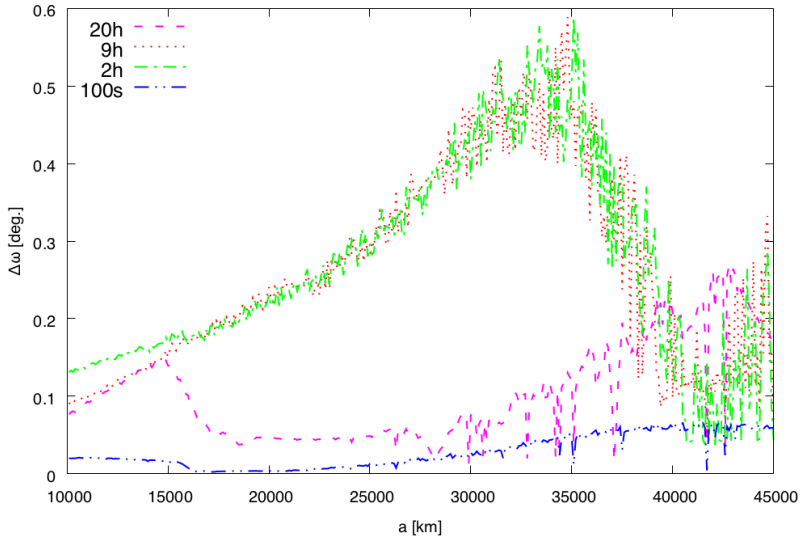

Figure 1.9 – Variations in the argument of perigee, calculated as residuals in respect to Sun-only trajectory. The integration time is 200 y, the rotation period is 20 h, and the initial semi-major axis is 42 164 km.

tectable on such long timescales. Similarly, there is also a relatively significant change in inclination. Nonetheless, this effect belongs to the class of small nongravitational forces that could be important for high-precision orbit determination applications or studies interested in very long-term dynamics, where they produce discrepancies with models based on gravitational perturbations only. Such missions have already been carried out (the already discussed LAGEOS satellites are a good example, another one being the GRACE program), and will surely continue to appear in the future. In the domain of space debris, there are proposed strategies of removal that could also benefit from precise orbit determination, such as technologies focusing on laser illumination of debris. Current estimations of the Yarkovsky-Schach effect are still impaired by our lack of knowledge on actual physical parameters and exact shape of the debris in space; should such data emerge in the future, the precision of the force evaluation could be further corroborated.

Chapter 2

Resonances in MEO region

The resonances are one of the most important and widespread features in the dynamics of small bodies in the Solar System. They occur wherever there is a commensurability between the orbital or rotational motion of two bodies. They play a huge part in shaping the Main Belt of asteroids, producing gaps in semi-major axis distribution around the values corresponding to mean motion resonances with Jupiter's orbit, as well as grouping objects in stable resonances in other areas. Similarly, the mean motion resonances with Neptune form many populations among trans-Neptunian objects. The moons within Saturn's rings sweep away the ice and dust at some values of semi-major axis. Likewise, the objects on orbits around the Earth may fall into a resonance with planet's tesseral harmonics of the gravitational potential. Additionally, the disturbing gravitational pull of the Sun and the Moon produces a network of lunisolar resonances, depending on the inclination and eccentricity of the object.

All these phenomenons form a mesh of resonances in the vicinity of the Earth that may hold a great importance for the problem of space debris. The orbits located in stable regions could serve as graveyard orbits, where retired satellites would stay for very long periods of time without posing any danger to those that are active. On the other hand, space debris entering the chaotic regions (e.g. due to the consequent action of small perturbations) could quickly end up on eccentric orbits that could traverse zones populated with active spacecrafts.

In this chapter, we discuss the two types of resonances in space debris environment: tesseral and lunisolar resonances, focusing on MEO region. We create an atlas of stability maps for these resonances, compare them with the literature, and consider some potential secondary resonances, based on features visible on the maps.

2.1 Resonances: essentials

Assuming we have a system that can be described by a main force and a small perturbation, the resonance is said to occur when in the development of such a perturbation,

there are terms containing an angle which vary very slowly (so that the time derivative is close to zero). This occurs when two angles in the system have commensurable frequencies ν_1, ν_2:

$$\frac{k_1}{k_2} = \frac{\nu_2}{\nu_1}, \tag{2.1.1}$$

where k_1, k_2 are two integers.

The Hamiltonian of a problem involving a resonance can be expressed in action-angle variables and reduced to pedulum-like form (the First Fundamental Model of resonance (Breiter, 2003)) through averaging and expansion techniques. The phase space is then divided into circulation and libration zones, with chaotic motions developing along the separatrices between the two regimes. Along with the growth of the perturbation, the chaotic motion propagates and disrupts the stable zones within the libration region, allowing the chaotic orbits the possibility to explore extensive parts of the phase space, and effectively reducing the predictability of motion in the region.

2.1.1 Tesseral resonances

In this thesis, two classes of resonances will be considered: tesseral and lunisolar resonances. The tesseral resonance arises when there is a commensurability between the orbital period of an object revolving around the Earth and the rotational period of the planet. The most well-known example of this kind of resonance is the 1:1 resonance, corresponding to the geostationary altitude. The MEO region is, however, intersected with other tesseral resonances of higher orders.

The potential of the Earth has the form

$$U_{geo} = U_0 + U_P, \tag{2.1.2}$$

where U_0 is the potential of a sphere and U_P could be considered its perturbation, resulting from the non-sphericity of the Earth. It is usually described with the use of spherical harmonics

$$U_P = -\frac{\mu}{r} \sum_{n\leq} \sum_{m=0}^{n} \left(\frac{r_E}{r}\right)^n P_n^m(\sin\phi)\left(C_{n,m}\cos m\lambda + S_{n,m}\sin m\lambda\right). \tag{2.1.3}$$

The indices n, m are the order and degree of the development, respectively. The rest of the symbols are: r – geocentric distance of the object, $\mu = GM$ – gravitational parameter, r_E – Earth's radius, P_n^m – Legendre function of degree n and order m. (ϕ, λ) are the longitude and latitude of the object in the reference frame rotating with the Earth, and $C_{n,m}$ and $S_{n,m}$ are the coefficients of the geopotential. Coefficients with $m = 0$ correspond to the effects independent of the longitude λ; in this case, $S_{n,0} = 0$ and the terms with $J_n = -C_{n,0}$ are referred to as zonal harmonics. J_2, related to the Earth's flattening, is the most dominant effect, responsible for secular drift in ω and Ω:

$$\dot{\omega} = \frac{3}{4}\frac{J_2 r_E^2 n}{a(1-e^2)^2}(5\cos^2 i - 1), \tag{2.1.4}$$

$$\dot{\Omega} = -\frac{3}{2}\frac{J_2 r_E^2 n}{a(1-e^2)^2}\cos i \tag{2.1.5}$$

(Murray and Dermott, 2000), from which it is clear that polar orbits (with $i = 90°$) do not experience any effect in the longitude of the ascending node, and the perturbations in the argument of perigee disappear for the so-called critical inclinations equal to $63°26'$ and $116°34'$.

The Kaula development provides the expression of the geopotential in terms of the orbital elements (Kaula, 1966):

$$U_P = -\frac{\mu}{a}\sum_{l\geq 2}\sum_{m=0}^{n}\sum_{p=0}^{n}\sum_{q=-\infty}^{\infty}\left(\frac{r_E}{a}\right)^n J_{n,m}F_{nmp}(i)G_{npq}(e)S_{nmpq}(M,\omega,\Omega,\theta_\oplus), \tag{2.1.6}$$

where the indices l,m,p,q identify the terms in the inclination and eccentricity functions $F_{nmp}(i)$ and $G_{npq}(e)$. Their full forms can be found in Kaula (1966), let us only note that $G_{npq}(e) \approx \mathscr{O}(e^{|q|})$. Furthermore, we have

$$J_{nm} = \sqrt{C_{nm}^2 + S_{nm}^2}, \tag{2.1.7}$$

$$S_{nmpq} = C_{nm}\cos\Psi_{nmpq} + S_{nm}\sin\Psi_{nmpq}, \tag{2.1.8}$$

$$\Psi_{nmpq} = (n-2p+q)M + (n-2p)\omega + m(\Omega-\theta_\oplus) + \varepsilon_{nm}\frac{\pi}{2} - m\lambda_{nm}. \tag{2.1.9}$$

$\theta_\oplus$ is the sidereal time and depends explicitly on time.

The two fast angles of the problem are M and $\theta_\oplus$. The resonance occurs when

$$(n-2p+q)\dot{M} - m\,\dot{\theta}_\oplus \simeq 0. \tag{2.1.10}$$

The indices (n,m,p,q) that satisfy this condition are called the resonant indices, and the resonance is identified by the natural indices n_1, n_2 satisfying

$$\frac{n_1}{n_2} = \frac{m}{n-2p+q}. \tag{2.1.11}$$

Eq. (2.1.10) gives a condition for the resonant semi-major axis

$$\frac{\mu^{\frac{1}{2}}a^{-\frac{3}{2}}}{\dot{\theta}_\oplus} \simeq \frac{m}{n-2p+q} \quad \Rightarrow \quad a_{res} \simeq \left(\frac{m}{n-2p+q}\,\dot{\theta}_\oplus\mu^{-\frac{1}{2}}\right)^{-\frac{2}{3}}. \tag{2.1.12}$$

The order of the resonance is defined as

$$|k| \equiv n-2p+q+m. \tag{2.1.13}$$

The smaller the order, the more important the resonance. Tab. 2.1 gathers the most eminent resonances in the Earth's vicinity.

In order to use the Hamiltonian formalism, one needs to know the form of the potential in canonical variables. The action-angle Delaunay variables have simple

expressions in terms of Keplerian elements:

$$\begin{aligned} L &= \sqrt{\mu\, a}, & l &= M, \\ G &= L\sqrt{1-e^2}, & g &= \omega, \\ H &= G\cos i, & h &= \Omega. \end{aligned} \tag{2.1.14}$$

In these variables, the Hamiltonian of the problem becomes

$$\mathscr{H} = -\frac{\mu^2}{2L^2} + \mathscr{H}_{sec}(L,G,H,l,g,h) + \mathscr{H}_{res}(L,G,H,l,g,h) + \mathscr{H}_{nonres}(L,G,H,l,g,h). \tag{2.1.15}$$

The secular part $\mathscr{H}_{sec}$ corresponds to $n-2p+q=0$ and $m=0$ and has the form, up to the second order of eccentricity and third order of spherical harmonic expansion:

$$\begin{aligned} \mathscr{H}_{sec} =& \frac{\mu\, r_E^2 J_2}{a^3}\left(\frac{3}{4}\sin^2 i - \frac{1}{2}\right)(1-e^2)^{-\frac{3}{2}} \\ &+ \frac{2\mu\, r_E^3 J_3}{a^4}\left(\frac{15}{16}\sin^3 i - \frac{3}{4}\sin i\right) e(1-e^2)^{-\frac{5}{2}}\sin\omega \end{aligned} \tag{2.1.16}$$

(Celletti and Galeş, 2014). The tesseral resonance discussed the most in this thesis is the 2:1 resonance. The resonant part of its Hamiltonian, truncated to e^4 and $\sin^4 i$, is

$$\begin{aligned} \mathscr{H}_{res} =& \frac{\mu\, r_E^2 J_{22}}{a^3}\left(\frac{3}{4}(1+\cos i)^2(-\frac{e}{2}+\frac{e^3}{16})\cos(M-2\theta_\oplus+2\omega+2\Omega-2\lambda_{22})\right. \\ &+\frac{3}{2}\sin^2 i\left(\frac{3}{2}e+\frac{27}{16}e^3\right)\cos(M-2\theta_\oplus+2\Omega-2\lambda_{22}) \\ &\left.+\frac{3}{4}(1-\cos i)^2\frac{67}{48}e^3\cos(M-2\theta_\oplus-2\omega+2\Omega-2\lambda_{22})\right) \\ &+\frac{\mu\, r_E^3 J_{32}}{a^4}\left(\frac{15}{8}\sin i(1+\cos i)^2\left(\frac{e^2}{8}+\frac{e^4}{48}\right)\sin(M-2\theta_\oplus+3\omega+2\Omega-2\lambda_{32})\right. \\ &+\frac{15}{8}\sin i(1-2\cos i-3\cos^2 i)\left(1+2e^2+\frac{239}{64}e^4\right)\sin(M-2\theta_\oplus+\omega+2\Omega-2\lambda_{32}) \\ &\left.-\frac{15}{8}\sin i(1+2\cos i-3\cos^2 i)\left(\frac{11}{8}e^2+\frac{49}{16}e^4\right)\sin(M-2\theta_\oplus-\omega_2\Omega-2\lambda_{32})\right) \end{aligned}$$

Table 2.1 – Most prominent resonances close to the Earth.

order	(n_1,n_2)	a_{res} (km)
2	(1,1)	42 164
3	(2,1)	26 561
4	(3,1)	20 270
5	(4,1)	16 732
5	(3,2)	31 177

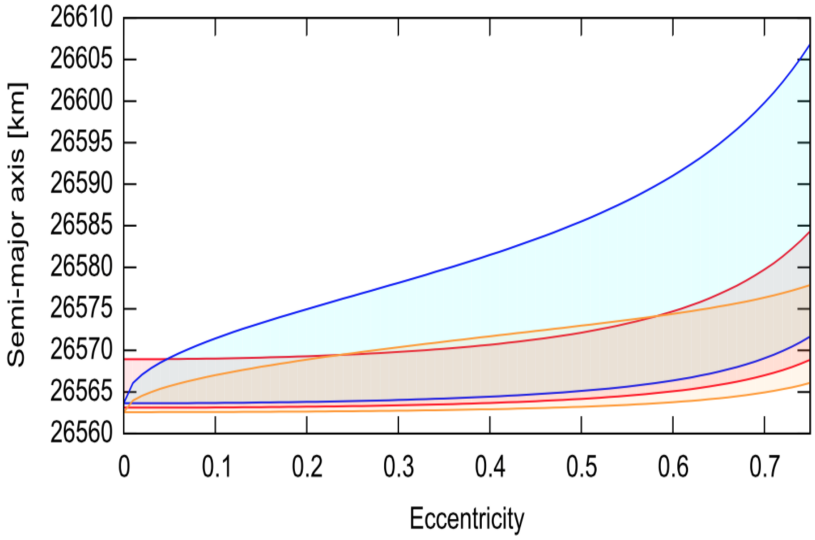

Figure 2.1 – Exemplary superposition of resonances corresponding to three various multiplets of 2:1 resonance for $i = 55°$. Each resonance is traced with its width calculated as if it was isolated. From Daquin (2015).

$$-\frac{15}{8}\sin i(1-\cos i)^2\frac{131e^4}{128}\sin(M-2\theta_\oplus-3\omega+2\Omega-2\lambda_{32})\Big)\,, \tag{2.1.17}$$

with λ_{22} and λ_{32} being the phases. In most cases, we are interested in long-term dynamics, therefore the Hamiltonian is averaged and the non-resonant part, $\mathscr{H}_{nonres}$, is dropped.

Celletti and Galeş (2014) show that in case of 2:1 resonance, there are three terms from the above expansion that dominate the dynamics and have comparable magnitude, but none of them prevails over the others. These are the terms with resonant angles being $(M-2\theta_\oplus+2\omega+2\Omega-2\lambda_{22})$, $(M-2\theta_\oplus+2\Omega-2\lambda_{22})$ and $(M-2\theta_\oplus+\omega+2\Omega-2\lambda_{32})$. The presence of several sets of resonant indices means that the resonance actually splits into multiple resonances satisfying the condtion (2.1.10), which have different values of resonant semi-major axis. As they are separated by only several kilometers, they may overlap with each other (Fig. 2.1) if the distance between them is smaller than their respective widths (Chirikov, 1979). The interactions between harmonics lead to the formation of chaotic zones.

2.1.2 Lunisolar resonances

The lunisolar resonances are related to the disturbing potential of a third body – the Sun or the Moon. They have a much longer timescales than tesseral resonances, which may be a reason why they were largely overlooked since early works (Hughes (1980); Ely and Howell (1997); Breiter (2001)). The general form of the perturbing potential

in the geocentric reference frame is

$$U_{3b} = -\frac{\mu_{3b}}{||\vec{r} - \vec{r}_{3b}||} + \mu_{3b}\frac{r\, r_{3b}}{||\vec{r}_{3b}||}, \tag{2.1.18}$$

with $\vec{r}$ being the position vector of the satellite from the centre of the Earth, $\vec{r}_{3b}$ – from the centre of the Earth to the perturbing body, and μ_{3b} is the gravitational parameter of the third body. Expressing this potential in terms of Fourier series with the use of Keplerian elements, we have for the Moon

$$U_M = \sum_{m+0}^{2}\sum_{s=0}^{2}\sum_{p=0}^{2} h^M_{2-2p,m,\pm s}(a,e,i)\cos\psi^M_{2-2p,m,\pm s}, \tag{2.1.19}$$

with the critical angle

$$\psi^M_{2-2p,m,\pm s} = (2-2p)\omega + m\Omega \pm s(\Omega_M - \frac{\pi}{2} - y_s\pi), \tag{2.1.20}$$

with y_s being equal to 0 for s even and to 1/2 otherwise (Daquin, 2015).

Similarly, the potential related to the Sun's gravity is

$$U_S = \sum_{m=0}^{2}\sum_{p=0}^{2} h^S_{2-2p,m}(a,e,i)\cos\psi^S_{2-2p,m}, \tag{2.1.21}$$

with

$$\psi^S_{2-2p,m} = (2-2p)\omega + m(\Omega - \Omega_S) \tag{2.1.22}$$

(Daquin, 2015). The full expressions of h^M and h^S harmonics can be found in Kaula (1966).

The resonance emerges when the critical angle is constant:

$$\dot{\psi}^M_{2-2p,m,\pm s} = (2-2p)\dot{\omega} + m\dot{\Omega} \pm s\dot{\Omega}_M = 0, \tag{2.1.23}$$

in case of the Moon; as $\dot{\Omega}_S = 0$, the resonance with the Sun appears when

$$\dot{\psi}^S_{2-2p,m} = (2-2p)\dot{\omega} + m\dot{\Omega} = 0. \tag{2.1.24}$$

As the mean anomaly is absent from the equations, the value of semi-major axis is not affected by these resonances.

Within the MEO region, the tesseral perturbations due to J_2 are at least an order of magnitude bigger than the lunisolar effects (Daquin et al., 2016). It is therefore possible to approximate $\dot{\omega}$ and $\dot{\Omega}$ with (2.1.4) and (2.1.5), respectively, ignoring the variations due to the lunisolar perturbations. With that in mind, eqs. (2.1.23) and (2.1.24) define the curves of the lunisolar resonances in the (e,i) phase space (Fig. 2.2). The shaded areas indicate the width of a resonance. It is visible that some of these resonances (specifically, at the inclinations equal to 46.4°, 56.1°, 63.4°, 69.0°, 73.2°and 90°) are independent of the orbit eccentricity. Each of these splits into multiplet-like structure with $s \in \{1,2\}$, and the curves intersections indicate the regions where multiple resonances dominate the dynamics. These superpositions produce chaos and may lead to large drifts in eccentricity (Daquin et al. (2016); Gkolias et al. (2016)).

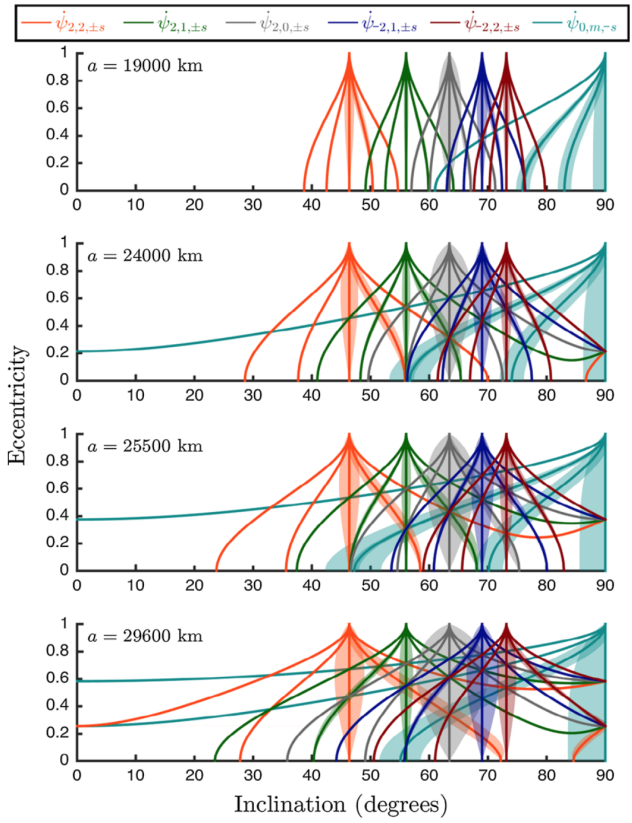

Figure 2.2 – Centers (solid lines) and widths (shaded areas) of lunisolar resonances for exemplary semi-major axes within the MEO region. At lower altitudes, the widths are narrow and therefore, the dynamics should be dominated by regular orbits. At bigger values of a, the libration regions are wider and the resonances overlap, creating chaotic domains. From Daquin et al. (2016).

2.1.3 Chaos indicators

In efforts to identify the chaotic behaviours in the system, two kinds of indicators come into play: variational and spectral methods. Variational indicators rely on analysis of behaviour of a tangent vector assosciated with the orbit under consideration. The spectral methods, on the other hand, focus on one specific orbit and inspect the frequency spectrum drawn from its numerical approximation. Calculation of such chaos indicators over a grid of initial conditions allows to form stability maps, which clearly depict the domains of existence of stable or chaotic motions.

2.1.3.1 MEGNO

The indicator primarily used during this thesis is MEGNO. It was first described by Cincotta and Simó (2000), and was proven to be a robust tool in the study of dynamical problems (e.g. Goździewski et al. (2001); Breiter et al. (2005); Valk et al. (2009)). The acronym stands for Mean Exponential Growth of Nearby Orbits, and it belongs to the variational methods based on the use of Lyapunov exponents.

Let $\vec{\delta}_\phi$ be a deviation vector, representing a distance between two close trajectories. Its evolution is described by

$$\dot{\vec{\delta}}_\phi = \frac{\mathrm{d}}{\mathrm{d}t}\vec{\delta}_\phi(t) = \vec{J}(\phi(t))\vec{\delta}_\phi(t), \quad \text{with} \quad \vec{J}(\phi(t)) = \frac{\partial \vec{f}}{\partial \vec{x}}(\phi(t)) \tag{2.1.25}$$

(terms of $\mathscr{O}(\vec{\delta}^2)$ are omitted), where $\vec{J}(\phi(t))$ is the Jacobian matrix of the differential equations system. MEGNO is defined as

$$Y_\phi(t) = \frac{2}{t}\int_0^t \frac{\dot{\delta}_\phi(s)}{\delta_\phi(s)}\, s\,\mathrm{d}s, \quad \text{with} \quad \delta_\phi = ||\vec{\delta}_\phi(t)|| \tag{2.1.26}$$

(Cincotta and Simó, 2000). To ensure convergence and remove oscillations, the mean value of $Y_\phi(t)$ is used:

$$\bar{Y}_\phi(t) = \frac{1}{t}\int_0^t Y_\phi(s)\,\mathrm{d}s. \tag{2.1.27}$$

For quasi-periodic orbits, $\bar{Y}_\phi(t)$ converges to 2, while in case of chaotic motion, δ grows linearly towards infinity. For orbits close to stable periodic ones, $\bar{Y}_\phi(t)$ tends asymptotically to 0 (Cincotta et al., 2003).

MEGNO was implemented in the NIMASTEP software by its author, N. Delsate (Delsate, 2011). The initial tangent vector is chosen randomly, in order to avoid artificial formation of low MEGNO zones due to the proximity of $\vec{\delta}_\phi(0)$ to the minimum Lyapunov exponent direction.

2.1.3.2 FLI

Similarly to MEGNO, the Fast Lyapunov Indicator (FLI; first introduced in Froeschlé et al. (1997)) is a variational method based on the analysis of the tangent vector evolution. It can be defined as the largest Lyapunov characteristic exponent at a fixed time $t = T$:

$$\mathrm{FLI}(t) = \sup_{0<t\geq T} \ln \delta_\phi(t). \tag{2.1.28}$$

The character of the orbit is then distinguished in comparison with its vicinity (the higher the value, the more chaotic the motion).

2.1.3.3 Frequency analysis

The idea is based on the KAM theory stating that in case of regular motion, the solutions of the system are confined to invariant tori, therefore having constant frequencies. The variation of these frequencies is an indication of chaos. The method consists

of approximating the signal with N harmonics, starting from numerical data of $f(t)$ on a finite time interval

$$f(t) = \sum_{k=1}^{\infty} a_k e^{i\nu_k t}, \qquad f'(t) = \sum_{k=1}^{N} a'_k e^{i\nu'_k t}, \tag{2.1.29}$$

where $f'(t)$ is the approximation of the signal, and ν_k and ν'_k are the frequencies. The frequencies ν'_k are found with the use of FMA (Frequency Map Analysis) algorithm, detailed in Laskar (1993). The code that was used in this thesis was developed by B. Noyelles.

2.2 Numerical investigations of the chaotic MEO zones

With the use of NIMASTEP software, described in the Introduction, and the MEGNO indicator implemented in it, we were able to integrate the osculating Cartesian equations of motion in order to produce several stability maps, considering gravitational perturbations due to the geopotential only (Sec. 2.2.1), or the geopotential and Sun and Moon attraction (Sec. 2.2.2). The work was facilitated by the use of clusters, belonging to the CÉCI consortium of high-performance computing centers of several Belgian universities. The first step in this analysis is to compare these maps with those existing in the literature. All the numerical simulations in the following were performed with the use of Adams-Bashforth-Moulton method of order 10 (the next chapter contains more information regarding the numerical integration).

2.2.1 Tesseral resonances

In Celletti and Galeş (2014), the authors use the Hamiltonian formalism and the equations averaged over short periods to present a cartography of 1:1 and 2:1 tesseral resonances with the use of FLI indicator. In Fig. 2.3a, drawn from the article, they plot the FLI values for the Hamiltonian (2.1.15), with the geopotential developed till degree 3, retaining only the dominant terms in (2.1.17), as described at the end of Sec. (2.1.1). The plot demonstrates how the chaotic zones occupy big portions of space when the resonances overlap, even for non-elevated eccentricity values as $e = 0.1$. Fig. 2.3b is a recreation of this map with the use of MEGNO, where the whole system was integrated. 108 000 orbits were propagated on a 40 y timescale. All the important features obtained with the main terms only are clearly distinguishable; the shape of the chaotic zone is preserved, as well as the stable regions within it. Moreover, the precision of our results with MEGNO is much higher compared to the results presented in Celletti and Galeş (2014), due to a higher number of orbits that were integrated; more detailed structures are clearly discernible in Fig. 2.3b. The stable regions within the chaotic sea are probably to be associated with secondary resonances in the system, but further study would be required to determine their nature.

Fig. 2.4 presents the stability maps for $e = 0.5$. Only the harmonics with order and degree 2 were used here. Fig. 2.4a was taken from Daquin et al. (2015), where the authors' aim is to test the robustness of tesseral chaos to the averaging procedure. The

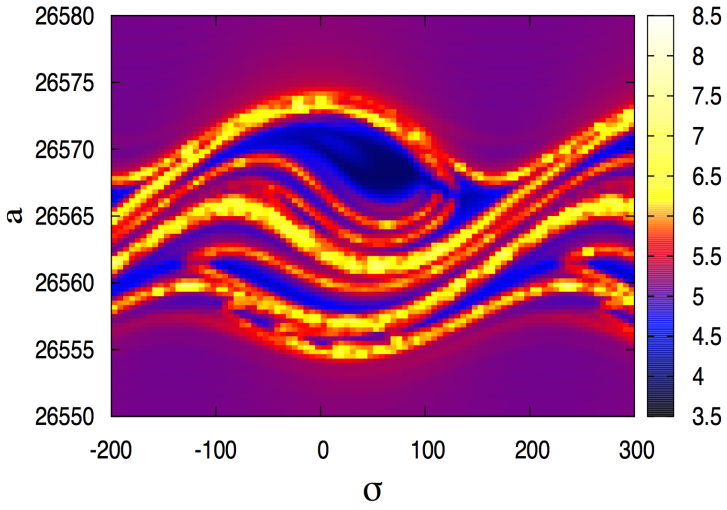

(a) From Celletti and Galeş (2014).

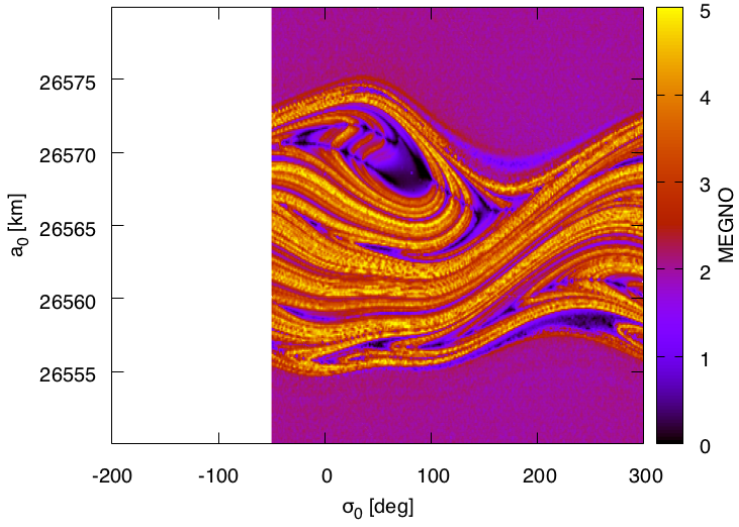

(b) Recreation of the above with the use of MEGNO.

Figure 2.3 – Comparison of FLI and MEGNO maps for the 2:1 tesseral resonance, with only the dominant terms of the geopotential (a), or the geopotential described by all the spherical harmonics till degree 3 (b). Initial conditions: $e = 0.1$, $i = 20°$, $\omega = \Omega = 0°$. Integration time was 40 y. The angle σ is $\sigma = M - 2\theta_{\oplus} + \omega + 2\Omega$.

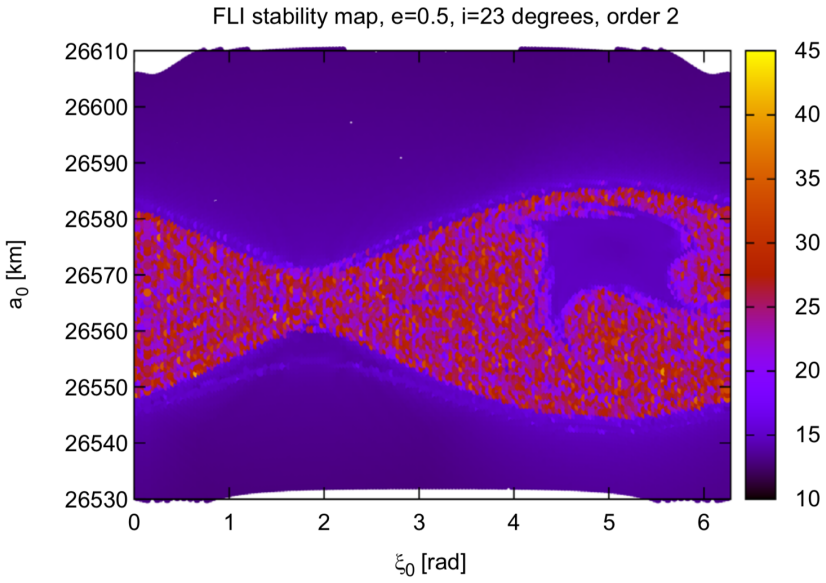

(a) From Daquin et al. (2015).

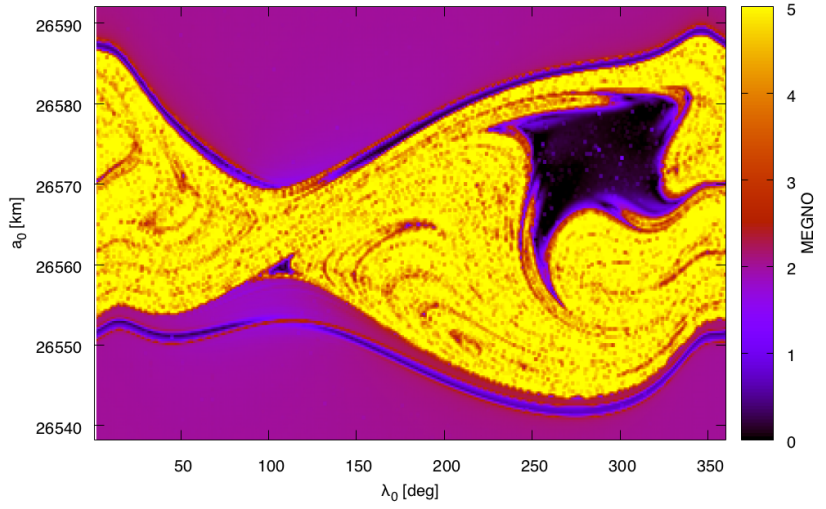

(b) Recreation of the above with the use of MEGNO.

Figure 2.4 – Tesseral chaos around the 2:1 resonance as obtained in terms of FLI by Daquin et al. (2015) (a) and with MEGNO (b). The initial conditions are: $e = 0.5$, $i = 23°$, $\omega = 90°$, $\Omega = 270°$. The simulation time is 40 y. $\xi_0 = \lambda_0 = M + \omega + \Omega$.

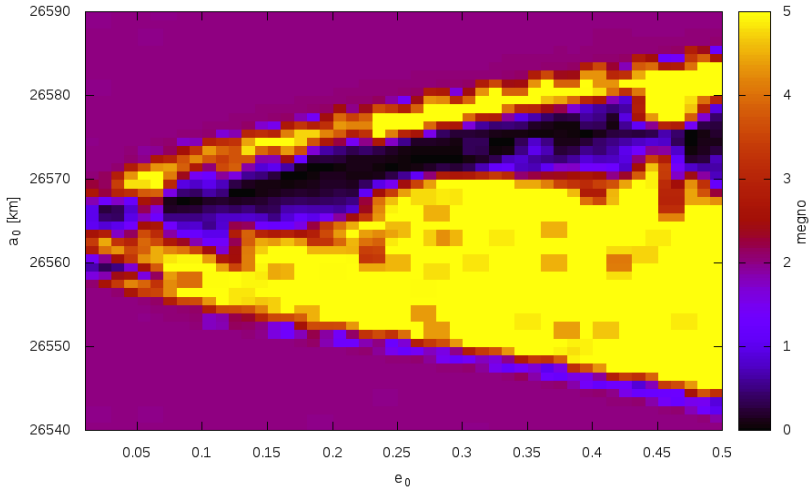

Figure 2.5 – MEGNO values in semi-major axis – eccentricity phase space for 2:1 tesseral resonance, with the force model being limited to 2nd order of geopotential expansion. The initial conditions are: $i = 23^\circ$, $\omega = 90^\circ$, $\Omega = 270^\circ$, $M = 300^\circ$. 4 800 orbits were propagated over 100 y. A stable zone being preserved along with eccentricity growth is evident.

map was produced in terms of FLI values, with the osculating equations propagated over 40 y, but is presented in terms of the mean variables to allow for a comparison with that obtained with the averaged system. Fig. 2.4b is our version of it, made with the use of MEGNO and osculating theory, hence the difference in shape. We integrated 77 900 orbits over 40 y. Again, the precision obtained in the MEGNO map is much better than that in the FLI map. Some additional stable structures are noticeable, e.g. the thin line of low MEGNO (close to 0) below the main chaotic zone. Nonetheless, the same conclusions can be drawn from both graphs: the maximum width of the resonant zone is evidently bigger than in case of $e = 0.1$, presented above. This point is further corroborated in our Fig. 2.5, which shows (in terms of MEGNO values) how the resonance width becomes larger with the eccentricity increasing, as well as on Fig. 2.6, similar to Fig. 2.4, but calculated with $e = 0.1$ (77 900 orbits). A stable region is preserved within the chaotic zone regardless of the eccentricity. This same region is also apparent to occupy a big portion of space in Fig. 2.4. A possible secondary resonance within the system could be a plausible explanation for this structure; while the superposition of resonant multiplets creates chaos, a secondary resonance may produce such stable region within the chaotic sea. What is more, the addition of other perturbations, such as Sun or Moon attraction, does not abolish it. The Hamiltonian that describes the problem has the form

$$H = -\frac{\mu^2}{2L^2} + \frac{\mu^2 r_E^2 J_2}{a^3}\left(\frac{3}{4}\sin^2 i - \frac{1}{2}\right)(1-e^2)^{-3/2}$$

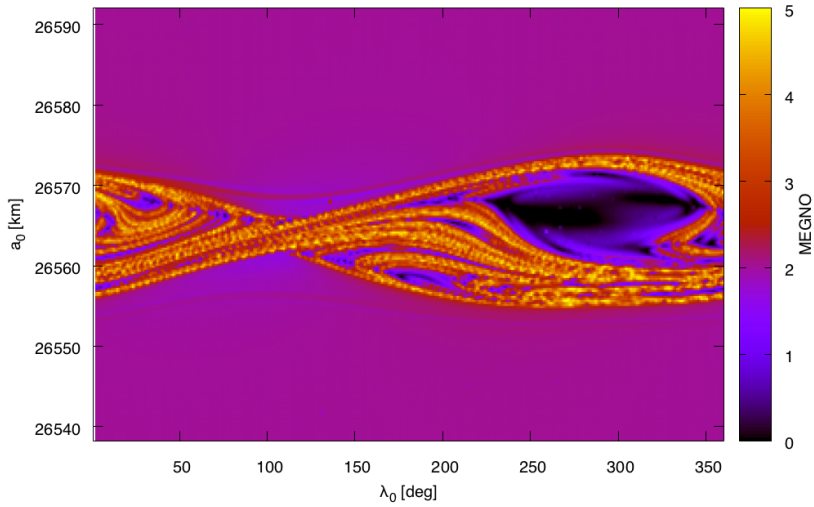

Figure 2.6 – MEGNO map of tesseral chaos for initial conditions $e = 0.1$, $i = 23°$, $\omega = 90°$, $\Omega = 270°$, with 77 900 orbits propagated over 40 y.

$$+\frac{\mu^2 r_E^2 J_{22}}{a^3}\left(\frac{3}{4}(1+\cos i)^2\left(-\frac{e}{2}+\frac{e^3}{16}\right)\cos(M-2\theta_\oplus+2\omega+2\Omega)\right.$$
$$+\frac{3}{2}\sin^2 i\left(\frac{3}{2}e+\frac{27}{16}e^3\right)\cos(M-2\theta_\oplus+2\Omega)$$
$$\left.+\frac{3}{4}(1-\cos i)^2\frac{67e^3}{48}\cos(M-2\theta_\oplus-2\omega+2\Omega)\right). \quad (2.2.1)$$

Within the portion of space that contains the stable region, $(M-2\theta_\oplus+2\omega+2\Omega)$ is the resonant angle that librates, whereas the two remaining ones circulate. However, the frequency analysis of these angles performed on the stable orbits shows that $(M-2\theta_\oplus+2\omega+2\Omega)$ and $(M-2\theta_\oplus+2\Omega)$ have very similar periods (see Table 2.2), meaning that there may be a secondary resonance between them. However, the fact that the three terms are of comparable magnitude makes the problem more difficult, as none of them can be seen as a perturbation to the others. Thus, the usual perturbation approach cannot be applied, and the question remains open.

The comparison of FLI and MEGNO maps, and the finer details found with the latter could be in itself published in an article form. As for now, these results were presented at the CelMec conference in 2017.

En route to a more realistic model, Fig. 2.7 and 2.8 present the broadening of chaotic regions with the addition of higher terms of geopotential (2 and 3, respectively). As the coefficients of spherical harmonics diminish with the order, further expansion does not affect the stability in any significant way (Fig. 2.9). The eccentricity growth on the other hand can lead to destruction of the stable zones and extension of the resonant region (Fig. 2.10). All four of the above mentioned graphs were created

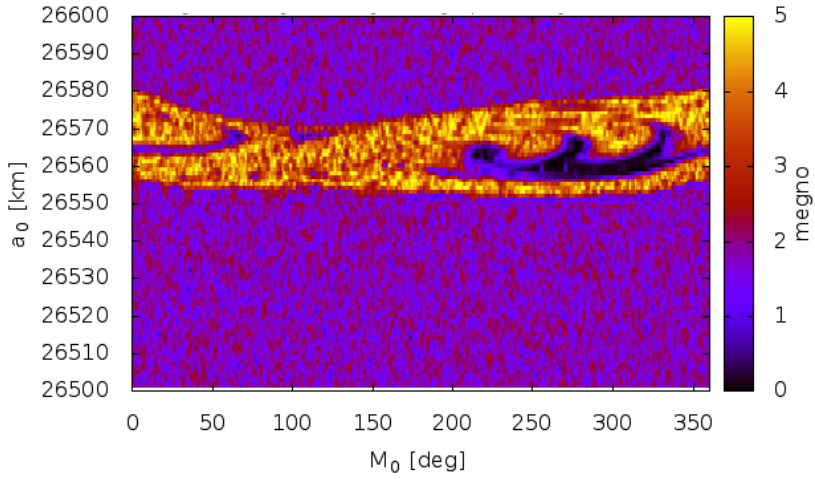

Figure 2.7 – MEGNO stability map for 2:1 tesseral resonance. Initial conditions: $e = 0.3$, $i = 23°$, $\omega = 0°$, $\Omega = 0°$, with geopotential expanded till degree 2. The integration time was 40 y.

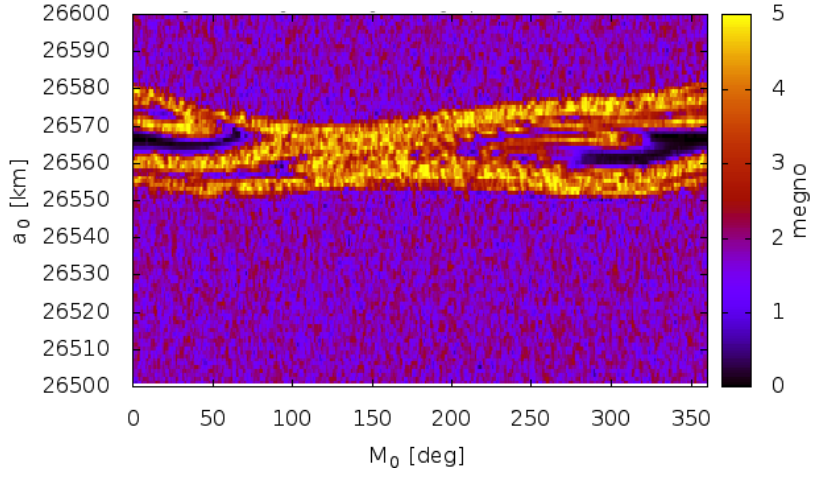

Figure 2.8 – Similarly as above, but with the order of the highest terms of included harmonics being 3.

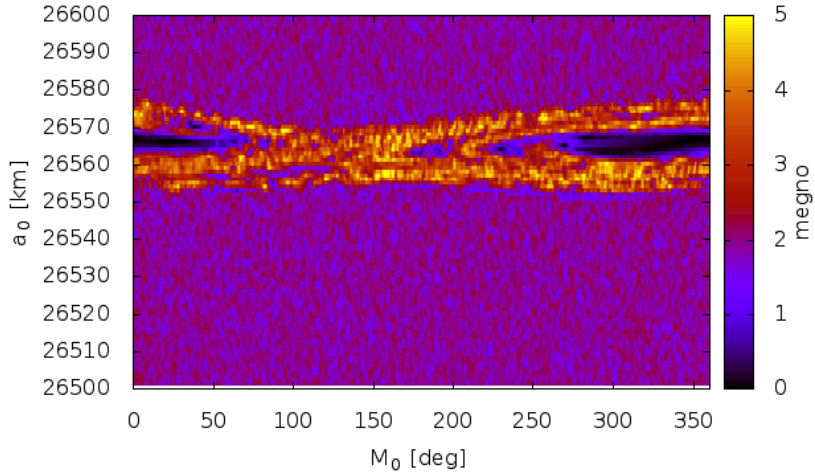

Figure 2.9 – 2:1 resonant zone under the influence of the geopotential modeled by a spherical harmonics expansion up to order 5, with initial conditions: $e = 0.2$, $i = 23°$, $\omega = 0°$, $\Omega = 0°$.

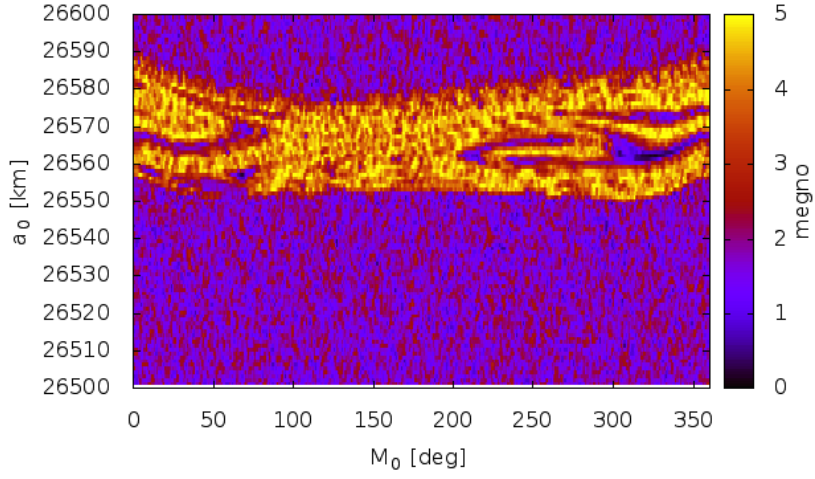

Figure 2.10 – Similar as in previous graph, but with $e = 0.4$.

by propagating 36 100 orbits over 40 y.

2.2.2 Lunisolar resonances

Lunisolar resonances form a dense network of chaotic bands in the $e-i$ phase space, where many regular orbits persist within considerable stable regions. Fig. 2.11 and 2.12 present an example of such a mesh at $a_0 = 29\,600$ km. Both figures were obtained by propagating 25 000 orbits over 200 y. As demonstrated by Daquin et al. (2016), even the very basic model of geopotential perturbations described by oblateness (J_2) only and the Moon as a sole third-body perturber suffices to detect the prevalent features of the secular resonances. As the phase space is in fact of six dimensions, the stability maps are difficult to present; hence the only difference between two sets of maps is the value of initial argument of perigee. This kind of mesh and overlapping of resonances dominate the dynamics at bigger values of semi-major axis, as per Fig. 2.2 (Daquin et al., 2016), and it allows the orbits of satellites or space debris that find themselves in such resonances to undergo a significant eccentricity growth on relatively short timescales – the orbits can traverse large portions of eccentricity range through the chaotic zones. They are however confined within several degrees in inclination. It is worth noting that on the verge of these resonances, we can find the Galileo navigational satellites - the inclination and semi-major axis of the constellation corresponds to the resonant values. The resonances are therefore considered as disposal regions for this system (Rosengren et al., 2017).

Table 2.2 – Dominant periods (in years) of angles $\sigma_1 = (M - 2\theta_\oplus + 2\omega + 2\Omega)$ and $\sigma_2 = (M - 2\theta_\oplus + 2\Omega)$.

σ_1	σ_2
9.7555	4.5572
8.5537	3.1062
11.3632	8.5518
4.5561	2.9731
13.5979	4.8794
69.2139	69.2576
34.5340	1.1789
17.0311	2.3560
4.8739	7.6071
22.9327	9.7536
3.1092	3.2519
	4.2785
	34.5279
	2.4386
	5.2436
	9.7740
	11.3323

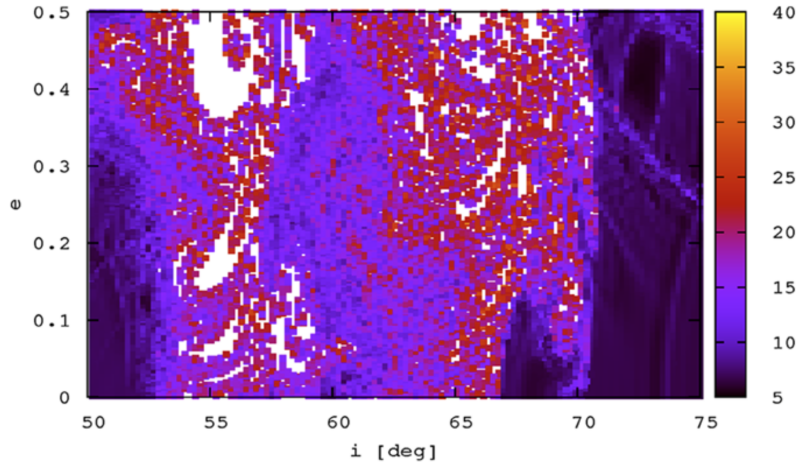

(a) From Daquin et al. (2016).

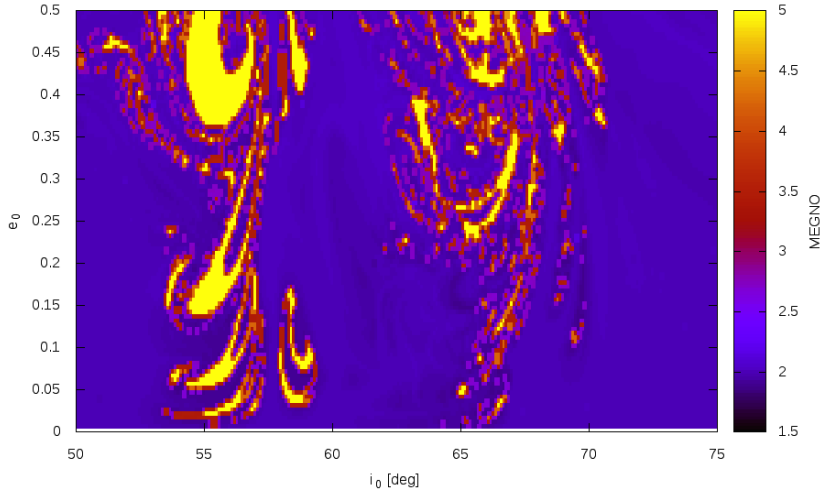

(b) Recreation of the above with the use of MEGNO.

Figure 2.11 – FLI (from Daquin et al. (2016)) and MEGNO stability maps of lunisolar resonances at $a_0 = 29\,600$ km. The remaining initial conditions are: $\omega = 30°$, $\Omega = 120°$. The initial epoch is March 2, 1969, and the integration time is 200 y.

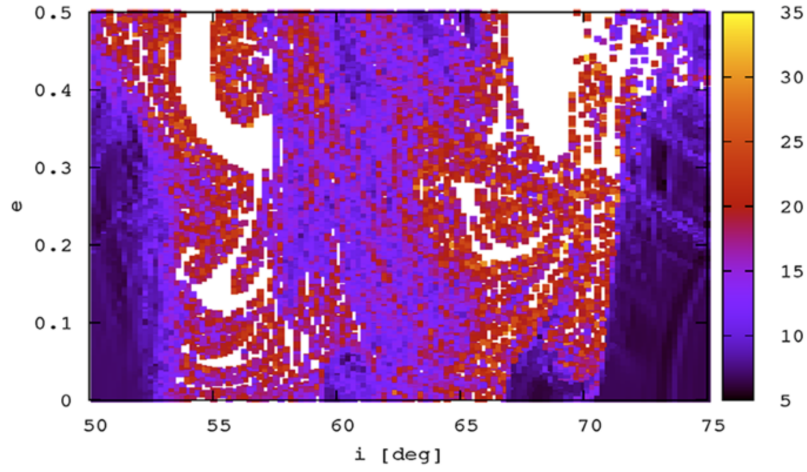

(a) From Daquin et al. (2016).

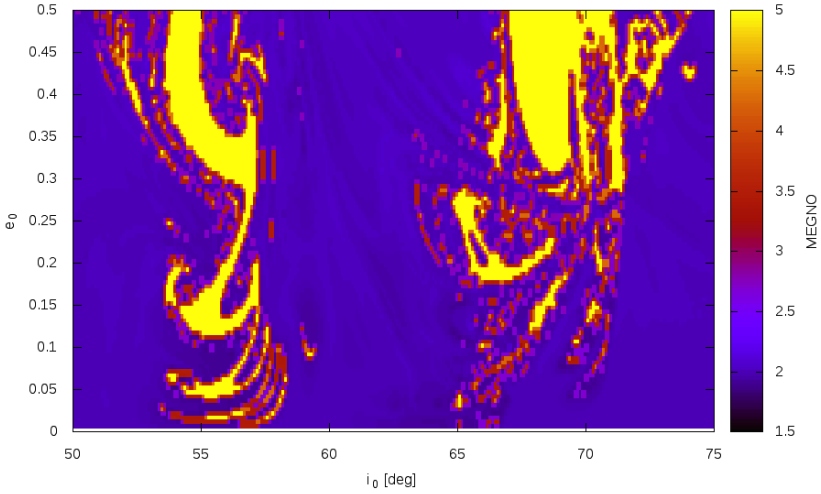

(b) Recreation of the above with the use of MEGNO.

Figure 2.12 – Similarly as in Fig. 2.11, but with initial $\omega = 75°$.

2.3 Conclusions

With the use of the in-house NIMASTEP integrator and the MEGNO chaos indicator, we produced several stability maps of tesseral and lunisolar resonant zones. Some of them are reproductions of previous work found in literature, but with much better resolution (due to the higher number of considered orbits), which allows to identify more features, and reveals further complexity of the dynamics in the region. We also discussed some supposed secondary resonances in tesseral case, identifying the potential angles that could correspond to this phenomenon. To our knowledge, this was the first attempt at recognizing these resonances in MEO (some secondary resonances between the geostationary resonant angle and the longitude of the Sun, related to the solar radiation pressure, were identified in GEO, see Lemaitre et al. (2009)); however, due to the comparable magnitude of perturbing terms, the problem requires some more advanced analytical methods to be applied. Both tesseral and lunisolar resonances could be important in space debris management, as they may serve as reservoirs of graveyard orbits, or as a basis for deorbiting strategies in case of eccentricity growth (see e.g. Rossi et al. (2009); Radtke et al. (2015)).

Chapter 3

Numerical integration of chaotic orbits

In recent decades, numerical integration has become a powerful tool in Celestial Mechanics. Due to the technological advancements that allowed to reduce computational costs and time, it is now regularly used wherever analytical methods cannot be applied. It provides an approximate solution when the equations are not possible to solve in an exact manner, or gives the opportunity to explore long-term effects of the problem at hand. Many important results could not have been obtained without referring to numerical methods. This is notably valid in the field of Orbital Dynamics. As seen in the previous chapter, numerical methods help to identify the regions of chaotic and regular motions throughout a six-dimensional phase space by computing chaos indicators and composing stability maps and atlases.

Nevertheless, the sensitive dependence on initial conditions of chaotic systems means that, due to inevitable numerical noises (such as truncation and round-off errors), some quantities cannot be accurately computed. The emerging question of which quantities we can still estimate with a relative reliability remains unaswered.

3.1 Motivation

The orbits that we consider are mainly those close to 2:1 tesseral resonant surface, with a small detour into lunisolar resonances. As discussed in the previous chapter, the interactions between neighbouring resonances generate chaotic regions, where the predictability of the orbital evolution is limited. With the use of numerical integration and chaos indicators, stability maps can be produced. However, if a single orbit is considered, one can notice that different trajectories are obtained if various integration time steps are used. Fig. 3.1 presents an example of this effect: plotting semi-major axis resulting from simulations performed with the Adams-Bashforth-Moulton

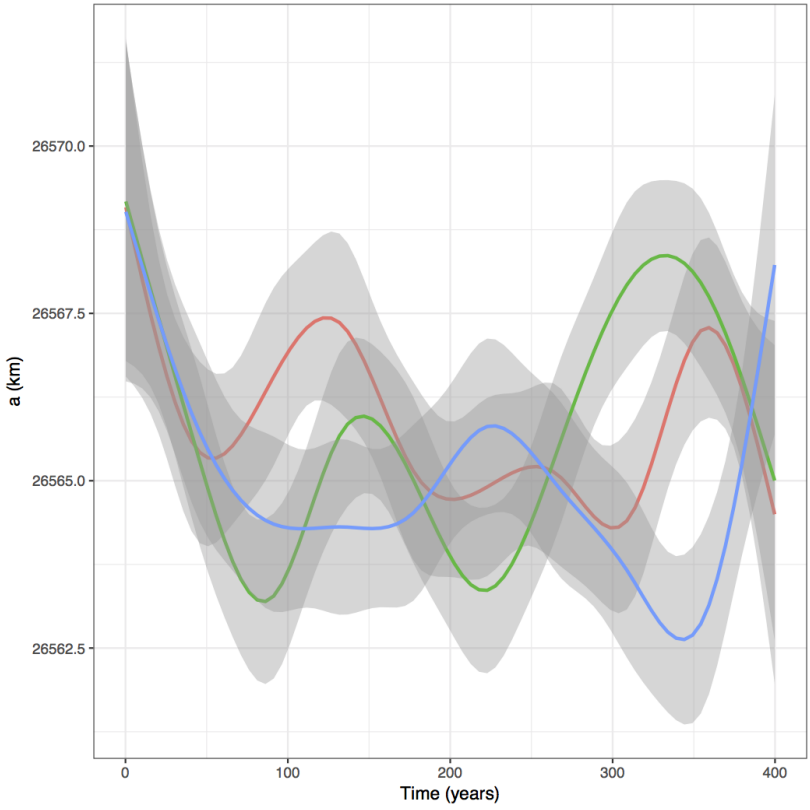

Figure 3.1 – Long-term evolution of a chaotic orbit close to 2:1 tesseral resonance, traced with three different time steps (red – 30s, green – 60s, blue – 100s). The integration was performed with the use of ABM10 scheme. Initial conditions are: $a = 26\ 569$ km, $e = 0.5$, $i = 23°$, $\omega = 90°$, $\Omega = 270°$. The geopotential was developed till degree 2. The graphs were smoothed to remove oscillations so that the general trends are visible. The divergence of orbits is apparent already after around 15 y.

integrator of order 10, with time steps of 30, 60 and 100 s, we have three different evolutions, diverging already after around 15 y. It is clear that a trajectory is not accurately computed and it depends on its integration parameters. Reducing the time step seems to prolonge the interval on which the trajectory is well computed. However, 30 s is already a very small time step, especially on timescales as long as 400 y. Nevertheless, the information regarding stability, calculated with different variational indicators, remains valid, as visible when comparing maps generated by different groups of researchers (cf. graphs in previous chapter). Despite the fact that these groups would probably obtain different numerical orbits with their own orbital propagators, their variational maps would still be identical. Therefore, some 'observables' seem to be more robust to perturbations than others. The same applies to the

information extracted from their time series. A similar problem exists in the realm of Molecular Dynamics: even though the numerical trajectories are correct for only very short times, the statistical information derived from these simulations is still accurate (Tupper, 2008). It is therefore important to know what quantities can be computed accurately in case of chaotic orbits.

The work described in this chapter was carried out in collaboration with Dr Jérôme Daquin. The issue was first identified during the conduction of numerical simulations described in the previous chapter, when the use of too big of a stepsize produced erroneous stability maps of tesseral chaos.

In the following, we mainly performed simulations with two 'popular' constant time step integrators, the single-step classical Runge-Kutta method of order 4 (RK4) and the multi-step Adams-Bashforth-Moulton method of order 10 (ABM10). RK4 is one of the most widely used algorithms. However, it is only conditionally stable, and might require a very small time step in order to keep the error at intended level. Furthermore, RK4 requires 4 evaluations of the derivative per one step of integration. ABM10 is a faster and more precise integrator. It is a multi-step predictor-corrector algorithm, with Adams-Bashforth method used to predict the first value and an implicit Adams-Moulton scheme used to further correct it. With half a number of function evaluations of RK4, the method allows to obtain high precision of integration. As we integrate the full (osculating) system and not the averaged one, this choice allows to reduce computational costs and integration time. The symplectic schemes are also briefly discussed.

3.2 Numerical experiments

The disparities discussed above hold for other resonances as well. Fig. 3.2 gives two examples of 3:2 and 5:3 tesseral resonances, whereas Fig. 3.3 shows the evolution of a trajectory starting within a chaotic sea related to a lunisolar resonance. In all these cases, the ABM10 integrator was used. The divergencies are clearly visible in all three graphs.

First of all, an important issue is the conservation of energy, which is a first integral of the system. Fig. 3.4 demonstrates its variations over 200 y when ABM10 is used – it is preserved up to 4%, even though the scheme is not symplectic. An error on a similar level was produced with RK4 integrator.

Following some ideas from the realm of Molecular Dynamics (see e.g. Tupper (2008); however, we consider only a single initial condition and discard the spatial averaging idea), an observable that could be expected to be conserved regardless of a time step is the distribution of the semi-major axis. The histograms of such a distribution are calculated by first dividing the range of values that the semi-major axis achieves during its evolution into "baskets" of 1 km span. Then, we count the number of appearances of values falling into a specific "basket" range. Fig. 3.5 presents three such histograms that were computed for the three trajectories of Fig. 3.1. It is apparent that the distribution of the semi-major axis does not converge. Any statistical information extracted from the histograms is thus not accurate either. The same

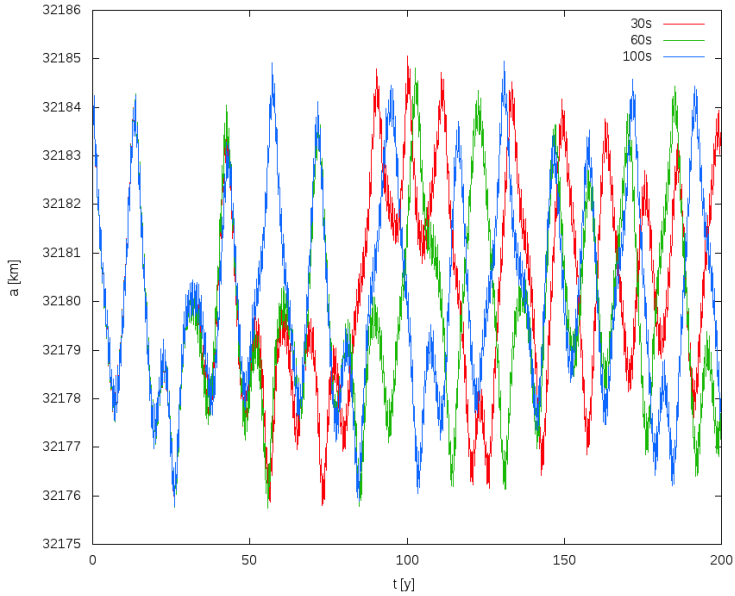

(a) 3:2 tesseral resonance

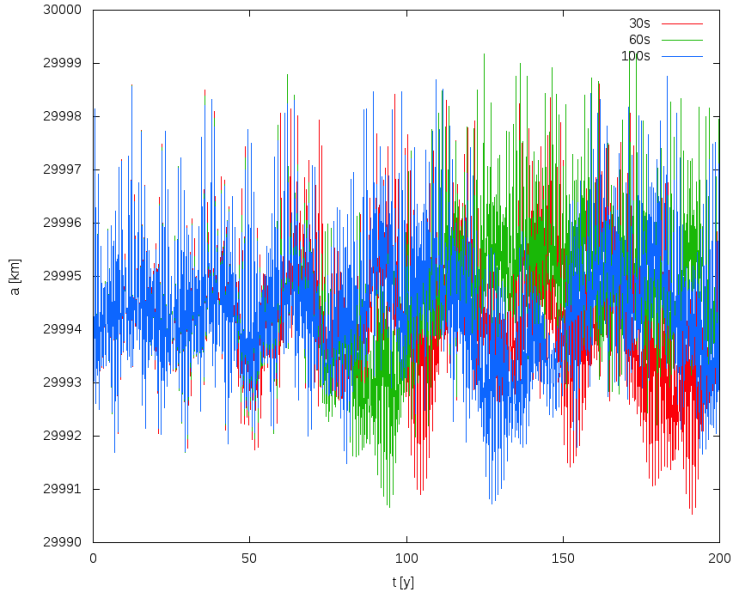

(b) 5:3 tesseral resonance.

Figure 3.2 – Examples of the problem in case of other tesseral resonances: 3:2 (a) and 5:3 (b). Initial conditions: (a): $e = 0.1$, $i = 10^\circ$, $\omega = \Omega = 0^\circ$, $M = 83^\circ$; (b): $e = 0.3$, $i = 45^\circ$, $\omega = \Omega = 0^\circ$, $M = 57.6^\circ$, all chosen within the chaotic sea of a relevant resonance. The geopotential was expanded till degree 5. The orbits were propagated with ABM10 integrator over 200 y. The discrepancies between trajectories obtained with various time steps are evident.

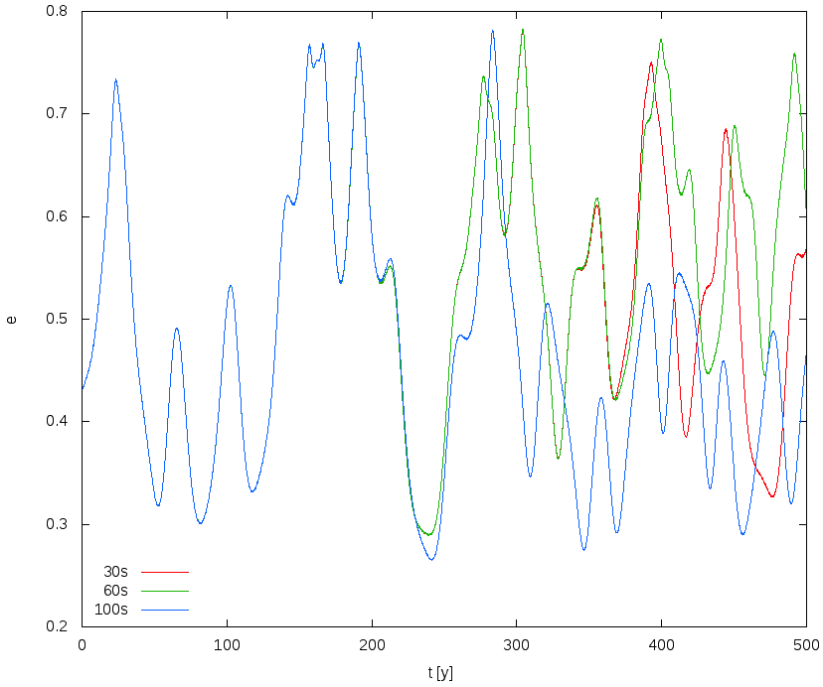

Figure 3.3 – Eccentricity evolution of a trajectory in a chaotic region of lunisolar resonance. Effects of J_2, Sun and Moon were taken into account. Initial conditions are: $a = 29\ 600$ km, $e = 0.43$, $i = 64.8°$, $\omega = 30°$, $\Omega = 120°$, $M = 0°$. Integration time is 500 y, and the integrator is ABM10.

kinds of experiment conducted for other initial conditions known to be chaotic do not invalidate this observation (Fig. 3.6).

The analysis of Lyapunov times could provide an insight into the limits of the predictability of the system. We have examined their values for three different timesteps for several initial conditions known to belong to the tesseral chaotic sea, and each time we have obtained different values for different h. They remain of the same order though, that is, of just a couple of years (3-8 y). Similarly, the correlation time τ_C could also serve as a good indicator of predictability horizon. For practical applications, the correlation decay of a particular observable of interest for the problem is monitored (Wiggins and Ottino, 2004). As it was mentioned, the macroscopic variable of interest for the tesseral problem is related to the semi-major axis; we thus turn to monitoring its correlation decay.

The autocorrelation relates quantities that are θ-apart. We introduce the following time-average notation: $\langle f_\nu \rangle = \lim_{t\to+\infty} \frac{1}{t} \int_0^t f(\tau+\nu)\,\mathrm{d}\tau$. The (normalized) autocorrelation coefficient $C(\theta)$ for the semi-major axis then reads

$$C(\theta) = \frac{\langle (a_0 - \langle a_0 \rangle)(a_\theta - \langle a_\theta \rangle) \rangle}{\sigma^2(a)}. \tag{3.2.1}$$

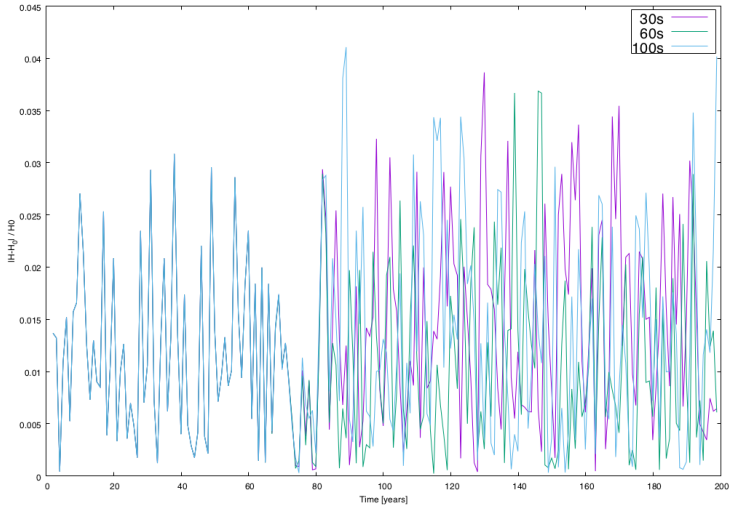

Figure 3.4 – The Hamiltonian first integral for the three time steps used in Fig. 3.1. The energy is conserved up to 4% over a period of 200 y when ABM10 integrator is used.

Looking at $\lim_{\theta\to+\infty} C(\theta)$ for various known chaotic initial conditions, we find a fast decay of the correlation coefficient as a function of the lag-time θ. The correlation time τ_C is then obtained as the smallest time $t_\star$ for which the absolute value of the correlation coefficient is smaller than $1/e$ for all $t \geq t_\star$ (Tsiganis et al., 2002). Alternatively (e.g. Allen (2004)), we may estimate τ_C from the exponential correlation decay as the characteristic time over which the decay occurs

$$C(\theta) \propto e^{-\theta/\tau_C}. \tag{3.2.2}$$

We estimated τ_C to be typically around 10 years (i.e. $\sim 7 \times 10^3$ orbital revolutions). This means that the experiments conducted in Figs. 3.5 and 3.6 satisfy

$$\tau_{\text{run}} \sim 40\tau_C, \tag{3.2.3}$$

which can be considered much larger than one. Let us note that from this estimation, it follows that τ_C is of similar magnitude as the Lyapunov time (*strong chaos*).

Even with the Lyapunov times being inconsistent, the stability maps computed with three different time steps agree perfectly well. Fig. 3.7 presents zoomed-in portions of maps of Fig. 2.4b of previous chapter. The chosen region contains the 'main' separatrix, the border between stability island of secondary resonance and chaotic sea, and a high number of chaotic orbits. Fig. 3.7a and 3.7b were traced with a time step of 30 and 100 s, respectively, and the ABM10 integrator, whereas Fig. 3.7c and 3.7d with 30 and 60 s plugged into the RK4 integrator (100 s is already too big for RK4). All four graphs are in excellent agreement.

As far as lunisolar resonances are considered, the direct integration of osculating equations yields some differences when compared to the maps calculated with averaged theory. In Fig. 3.8, we plot a zoomed portion of the phase space of Fig.2.12a,

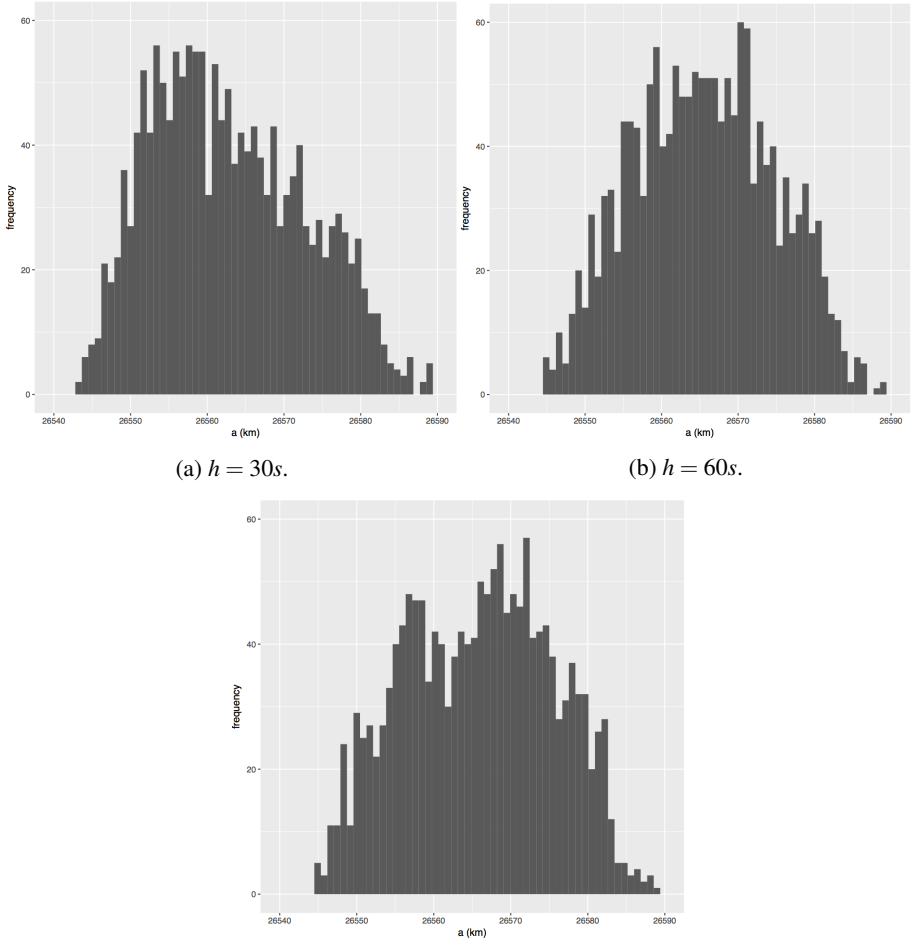

(a) $h = 30s$.

(b) $h = 60s$.

(c) $h = 100s$.

Figure 3.5 – Distributions of the semi-major axis for three chaotic trajectories of Fig. 3.1, calculated over 400 y. Simulations were performed with the ABM10 integrator.

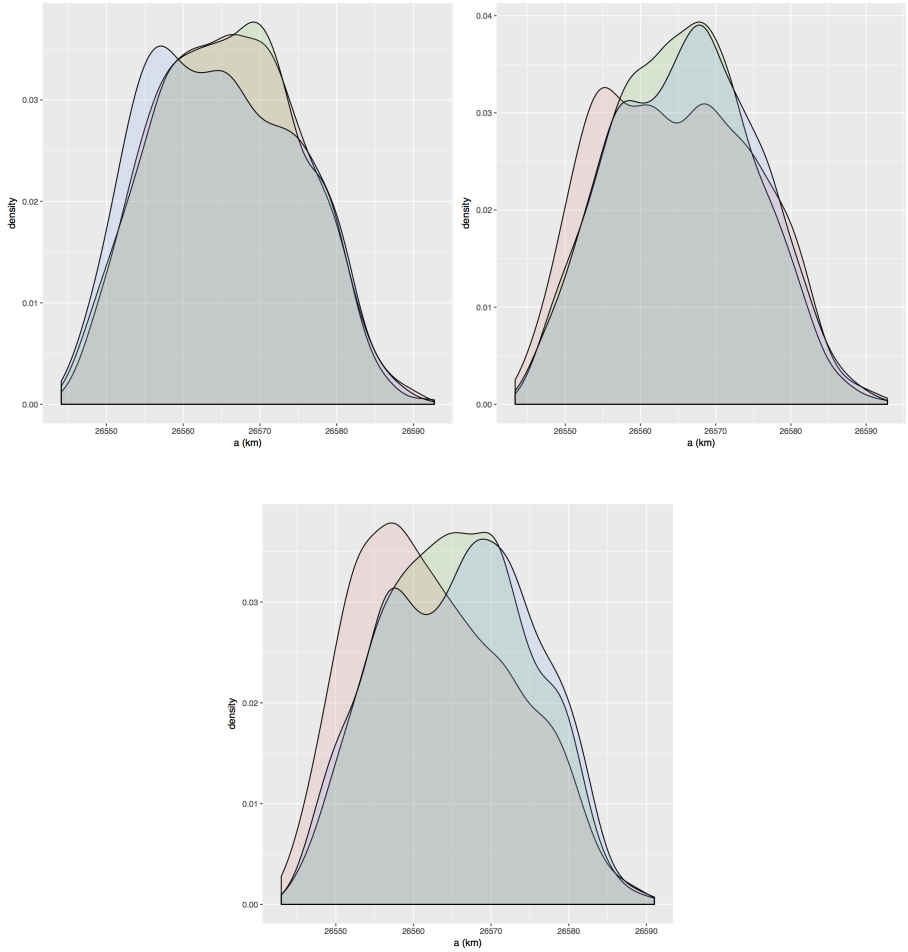

Figure 3.6 – Overlayed histograms as in Fig. 3.5 for three other sets of initial conditions: (a): $a = 26\ 572.4$ km, $e = 0.5$, $i = 23^\circ$, $\Omega = 270^\circ$, $\omega = 90^\circ$, $M = 336^\circ$; (b): $a = 26\ 572.4$ km, $e = 0.5$, $i = 23^\circ$, $\Omega = 270^\circ$, $\omega = 90^\circ$, $M = 338^\circ$; (c): $a = 26\ 572.4$ km, $e = 0.5$, $i = 23^\circ$, $\Omega = 270^\circ$, $\omega = 90^\circ$, $M = 340^\circ$. The J_2 and J_{22} harmonics of geopotential were considered.

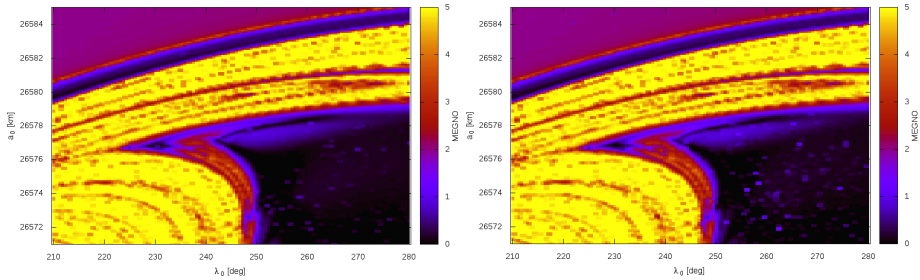

(a) $h = 30$ s. (b) $h = 100$ s.

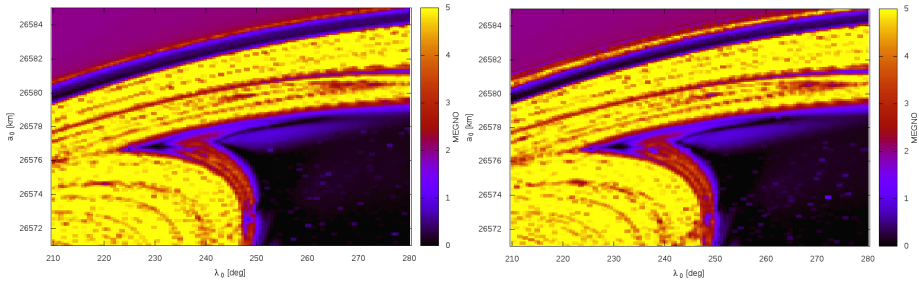

(c) $h = 30$ s. (d) $h = 60$ s.

Figure 3.7 – Comparison of zoomed portions of the boundary between chaotic and regular regions of the stability maps for 2:1 tesseral resonance (Fig. 2.4). (a) and (b) were traced with ABM10 integrator, whereas (c) and (d) with RK4. For each graph, 18 600 orbits were propagated over 40 y. The maps agree perfectly well for various time step entries.

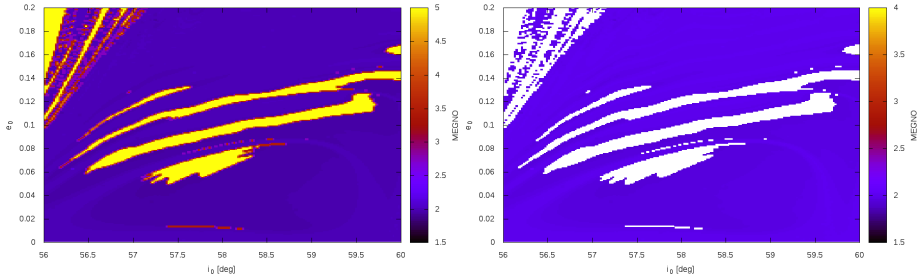

(a) MEGNO values. (b) Crash orbits.

Figure 3.8 – A zoomed in portion of Fig. 2.12a from previous chapter – MEGNO values (a) and orbits that eventually end up being collisional (b). Integration time was 200 y, 50 200 orbits were calculated.

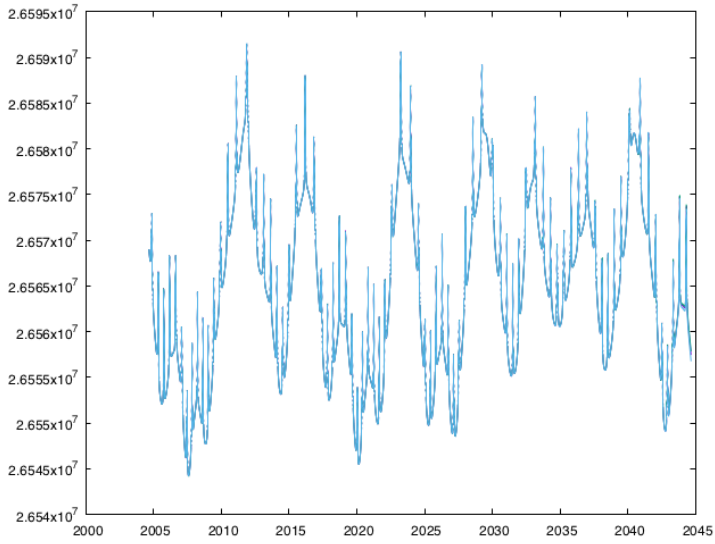

Figure 3.9 – A chaotic trajectory within the 2:1 tesseral sea traced with a symplectic scheme. No discrepancies between the trajectories obtained with various time steps were obtained. Initial conditions: $a = 26\,569$ km, $e = 0.5$, $i = 23°$, $\Omega = 270°$, $\omega = 90°$, $M = 230°$.

taken from Daquin et al. (2016). Whereas in the original map, there are both chaotic orbits and crash orbits, we obtain a much higher volume of crashing orbits – in fact, all initial conditions found to be chaotic end up having a perigee smaller than Earth's radius. It should be emphasized that while the original map was obtained with an averaged system, our rendition is, to our knowledge, the first time that a full system of osculating equations was propagated in case of lunisolar resonances. The change in integration time step does not influence this result. However, if we consider an estimated time of crash with the Earth's surface, we obtain a one day difference between the trajectories determined with 30 and 100 s of time step, which is still not much considering a long integration time (200 y).

As expected, no discrepancies depending on the time step are found when a symplectic scheme is used. We performed some tests with the use of SYMPLEC software, created by Ch. Hubaux (described in the Introduction). We used the SABA scheme of order 4, and the time steps of 0.01 day (864 seconds) and 0.001 day (86.4 seconds). Fig. 3.9 presents an exemplary trajectory with initial conditions in the tesseral chaotic sea. As visible, all trajectories, regardless of the time step that was used, coincide.

3.3 Conclusions

Performing numerical simulations of chaotic orbits in MEO region, whether within the tesseral or lunisolar resonances, with a constant time step method requires particular vigilance due to orbit dependance on a chosen time step. In fact, most of the

semi-major axis related quantities that we considered are not preserved and show that no information related to it can be trusted. Despite these discrepancies, the variational indicators are computed correctly, so the stability distinction is valid. It seems that some observables are more robust to numerical errors than others. These results suggest that some "good computational practices" should be defined and constrained. The symplectic scheme is the most reliable in this respect.

Chapter 4

Tumbling rotation of asteroids with YORP effect and energy dissipation

The YORP effect is based on a similar principle as the Yarkovsky effect, but affects the rotational motion of the body. The abbreviation was coined by Rubincam (2000) and honors the first scientists who, after Yarkovsky, proposed that the phenomenon may affect the body rotation (Radzievskii, 1952) and identified the thermal reemission and surface irregularities as the main factors (Paddack, 1969; Paddack and Rhee, 1975; O'Keefe, 1976). Since the work of Rubincam, various aspects of the YORP effect have been studied. The main application is the rotational dynamics of asteroids (although some initial studies in the domain of space debris have also emerged, see Albuja (2015)). However, most studies admit the simplifying assumption of principal axis rotation; few works investigated the mechanism in case of tumbling asteroids. Moreover, some of these results seem to be in contradiction with observational data, revealing flaws in present models. The process of dissipation of inelastic energy, mostly neglected so far, needs to be accounted for, as it might provide a remedy to the conundrum (initial work on this matter was done in Breiter and Murawiecka (2015)). In this last chapter, we provide an analytical model of the YORP effect on both principal axis and non-principal axis rotators, combined with inelastic energy dissipation, searching to identify the conditions for the principal axis rotation to act as an attractor. This time, the main bodies of interest are asteroids. We first introduce the reader to the YORP effect and nutation damping related to energy dissipation in Sections (4.1)-(4.4), before discussing the results in Sec. (4.5). The work was done in collaboration with Prof. S. Breiter.

4.1 YORP effect

The same mechanism of absorption and reemission of solar radiation as in Yarkovsky effect is at the basis of the YORP effect. However, the important difference between the two is the fact that the momentum of the reflected photons also contributes to secular changes in rotation (the absorption itself is still negligible (Rubincam, 2010)). Therefore, besides considering $\mathrm{d}\vec{f}_{ther}$ as expressed in Eq. (1.1.3), one also needs to take into account the related scattering part of the force, expressed as (assuming Lambert's law for scattering again)

$$\mathrm{d}\vec{f}_{sc} = -\frac{2}{3}\frac{A}{c}\max(0,\hat{n}\cdot\hat{r}_s)\,\Phi\,\hat{n}\,\mathrm{d}S. \tag{4.1.1}$$

The total force is then $\mathrm{d}\vec{f} = \mathrm{d}\vec{f}_{sc} + \mathrm{d}\vec{f}_{ther}$, and the YORP torque

$$\vec{M} = \int \vec{r}\times\mathrm{d}\vec{f}, \tag{4.1.2}$$

integrated over the whole body surface. The effect depends on the rotation direction and produces changes in rotation rate and obliquity of the angular momentum vector.

An important distinction of the YORP effect with respect to the Yarkovsky effect is the possibility to assume that the thermal conductivity K is null. This so-called *Rubincam's approximation* (Rubincam, 2000; Vokrouhlický and Čapek, 2002) means that there is no time lag between absorption and reemission of the thermal wave. It allows to drop the second member in the energy conservation equation (1.1.1) and calculate the temperature without the requirement to solve the heat diffusion problem, according to

$$T^4 = \frac{(1-A)\Phi}{\varepsilon\sigma}\max(0,\hat{n}\cdot\hat{r}_s). \tag{4.1.3}$$

The simplification is often used in YORP models. However, one needs to keep in mind that it is a rather strong assumption that may not be applicable in case of very small bodies, as they may have high values of thermal conductivity (they may even be isothermal if enough heat is conducted). What is more, it has been shown (Čapek and Vokrouhlický, 2004; Nesvorný and Vokrouhlický, 2008) that a non-zero K is important for the evolution of the obliquity, whereas the rotation rate is insensitive to it (as long as small surface features that can produce the so-called tangential YORP, TYORP, are ignored (Golubov and Krugly, 2012)).

The models with $K = 0$ are useful when applied to observational detection of the YORP effect, as the uncertainties in the determination of the asteroid pole position are already bigger then the estimates of the YORP effect in obliquity. The secular drift in rotation rate due to the YORP torque is very small and requires lengthy and precise observational campaigns.

The strong dependence of the effect on the shape of the body is also in contrast with the Yarkovsky force. As the reemission occurs in the direction normal to the surface, there is no torque in the limit of a spheroid; an object needs to have some 'windmill'-kind of asymmetry. A more detailed characterization of the shape will

usually diminish the error in YORP estimations. It has been shown that the effect is sensitive to small-scale surface features such as craters or boulders (Statler, 2009). What is more, such fine topography characteristics may require the treatment of heat diffusion problem in full three-dimensional form (Golubov et al., 2014; Ševeček et al., 2015). While this is computationally expensive, the consequences may be significant. Also, if the shape of an asteroid is not convex, the effects of shadowing must be considered, as the cut-off of the solar flux increases the temperature contrast on the surface.

The YORP effect is important for small bodies. Usually, $R \approx 10$ km is regarded as the limit on the size, above which the effect is negligible. The torque is proportional to the inverse of the radius square, therefore the smaller the object, the easier it is to detect it. It has been so far identified to affect the rotation rate of several asteroids, including 1862 Apollo (Kaasalainen et al., 2007), 54509 YORP (Lowry et al., 2007; Taylor et al., 2007), 3103 Eger (Ďurech et al., 2012), or 25143 Itokawa (Lowry et al., 2014), all of which are shorter than 2 km in their longest axes.

4.2 YORP on non-principal axis rotators

A vast majority of asteroids rotate around their principal axis. This means, as explained below, that their angular momentum is aligned with the axis of maximum inertia. A body on an orbit can experience various phenomenons that could potentially cause it to enter tumbling rotation: close encounters with planets, spin down by the YORP effect, or subcatastrophic impacts. Objects created in a disruption event of a parent body often exhibit tumbling rotation as well. The identified tumblers are mostly small and slowly rotating objects, relatively difficult to classify through photometry – numerous repeated observations are required in order to cover the long period (Pravec et al., 2014). Nevertheless, the observational data seem to suggest that the process of energy dissipation due to inelastic deformations in such bodies is efficient enough to overcome these triggers.

4.2.1 Non-principal axis rotation

The non-principal axis rotation is a state of excited rotational energy. If we define the axes of the body frame $\mathscr{B} = (\hat{b}_1, \hat{b}_2, \hat{b}_3)$ to be aligned with the principal axes of inertia tensor, it will have a form of a diagonal matrix

$$\mathbb{I} = \begin{pmatrix} I_1 & 0 & 0 \\ 0 & I_2 & 0 \\ 0 & 0 & I_3 \end{pmatrix}, \quad \text{with} \quad I_1 \leq I_2 \leq I_3. \tag{4.2.1}$$

We will further use the moments of inertia inverses $a_i = 1/I_i$.

The angular momentum vector is defined as $\vec{G} = \mathbb{I}\vec{\Omega}$. In a non-perturbed case, its modulus $||\vec{G}|| = G$ is a first integral, so the tip of $\vec{G}$ describes a sphere as $G^2 =$

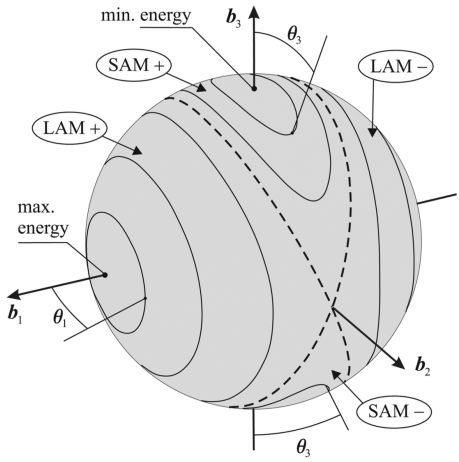

Figure 4.1 – Trajectories of the angular momentum vector in the body reference frame. Separatrix is marked with a dashed line. From Breiter and Murawiecka (2015).

$G_1^2 + G_2^2 + G_3^2$. The second first integral is the kinetic energy of the system,

$$\mathscr{H} = \frac{1}{2}\,\vec{\Omega}\cdot\vec{G} = \frac{1}{2}\,(a_1\,G_1^2 + a_2\,G_2^2 + a_3\,G_3^2), \tag{4.2.2}$$

defining the surface of an ellipsoid. The trajectories of $\vec{G}$ in the body frame are defined as level contours of constant energy surface on the angular momentum sphere (Fig. 4.1). In case of principal axis rotation, the angular momentum vector is aligned with one of the body principal axes as well as the angular velocity vector $\vec{\Omega}$:

$$\vec{G} = I_3\,\vec{\Omega}, \quad \text{or} \quad \vec{G} = I_1\,\vec{\Omega}. \tag{4.2.3}$$

Otherwise, its components G_i evolve in the body frame according to (in an unperturbed problem)

$$\dot{G}_1 = -(a_2 - a_3)G_2G_3, \tag{4.2.4}$$
$$\dot{G}_2 = \quad (a_1 - a_3)G_1G_3, \tag{4.2.5}$$
$$\dot{G}_3 = -(a_1 - a_2)G_1G_2, \tag{4.2.6}$$

and the solution is expressed in terms of elliptic functions. $\vec{G}$ circulates around $\pm\hat{b}_1$ or $\pm\hat{b}_3$, and the two regimes are divided by a separatrix, marked in Fig. 4.1 with a dashed curve.

If the angular momentum vector is aligned with one of the principal axes, the system is in an equilibrium. Six equilibria points can be identified, two for each axis. Those related to the shortest axis $\hat{b}_3$ or the longest one $\hat{b}_1$ are stable and correspond to the minimum or maximum energy state, respectively, whereas the intermediary axis

$\hat{b}_2$ is associated with an unstable equilibrium. The energy on the axes is $\mathscr{H} = \frac{1}{2} a_i G^2$. In case of a non-principal axis rotation, its value is constrained by those limits

$$0 < \frac{1}{2} a_3 G^2 \leq \mathscr{H} \leq \frac{1}{2} a_1 G^2. \tag{4.2.7}$$

Introducing $\mathscr{A} = 2\mathscr{H}/G^2$, this reads

$$0 < a_3 \leq \mathscr{A} \leq a_1 \tag{4.2.8}$$

(Deprit and Elipe, 1993), and we can differentiate between two regimes of motion:

- $a_1 > \mathscr{A} > a_2 > a_3$ – so-called *long-axis mode*, LAM, where the angular momentum vector circulates around the longest axis $\hat{b}_1$;
- $a_1 > a_2 > \mathscr{A} > a_3$ – *short-axis mode*, SAM, where $\vec{G}$ circulates around the shortest axis $\hat{b}_3$.

One can discriminate between SAM+ and SAM– depending on the sign of the product $\vec{G} \cdot \hat{b}_3$; the same applies to LAM (see Fig. 4.1). In case of $\mathscr{A} = a_2$, the trajectory of $\vec{G}$ coincides with the unstable equilibrium corresponding to $\hat{b}_2$ axis, or with the separatrix. In the presence of perturbations, chaotic region arises in its vicinity, and the motion is unpredictable.

The position of the angular momentum vector in the body frame is described by its angle with the given body axis. Further, we will use

$$\theta_{\mathrm{s}} = \max(\arccos|\hat{G} \cdot \hat{b}_s|), \tag{4.2.9}$$

with the subscript s=1 in case of LAM and 3 for SAM (see Fig. 4.1). It is related to the variable $\mathscr{A}$ through

$$\mathscr{A} = a_2 - (a_2 - a_s)\cos^2\theta_{\mathrm{s}} \tag{4.2.10}$$

(Breiter et al., 2012).

4.2.2 YORP on tumbling objects

The YORP effect has the tendency to sustain tumbling. This fact exposes the need for a more general model that would not suffer from the limiting assumption of principal axis (hereinafter abbr. PA) rotation. The first step in this direction was made by Vokrouhlický et al. (2007) and was entirely numerical. They found the existence of asymptotic tumbling states with an infinite growth of the angular momentum, locked around the obliquities of 55°or 125°. The first semi-analytical model was developed by Cicalò and Scheeres (2010), where the perturbation was averaged over precession and nutation cycles. Within the first-order approximation of the illumination function, they found first integrals of motion and closed cycles around equilibria where Vokrouhlický et al. (2007) found their asymptotic states. The angular momentum in their solution remains bounded. Both of these results were confirmed by the semi-analytical theory of Breiter et al. (2011), based on a more accurate description of the

illumination function. We here proceed to shortly describe this model as it is the one that we further use.

The model assumes zero thermal conductivity. The YORP torque in the body frame is described as

$$\vec{M} = -\kappa \left(\frac{a}{r_\mathrm{s}}\right)^2 \sum_{n\geqslant 1} \sum_{m=-n}^{n} \vec{v}_{n,m} Y_{n,m}(\hat{r}_\mathrm{s}), \tag{4.2.11}$$

where r_s is the length of the Sun position vector and $\hat{r}_\mathrm{s}$ its unit vector. $Y_{n,m}$ are spherical harmonics of degree n and order m, and $\vec{v}_{n,m}$ are dimensionless complex vector coefficients depending on the distribution of the optical and thermal recoil force on the body surface. The physical constants are encapsulated in

$$\kappa = \frac{2}{3}\frac{V\Phi_0}{c}\left(\frac{d_0}{a}\right)^2, \tag{4.2.12}$$

with V the body volume and Φ_0 the solar flux at $d_0 = 1$ AU. The torque is then averaged over the orbital and rotational motion. The resulting equations of motion are

$$\dot{G}_\mathrm{s} = -\frac{\kappa}{1-e^2}\frac{\pi}{2\mathrm{K}_\mathrm{s}} \sum_{n=1} \Theta^0_{2n}(\cos\varepsilon) G_{\mathrm{s},n}, \tag{4.2.13}$$

$$\dot{\varepsilon}_\mathrm{s} = -\frac{\kappa}{(1-e^2)\,G}\frac{\pi}{2\mathrm{K}_\mathrm{s}} \sum_{n=1} \Theta^1_{2n}(\cos\varepsilon) E_{\mathrm{s},n}, \tag{4.2.14}$$

$$\dot{\Delta}_\mathrm{s} = -\frac{\kappa\Delta}{(1-e^2)\,G}\frac{\pi}{\mathrm{K}_\mathrm{s}} \sum_{n=1} \Theta^0_{2n}(\cos\varepsilon) \Delta_{\mathrm{s},n}, \tag{4.2.15}$$

depending on the rotation mode (hence the subscript s). $\mathrm{K}_\mathrm{s} = \mathrm{K}(k_\mathrm{s})$ is the complete elliptic integral of the first kind, and its modulus k_s depends on θ_s and a_i. Θ^m_{2n} are normalized associated Legendre functions (of degree $2n$ and order m). The full expressions of the functions $G_{\mathrm{s},n}, E_{\mathrm{s},n}, \Delta_{\mathrm{s},n}$ are quite extensive and can be found in Breiter et al. (2011); they depend on θ_s and a_i. The variable $\Delta = 1/\mathscr{A}$ is called dynamical inertia and is often used in rigid body problems.

The averaging assumptions exclude long rotation periods (comparable to orbital period) as well as motion in the vicinity of separatrix, where the chaotic zone arises.

Simulations performed by Breiter et al. (2011) confirmed the asymptotic states in ε and θ_s with the growth or decrease of the rotation rate. They also corroborated the presence of first integrals found by Cicalò and Scheeres (2010) in case of quadrupole approximation of the illumination function, and additionally identified some limit cycles in $(\varepsilon, \theta_\mathrm{s})$ space in the LAM (Fig. 4.2). In a general rotation case, the principal axis rotation seems to be unstable under the YORP effect. Being in contradiction with observational evidence, those states should not persist in reality as the process of energy dissipation should drive the angular momentum vector back to the shortest body axis.

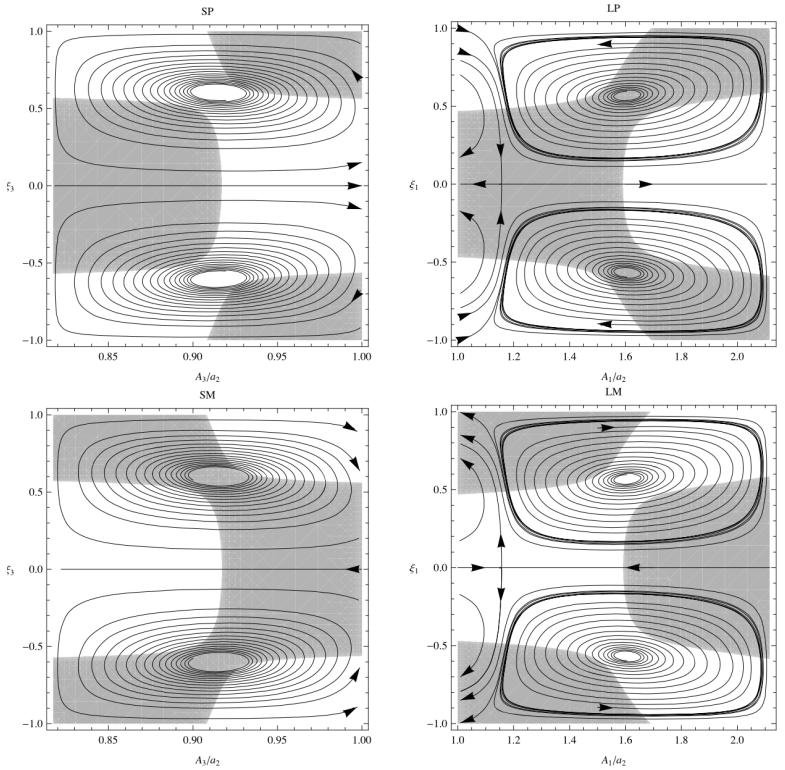

Figure 4.2 – Evolution of the instantaneous rotation axis for an exemplary shape of 3103 Eger, a 1.5 km-sized asteroid for which the YORP effect was measured (Ďurech et al., 2012). The trajectories are displayed in the $(\xi, \mathscr{A}_s/a_2)$ space, with $\xi = \cos\varepsilon$ and $\mathscr{A}_s/a_2 = 1 - \frac{a_2 - a_s}{a_2}\cos^2\theta_s$. The grey and white colors mark the areas of decrease and growth of G, respectively. The value of $\mathscr{A}_s/a_2 = 1$ corresponds to the separatrix. For principal axis rotation, $\mathscr{A}_s/a_2$ depends on axes ratios and is equal to 0.8173 for $\hat{b}_3$ and 2.1154 for $\hat{b}_1$ for Eger. SAM+ and SAM– modes are labeled as SP and SM, respectively, and likewise for LAM+ and LAM–. The limit cycles are visible in both LAM planes; stable in LAM+ and unstable in LAM–. The trajectories that originate inside them remain in LAM. The loss of angular momentum causes the chaotic zone around the separatrix to expand and eventually disrupt the asymptotic cycles and points. From Breiter et al. (2011).

4.3 Nutation damping

The circulation of $\vec{G}$ around $\hat{b}_1$ or $\hat{b}_3$ in NPA rotation means that there is a centrifugal force that results in internal stresses and displacements that are inelastic. This phenomenon leads to the dissipation of energy in form of heat. The draining of kinetic energy damps the instantaneous axis of rotation to the principal axis of maximum inertia, which is the minimum energy state.

The calculation of the effect is rather challenging. Most models approximate the

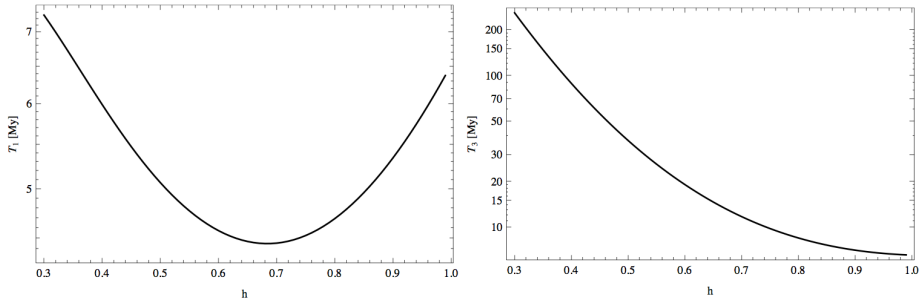

(a) LAM (b) SAM

Figure 4.3 – Dependence of nutation excitation (a) and damping (b) times on body shape for exemplary ellipsoids with $h = h_1 = h_2$. From Breiter et al. (2012).

body shape as a spheroid. Two exceptions are the rectangular prism in the model of Efroimsky (2000) and a triaxial ellipsoid of Breiter et al. (2012), but the latter is better suited for the application to asteroids.

Within this model, the rate of energy loss is

$$\dot{E} = -\frac{a_e^4 \rho\, m G^5 a_\mathrm{s}^5}{\mu\, Q}\, \Psi_\mathrm{s} \tag{4.3.1}$$

(Breiter et al., 2012), which translates into the change in θ_s as

$$\frac{\mathrm{d}\theta_\mathrm{s}}{\mathrm{d}t} = \frac{a_e^4 V G^3 a_\mathrm{s}^5}{\mu Q\,(a_\mathrm{s} - a_2)}\, \frac{\Psi_\mathrm{s}}{\sin\theta_\mathrm{s} \cos\theta_\mathrm{s}}. \tag{4.3.2}$$

The function Ψ_s depends on the current θ_s value and on the principal moments of inertia of the reference ellipsoid through the ratios of the ellipsoid semi-axes a_e, b_e, c_e

$$h_1 = \frac{b_e}{a_e}, \quad h_2 = \frac{c_e}{b_e}, \quad c_e \le b_e \le a_e. \tag{4.3.3}$$

ν and μ are respectively the Poisson ratio and Lamé modulus – quantities describing the stiffness and compressibility of the material, and Q is its quality factor. Their values are further assumed to be $\nu = 0.25$, $\mu = 10^9$ Pa (pascals), $Q = 100$.

From (4.3.1), one can see that the dissipation is faster for quickly rotating objects. Bigger bodies also experience stronger effect and reach the principal axis rotation faster.

If the body starts its evolution in LAM, θ_1 grows and the angular momentum vector is pushed towards the separatrix. In SAM, θ_3 decreases and $\vec{G}$ is driven towards the principal axis $\hat{b}_3$, where it should remain in an unperturbed case. The evolution in SAM is much longer than that in LAM (Fig. 4.3, plotted for $h = h_1 = h_2$).

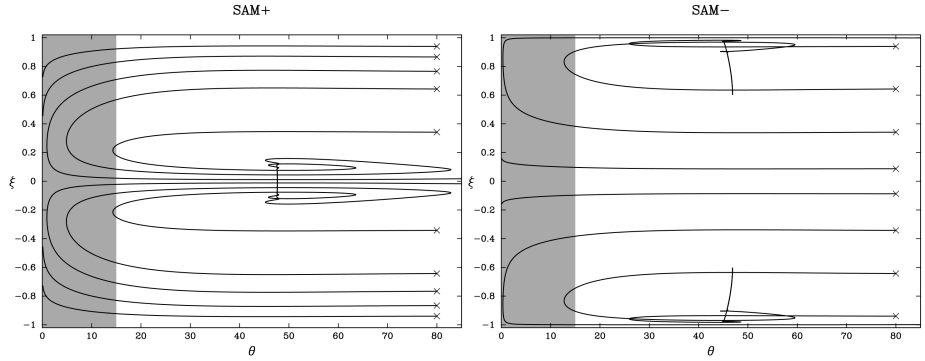

Figure 4.4 – Evolution of Eger rotation in SAM as in Fig. 4.2, but including the effects of energy dissipation, in (ξ, θ_3) plane. From Breiter and Murawiecka (2015).

4.4 YORP torque and inelastic energy dissipation

The first (and so far only) work that considered the joint action of the YORP effect and energy dissipation was that of Breiter and Murawiecka (2015). The fully numerical study consisted of integrating the equations for $\dot{G}_\mathrm{s}$, $\dot{\varepsilon}_\mathrm{s}$, $\dot{\theta}_\mathrm{s}$ for some exemplary shapes of asteroids. As the energy dissipation affects only the nutation angle, equations for $\dot{G}_\mathrm{s}$ and $\dot{\varepsilon}_\mathrm{s}$ remain the same as in (4.2.13) and (4.2.14), respectively, whereas the one for $\dot{\theta}_\mathrm{s}$ becomes

$$\dot{\theta}_\mathrm{s} = \frac{a^4 \rho\, m G^3 a_\mathrm{s}^5}{\mu Q (a_\mathrm{s} - a_2)} \frac{\Psi_\mathrm{s}}{\sin\theta_\mathrm{s} \cos\theta_\mathrm{s}} + \frac{\kappa\pi}{2G\mathrm{K}\sqrt{1-e^2}} \frac{a_2 - (a_2 - a_\mathrm{s})\cos^2\theta_\mathrm{s}}{(a_2 - a_\mathrm{s})\sin\theta_\mathrm{s}\cos\theta_\mathrm{s}} \sum_{n\geq 1} \Theta^0_{2n}(\cos\varepsilon)\Delta_{\mathrm{s},n}. \tag{4.4.1}$$

Nevertheless, the variations in θ_s affect the evolution of rotation rate and obliquity through the dependence of equations (4.2.13) and (4.2.14) on nutation. Generally speaking, the results showed that the pure YORP cycles from Breiter et al. (2011) are destroyed under the action of nutation damping related to energy dissipation, though some new asymptotic states of stationary tumbling were detected. The number of initial conditions that are driven towards the principal axis is too small compared to observational data. We briefly describe the details of these results below.

Fig. 4.4 is an analogue of Fig. 4.2a and b, but with nutation damping. The shape of 3103 Eger was chosen as an example in order to allow for comparison with the results of Breiter et al. (2011). The main effect of energy dissipation is to push the trajectories to the principal axis on the left, therefore any migration in ξ or to the right of the plot is due to YORP only. The integration was limited to $0.1^\circ < \theta_\mathrm{s} < 85^\circ$ in order to stay away from the chaotic zone around the separatrix (the upper limit) and to avoid a singularity in (4.4.1) at $\theta_\mathrm{s} = 0^\circ$($\theta_\mathrm{s} < 0.1^\circ$is therefore considered as principal axis rotation). The grey area marks the region of $\theta_3 < 15\ ^\circ$that is observationally indistinguishable from the principal axis rotation (Henych and Pravec, 2013). Stable points

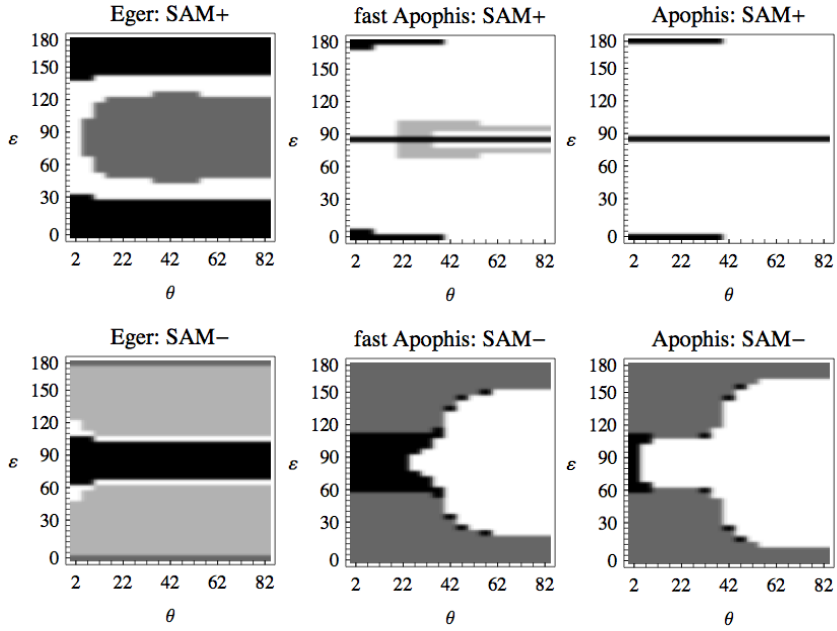

Figure 4.5 – Maps of final states for three exemplary objects. Color code: white – separatrix zone; light grey – rotational period below 10 y; dark grey – stationary tumbling with fixed period; black– principal axis rotation. Initial conditions were sampled with a 5°step in $\theta_3 \in (2^\circ, 82^\circ)$ and $\varepsilon \in (0^\circ, 180^\circ)$. Initial rotation periods were 5.7 h for Eger, 3 h for "fast Apophis" and 30 h for Apophis. From Breiter and Murawiecka (2015).

visible in Fig. 4.2a, b are gone, but a new asymptotic state is identified – stationary tumbling with a fixed rotation rate and obliquity $\varepsilon = 90^\circ$. Other than that, the trajectories are either driven towards the principal axis (for $|\xi| \gtrsim 0.8$ in SAM+ and $|\xi| \lesssim 0.5$ in SAM–), hit the separatrix in SAM+ or are driven towards the former unstable points (see Fig. 4.2b) and then towards $\xi = 0$ in SAM–, though they lose so much angular momentum that the rotation period becomes too long. All the orbits in both LAM cases are driven towards the separatrix; the limit cycles and equilibrium points do not persist. This is due to the fact that the dissipation effects are much stronger in LAM than in SAM. Smaller bodies were considered as well and more YORP-like evolution was detected, as the energy dissipation is much weaker. The trajectories do not remain in the stable points as they are related to angular momentum growth, which increases the dissipation. The stable cycles are also destroyed.

In general, there are four final states that are possible: exit from a mode through the separatrix, unlimited angular momentum growth (to the point where it violates the assumptions of the model), drive towards the principal axis and stationary tumbling state with stable period. Fig. 4.5 presents the distribution of these outcomes on a $(5^\circ \times 5^\circ)$ grid of initial conditions for three different objects: 3103 Eger as earlier, a much smaller 99942 Apophis (as an example of a body that is actually a tumbling

asteroid (Pravec et al., 2014)) and "fast Apophis" with a rotational period 10 times shorter than the actual one (as an instance of a smaller body, like Apophis, but with a faster rotation rate). Although there is no contradiction with the observational data for Eger ($\theta_3 < 15°$and $\varepsilon \approx 175°$in SAM+), the percentage of initial conditions resulting in principal axis rotation is too small for the spin rate-size ratio of an Eger-like object; most of the initial conditions remain in the tumbling zone. Smaller bodies like Apophis experience a stronger YORP effect and weaker nutation damping, so the four graphs represent this trend very well. Especially in SAM–, many stationary tumbling states were observed. Again, this is in accordance with the currently observed rotational state of 99942 Apophis. There are more trajectories ending up on the principal axis in case of faster Apophis since the energy dissipation is stronger for higher rotation rates, whereas YORP effect in θ_s is weaker. However, all things considered, the ratio of this end state to those of sustained tumbling is still too low when compared with observations (Pravec et al., 2014). Either the energy dissipation is underestimated, either the YORP effect overestimated, or – both. Some simplifying assumptions could also be to blame, e.g. the zero thermal conductivity, or the convex shape approximation.

4.5 Stability of the principal axis rotation

So far, we summarized the general understanding of the processes related to tumbling rotation of asteroids when both the YORP effect and the nutation damping due to energy dissipation are present. Here, we proceed to describe the new, analytical approach and results that were developed in the course of this thesis. As it was shown, the discussion presented so far raises the question of the stability of motion in close vicinity to the principal axis. Below, we first develop an approximated model for YORP effect on the principal axis rotators and then proceed to consider small departures from $\theta_3 = 0$.

4.5.1 Principal axis YORP

In the principal axis rotation, the variables $\Omega = G/I_3$ and $\xi = \cos\varepsilon$ evolve due to the YORP effect according to

$$\dot{\Omega} = -\kappa^* \sum_{n\geqslant 1} P_{2n}(0)\, P^0_{2n}(\xi)\, Z_{2n,0}, \tag{4.5.1}$$

$$\dot{\xi} = -\frac{\kappa^* \sqrt{1-\xi^2}}{\Omega} \sum_{n\geqslant 1} P_{2n}(0)\, P^1_{2n}(\xi)\, \left(X_{2n,1} - Y_{2n,1}\right), \tag{4.5.2}$$

with

$$\kappa^* = \frac{\kappa}{I_3\sqrt{1-e^2}}, \tag{4.5.3}$$

and P_n an unnormalized Legendre polynomial. The unnormalized values of the torque coeffcients are related to the real and imaginary parts of $\vec{v}_{n,m}$ through

$$X_{n,m} = \sigma_{n,m}\, \Re(\vec{v}_{n,m}) \cdot \hat{b}_1, \quad Y_{n,m} = \sigma_{n,m}\, \Im(\vec{v}_{n,m}) \cdot \hat{b}_2,$$

$$Z_{n,m} = \sigma_{n,m}\,\Re(\vec{v}_{n,m})\cdot\hat{b}_3, \tag{4.5.4}$$

with

$$\sigma_{n,m} = \sqrt{\frac{(2n+1)(n-m)!}{4\pi\,(n+m)!}}. \tag{4.5.5}$$

The system in the first approximation with $n = 1$ (the quadrupole approximation) has the form

$$\dot{\Omega} = -\kappa^* P_2(0)\,P_2^0(\xi)\,Z_{2,0}, \tag{4.5.6}$$

$$\dot{\xi} = -\frac{\kappa^*\sqrt{1-\xi^2}}{\Omega} P_2(0)\,P_2^1(\xi)\,(X_{2,1}-Y_{2,1})\,. \tag{4.5.7}$$

Dividing $\dot{\Omega}$ by $\dot{\xi}$, we have

$$\frac{\mathrm{d}\Omega}{\mathrm{d}\xi} = \frac{\Omega\,P_2^0(\xi)\,Z_{2,0}}{\sqrt{1-\xi^2}\,P_2^1(\xi)\,(X_{2,1}-Y_{2,1})}, \tag{4.5.8}$$

where the variables can be separated. After rearrangements, we obtain

$$\frac{\mathrm{d}\Omega}{\Omega} = \frac{1-3\xi^2}{\xi\,(1-\xi^2)}\,\frac{\mathrm{d}\xi}{2\zeta}, \tag{4.5.9}$$

where

$$\zeta = 3\left(\frac{X_{2,1}-Y_{2,1}}{Z_{2,0}}\right), \tag{4.5.10}$$

equal to 1 in case of convex bodies within Rubincam's approximation. Considering that the values $\xi = 0$ and $\xi^2 = 1$ are stationary points of the equation for $\dot{\xi}$ and therefore $\xi = 0$ cannot be crossed, the first integral is therefore found to be

$$C\Omega = \sqrt{|\xi|(1-\xi^2)}. \tag{4.5.11}$$

The sign of C is fixed to $C > 0$, or $C = 0$ for initial conditions $\xi = 0$ or $\xi^2 = 1$ with $\Omega > 0$; in such case, Ω varies at a constant obliquity.

With this integral, Ω can be eliminated from (4.5.7), giving

$$\frac{\mathrm{d}\xi}{\mathrm{d}t} = -\sqrt{2}Cw\sqrt{|\xi|\,(1-\xi^2)}, \tag{4.5.12}$$

where

$$w = \frac{3\,\kappa^*}{2\sqrt{2}}\,(X_{2,1}-Y_{2,1})\,. \tag{4.5.13}$$

The solution for ξ is then found in terms of Jacobi elliptic cosine:

$$\xi(t) = \pm\mathrm{cn}^2\left(u, \tfrac{1}{\sqrt{2}}\right), \tag{4.5.14}$$

where

$$u = Cwt + \varphi. \tag{4.5.15}$$

φ is the initial argument, given by

$$\xi(0) = \pm \mathrm{cn}^2\left(\varphi, \tfrac{1}{\sqrt{2}}\right), \text{ or } \varphi = F\left(\arccos\sqrt{|\xi(0)|}, \tfrac{1}{\sqrt{2}}\right). \tag{4.5.16}$$

Since $\xi = 0$ cannot be crossed, the sign $\sigma_\xi = \mathrm{sgn}(\xi)$, remains the same during the evolution. Therefore, the choice in (4.5.14) should be the same as the sign of initial $\xi(0)$.

Knowing $\xi(t)$, we find $\Omega(t)$ with the use of the first integral C to be

$$\Omega(t) = \frac{\sqrt{2}}{C}\,\mathrm{sn}\left(u, \tfrac{1}{\sqrt{2}}\right)\,\mathrm{cn}\left(u, \tfrac{1}{\sqrt{2}}\right)\,\mathrm{dn}\left(u, \tfrac{1}{\sqrt{2}}\right). \tag{4.5.17}$$

Although these two solutions seem to be periodic, they are not as the propagation should end at the limits of $\xi^2(t) = 0$ and $\xi^2(t) = 1$.

Adding further terms in the insolation expansion can be seen as perturbing the quadrupole system. We thus have

$$\dot{\Omega} = -\kappa^* P_2(0)\, P_2^0(\xi)\, Z_{2,0} + F_\Omega, \tag{4.5.18}$$

$$\dot{\xi} = -\frac{\kappa^*\sqrt{1-\xi^2}}{\Omega} P_2(0)\, P_2^1(\xi)\,\frac{1}{3}\, Z_{2,0} + F_\xi, \tag{4.5.19}$$

with F_Ω and F_ξ the perturbations to (4.5.6, 4.5.7). This system can be solved with the variation of constants approach, in which C and φ become functions of time in the unchanged solutions (4.5.14, 4.5.17). Then, the first order solution will be

$$C(t) = C_0 + \epsilon\, C_1(t), \tag{4.5.20}$$

$$\varphi(t) = \varphi_0 + \epsilon\, \varphi_1(t). \tag{4.5.21}$$

The new $u(t)$ is found using

$$u = w\int_0^t C\mathrm{d}t' + \varphi, \tag{4.5.22}$$

in place of (4.5.15), in order to avoid an explicit presence of time in the equation of motion. The meaning of $\varphi = u(0)$ is preserved, but this definition is better suited when C is variable. Therefore, we have

$$u(t) = wC_0 t + \varphi_0 + \epsilon\left(w\int_0^t C_1(t')\mathrm{d}t' + \varphi_1(t)\right) = u_0(t) + \epsilon\, u_1(t). \tag{4.5.23}$$

For linear perturbations, we have

$$\dot{C}_0 = 0, \quad \dot{\varphi}_0 = 0, \quad \dot{u}_0 = wC_0, \tag{4.5.24}$$

and

$$\dot{C}_1 = -\frac{C_0}{\Omega_0} F_\Omega(\xi_0) - \sigma_\xi \frac{P_2(\xi_0)}{C_0\Omega_0^2} F_\xi(\Omega_0, \xi_0), \tag{4.5.25}$$

$$\dot{\varphi}_1 = -\frac{\sigma_\xi F_\xi(\Omega_0, \xi_0)}{\sqrt{2} C_0 \Omega_0}. \tag{4.5.26}$$

The perturbed system with the terms of $n = 2$ and $n = 3$ is

$$F_\Omega = -\frac{3\kappa^* Z_{4,0}}{8} P_4^0(\xi) + \frac{5\kappa^* Z_{6,0}}{16} P_6^0(\xi), \tag{4.5.27}$$

$$F_\xi = -\frac{\kappa^* \sqrt{1-\xi^2}}{\Omega} \left(\frac{3(X_{4,1} - Y_{4,1})}{8} P_4^1(\xi) - \frac{5(X_{6,1} - Y_{6,1})}{16} P_6^1(\xi) \right). \tag{4.5.28}$$

Integration of equations (4.5.25, 4.5.26) yields

$$C_1(t) = \frac{C_0 \kappa^*}{\sqrt{2} w} (\left(\ln\left(1 - \xi_0^2(t)\right) - \ln\left(1 - (\xi_0^2(0))\right) \right) A_1 + \left(\ln(|\xi_0(t)|) - \ln(|\xi_0(0)|) \right) A_2 + \left(\xi_0^2(t) - \xi_0^2(0) \right) A_3 + \left(\xi_0^4(t) - \xi_0^4(0) \right) A_4), \tag{4.5.29}$$

$$\varphi_1(t) = \frac{5\kappa^* C_0}{2w} \left(\sqrt{2} A_5 w t + (\Omega_0(t) - \Omega_0(0)) A_6 + \left(\xi_0^2(t)\Omega_0(t) - \xi_0^2(0)\Omega_0(0) \right) A_7 \right), \tag{4.5.30}$$

with coefficients

$$A_1 = \frac{1}{32} \left(-60(X_{4,1} - Y_{4,1}) + 105(X_{6,1} - Y_{6,1}) + 6Z_{4,0} - 5Z_{6,0} \right), \tag{4.5.31}$$

$$A_2 = \frac{1}{256} \left(360(X_{4,1} - Y_{4,1}) + 525(X_{6,1} - Y_{6,1}) - 36Z_{4,0} - 25Z_{6,0} \right), \tag{4.5.32}$$

$$A_3 = \frac{105}{128} \left(-6(X_{4,1} - Y_{4,1}) - 6(X_{6,1} - Y_{6,1}) + Z_{4,0} + Z_{6,0} \right), \tag{4.5.33}$$

$$A_4 = \frac{1155}{1024} \left(9(X_{6,1} - Y_{6,1}) - Z_{6,0} \right), \tag{4.5.34}$$

$$A_5 = \frac{1}{8} \left((X_{4,1} - Y_{4,1}) + \frac{15}{4} (X_{6,1} - Y_{6,1}) \right), \tag{4.5.35}$$

$$A_6 = \frac{1}{8} \left(-7(X_{4,1} - Y_{4,1}) - \frac{45}{8} (X_{6,1} - Y_{6,1}) \right), \tag{4.5.36}$$

$$A_7 = \frac{99}{64} (X_{6,1} - Y_{6,1}). \tag{4.5.37}$$

Fig. 4.6 compares this analytical solution for $C(t)$ and $\varphi(t)$ with the results of numerical integration of equations (4.5.1, 4.5.2) with $n = 3$.

Calculation of $u(t)$ is not straightforward as it requires integrating C_1, which involves logarithms. Their integrals produce hypergeometric functions

$$\int \ln\left(1 - \xi_0^2(t)\right) dt = -\frac{\Omega_0(t)}{\sqrt{2|\xi_0(t)|} w} \left(2{}_3\mathrm{F}_2 \left(\frac{1}{2}, \frac{1}{2}, \frac{3}{4}; \frac{3}{2}, \frac{3}{2}; 1 - \xi_0^2(t) \right) - {}_2\mathrm{F}_1 \left(\frac{1}{2}, \frac{3}{4}; \frac{3}{2}; 1 - \xi_0^2(t) \right) \ln(1 - \xi_0^2(t)) \right), \tag{4.5.38}$$

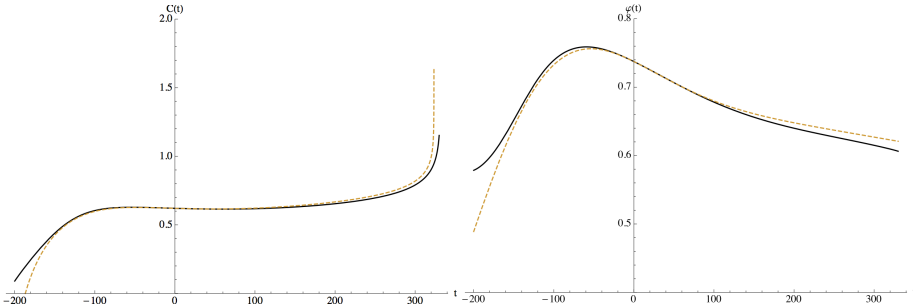

Figure 4.6 – Trajectories obtained with analytical solution (dashed line) of $C(t)$ and $\phi(t)$ as compared with numerical integration results (solid line). Plotted with $\kappa^* = 1$, $\Omega_0 = 1$, $\xi_0 = \frac{1}{\sqrt{3}}$.

$$\int \ln\left(|\xi_0(t)|\right) dt = \frac{2\sqrt{2\,|\xi_0(t)|}}{C_0\, w}\left({}_3\mathrm{F}_2\left(\frac{1}{4},\frac{1}{4},\frac{1}{2};\frac{5}{4},\frac{5}{4};\xi_0^2(t)\right)\right.$$
$$\left.-{}_2\mathrm{F}_1\left(\frac{1}{4},\frac{1}{2};\frac{5}{4};\xi_0^2(t)\right)\ln\left(\sqrt{|\xi_0(t)|}\right)\right). \tag{4.5.39}$$

The ${}_2\mathrm{F}_1\left(\frac{1}{4},\frac{1}{2};\frac{5}{4};x^2\right)$ function can be identified with the elliptic integral of the first kind $\frac{1}{2}\sqrt{\frac{2}{x}}\,\mathrm{F}\left(\arccos\left(\sqrt{\frac{1-x}{1+x}}\right)\right)$, whereas ${}_2\mathrm{F}_1\left(\frac{1}{2},\frac{3}{4};\frac{3}{2};x\right)$ with $\sqrt{\frac{2}{x}}\,\mathrm{F}\left(\arcsin\left(\sqrt{1-\sqrt{1-x}}\right)\right)$, which in our case simplifies to

$$\frac{\sqrt{2|\xi_0(t)|}}{\Omega_0(t)\,C_0}\mathrm{F}\left(\mathrm{am}(u_0)\right) = \frac{\sqrt{2|\xi_0(t)|}}{\Omega_0(t)\,C_0}u_0. \tag{4.5.40}$$

To calculate the two ${}_3\mathrm{F}_2$ functions, their hypergeometric series,

$${}_3\mathrm{F}_2\left(\frac{1}{2},\frac{1}{2},\frac{3}{4};\frac{3}{2},\frac{3}{2};1-\xi_0^2(t)\right) = \sum_{i=0}^{\infty}\frac{\left(\left(\frac{1}{2}\right)_i\right)^2\left(\frac{3}{4}\right)_i}{\left(\left(\frac{3}{2}\right)_i\right)^2}\frac{\left(1-\xi_0^2(t)\right)^i}{i!}, \tag{4.5.41}$$

$${}_3\mathrm{F}_2\left(\frac{1}{4},\frac{1}{4},\frac{1}{2};\frac{5}{4},\frac{5}{4};\xi_0^2(t)\right) = \sum_{i=0}^{\infty}\frac{\left(\left(\frac{1}{4}\right)_i\right)^2\left(\frac{1}{2}\right)_i}{\left(\left(\frac{5}{4}\right)_i\right)^2}\frac{\xi_0^{2i}(t)}{i!}, \tag{4.5.42}$$

can be used. Eventually, the new $u(t)$ is

$$u(t) = u_0 + \frac{\kappa^*}{w}\left(2A_2\left(\sqrt{|\xi_0(t)|}\,{}_3\mathrm{F}_2(\xi_0^2(t)) - \sqrt{|\xi_0(0)|}\,{}_3\mathrm{F}_2(\xi_0^2(0))\right)\right.$$
$$-C_0A_1\left(\frac{\Omega_0(t)}{\sqrt{|\xi_0(t)|}}\,{}_3\mathrm{F}_2\left(1-\xi_0^2(t)\right) - \frac{\Omega_0(0)}{\sqrt{|\xi_0(0)|}}\,{}_3\mathrm{F}_2\left(1-\xi_0^2(0)\right)\right)$$
$$+\frac{\sqrt{2}}{2}A_1\left(u_0\ln(1-\xi_0^2(t)) - \varphi_0\ln(1-\xi_0^2(0))\right)$$
$$\left.-\sqrt{2}A_2\left(\mathrm{F}\left(\arccos\left(\sqrt{\frac{1-|\xi_0(t)|}{1+|\xi_0(t)|}}\right)\right)\ln\left(\sqrt{|\xi_0(t)|}\right)\right.\right.$$

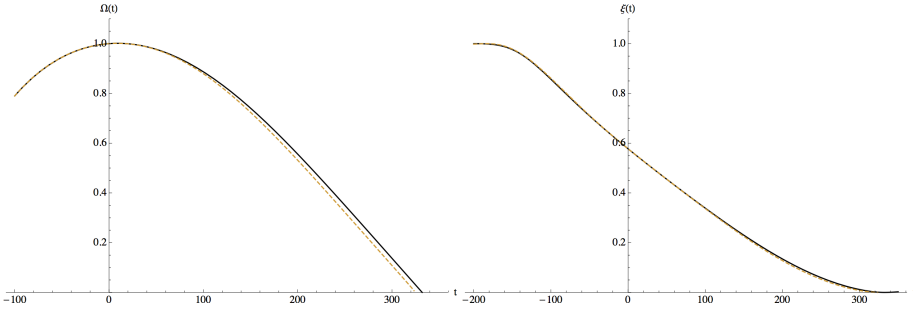

Figure 4.7 – Analytical solution (dashed line) for $\Omega(t)$ and $\xi(t)$ compared with numerical integration results (solid line). The initial conditions that were used are the same as in Fig. 4.6.

$$
\begin{aligned}
&-\mathrm{F}\left(\arccos\left(\sqrt{\frac{1-|\xi_0(0)|}{1+|\xi_0(0)|}}\right)\right)\ln\left(\sqrt{|\xi_0(0)|}\right)\\
&+\frac{C_0}{2}\left(\sqrt{2}w\left(-A_3\xi_0^2(0)-A_4\xi_0^4(0)-A_2\ln(|\xi_0(0)|)-A_1\ln(1-\xi_0^2(0))+\frac{5}{21}A_4\right.\right.\\
&\left.+\frac{1}{3}A_3+5A_5\right)t+\left(\frac{10}{21}A_4+\frac{2}{3}A_3+5A_6\right)(\Omega_0(t)-\Omega_0(0))\\
&\left.+\left(\frac{6}{21}A_4+5A_7\right)\left(\xi_0^2(t)\Omega_0(t)-\xi_0^2(0)\Omega_0(0)\right)\right),
\end{aligned}
\tag{4.5.43}
$$

where we skip the parameters of ${}_3\mathrm{F}_2$ hypergeometric functions for brevity.

The new $u(t)$ and $C(t)$ can be plugged into the quadrupole approximation solution (4.5.17, 4.5.14). The resulting analytical solution for $\Omega(t)$ and $\xi(t)$ yields trajectories very similar to that obtained numerically with the integration of (4.5.1, 4.5.2) with $n=3$ (Fig. 4.7).

4.5.2 Small wobble model

A small departure of the angular momentum vector from the principal axis already results in tumbling. Hereinafter, we keep $\Omega = G/I_3$ as a purely formal quantity, differing from the actual angular velocity by $\mathscr{O}(\eta^2)$.

We are interested in the dynamics in the vicinity of the principal axis. Using

$$\eta = \sin\theta, \tag{4.5.44}$$

with θ defined as in (4.2.9), we expand the equations (4.2.13)-(4.2.15) with $n=1$ around $\theta = 0$, keeping the terms up to η^3:

$$\frac{\mathrm{d}\Omega}{\mathrm{d}t} = \frac{\kappa^* P_2(\xi)}{2}\left(Z_{2,0}+\eta^2\left(-3Z_{2,0}+\alpha_0\left(3X_{2,1}+Z_{2,0}-3Z_{2,2}\right)\right)\right), \tag{4.5.45}$$

$$\frac{\mathrm{d}\xi}{\mathrm{d}t} = \frac{2\xi\left(1-\xi^2\right)}{\Omega\left(1-3\xi^2\right)}\frac{\mathrm{d}\Omega}{\mathrm{d}t}, \tag{4.5.46}$$

$$\frac{\mathrm{d}\eta}{\mathrm{d}t} = -\frac{2\eta}{\Omega}\left(\frac{\mathrm{d}\Omega}{\mathrm{d}t} + \frac{\kappa^* P_2(\xi)\,\eta^2 Z_{2,0}}{2\beta}\right), \tag{4.5.47}$$

where

$$\alpha_0 = \frac{a_1 - a_2}{a_1 - a_3}, \tag{4.5.48}$$

and

$$\beta^{-1} = \frac{10 - 3\alpha_0}{8} - \frac{3\alpha_0\,(X_{2,1} - Z_{2,2})}{2Z_{2,0}}. \tag{4.5.49}$$

The integral C remains valid in tumbling rotation (assuming Ω as defined above). The second integral is obtained by dividing (4.5.47) by (4.5.45),

$$\frac{\mathrm{d}\eta}{\mathrm{d}\Omega} = -\frac{2\eta}{\Omega} - \frac{\kappa^* \eta^3 P_2(\xi) Z_{2,0}}{\beta\Omega\dot{\Omega}}, \tag{4.5.50}$$

and neglecting the terms of $\mathscr{O}(\eta^2)$ in $\dot{\Omega}$

$$\frac{\mathrm{d}\eta}{\mathrm{d}\Omega} = -\frac{2\eta}{\Omega}\left(1 + \frac{\eta^2}{\beta}\right), \tag{4.5.51}$$

with the accuracy of $\mathscr{O}(\eta^5)$. After integration, this gives

$$\frac{\Omega^4\eta^2}{\beta + \eta^2} = \text{const}, \tag{4.5.52}$$

which can be approximated for small η as

$$B = \Omega^4\,\eta^2\left(1 - \frac{\eta^2}{\beta}\right). \tag{4.5.53}$$

The arbitrary constant B is the same integral as the one found by Breiter et al. (2011) without truncation in η.

Unfortunately, elimination of two of the three variables in any of the equations (4.5.45), (4.5.46) or (4.5.47) does not lead to a sufficiently simple solution.

4.5.3 YORP and inelastic energy dissipation

Adding the energy dissipation, the equation for η becomes

$$\frac{\mathrm{d}\eta}{\mathrm{d}t} = \eta E_1(\xi,\Omega) + \eta^3 E_3(\xi,\Omega), \tag{4.5.54}$$

whereas those for $\dot{\Omega}$ and $\dot{\xi}$ remain as in (4.5.45) and (4.5.46), respectively. E_1 and E_3 above are

$$E_1 = -\frac{\kappa^* P_2(\xi) Z_{2,0}}{\Omega} - \gamma\left[\frac{\mathrm{d}\tilde{\Psi}_3}{\mathrm{d}\eta}\right]_{\eta=0}, \tag{4.5.55}$$

$$E_3 = -\frac{\kappa^* P_2(\xi)}{\Omega}\left(\left(-3+\frac{1}{\beta}\right)Z_{2,0}+\alpha_0\left(3X_{2,1}+Z_{2,0}-3Z_{2,2}\right)\right)-\frac{\gamma}{6}\left[\frac{\mathrm{d}^3\tilde{\Psi}_3}{\mathrm{d}\eta^3}\right]_{\eta=0}, \tag{4.5.56}$$

with

$$\gamma = \frac{a^4 V \Omega^3 a_3^2}{\mu Q (a_2 - a_3)} = \frac{a^4 V \Omega^3 a_3}{\mu Q}\,\frac{1+h_1^2 h_2^2}{h_1^2\left(1-h_2^2\right)} \tag{4.5.57}$$

(as in Eq. (4.3.2)). Hereinafter, we use

$$\tilde{\Psi}_3 = \frac{\Psi_3}{\eta}. \tag{4.5.58}$$

The derivatives of odd orders at $\eta = 0$ of $\tilde{\Psi}_3$ are

$$\left[\frac{\mathrm{d}\tilde{\Psi}_3}{\mathrm{d}\eta}\right]_{\eta=0} = \frac{\left(1-h_2^2\right)^{\frac{5}{2}}\left(1-h_1^2h_2^2\right)^{\frac{3}{2}}}{\left(1+h_2^2\right)^{\frac{5}{2}}\left(1+h_1^2h_2^2\right)^{\frac{7}{2}}}\,\frac{M_{123}}{16}, \tag{4.5.59}$$

$$\left[\frac{\mathrm{d}^3\tilde{\Psi}_3}{\mathrm{d}\eta^3}\right]_{\eta=0} = \frac{3\left(1-h_2^2\right)^{\frac{5}{2}}\left(1-h_1^2h_2^2\right)^{\frac{1}{2}}}{64\left(1+h_2^2\right)^{\frac{5}{2}}\left(1+h_1^2h_2^2\right)^{\frac{9}{2}}}\left(4M_{012}-\left(7+5h_1^4-12h_1^4h_2^4\right)M_{123}\right.$$
$$\left.+2\left(1-h_1^4\right)^2 M_{13}\right), \tag{4.5.60}$$

whereas those of even orders vanish. M_{012} and M_{123} are

$$M_{012} = \left(1-h_1^4\right)^2\left(M_0+M_{12}\right), \tag{4.5.61}$$

$$M_{123} = \left(1-h_1^4\right)\left(M_{13}+M_{23}\right), \tag{4.5.62}$$

with M_0, M_{12}, M_{13} and M_{23} the positive functions of h_1, h_2 from Breiter et al. (2012).

4.5.4 Local stability criterion

The question is, what is the condition for the process of energy dissipation to overcome the tumbling-driving influence of the YORP effect? To answer this within the considered model assumptions, we set two limits: since we study small departures from the principal axis, we set $\eta_{\max} = 1/4$, which coincides with $\theta \approx 15\,^\circ$, the value below which tumbling rotation is observationally indistinguishable from the principal axis rotation. The other limit is related to averaging limits in the YORP model – the rotation cannot be slow enough to approach spin-orbit resonances. We therefore take $\Omega_{\min} = 10n$ (with n being the mean motion).

We can rewrite $\frac{\mathrm{d}\eta}{\mathrm{d}t}$ as a product of a common positive factor extracted from E_1 and E_3 and the remaining parts now labeled D_1 and D_3,

$$\frac{\mathrm{d}\eta}{\mathrm{d}t} = \frac{a_3 V \Phi_0 d_0^2 \eta}{\Omega c a^2 \left(1-e^2\right)^{\frac{1}{2}}}\left(D_1+\eta^2 D_3\right), \tag{4.5.63}$$

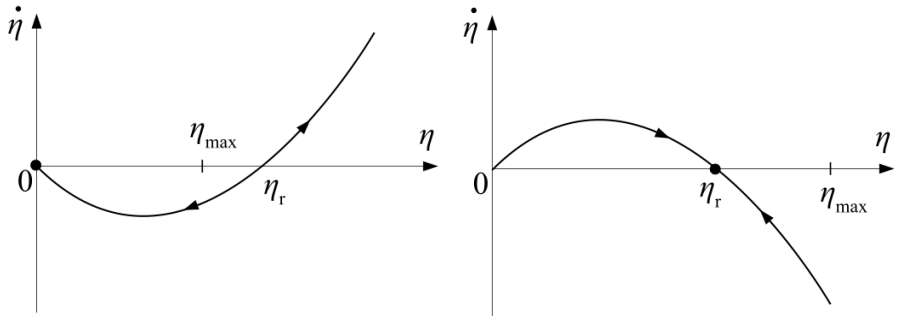

Figure 4.8 – Conditions for a local attractor.

with

$$D_1 = \left(\frac{1}{3} - \xi^2\right) Z_{2,0} - R\Omega^4 H_1, \tag{4.5.64}$$

$$D_3 = \left(\frac{1}{3} - \xi^2\right) \left(\frac{1}{\beta} + \frac{1}{\beta'}\right) Z_{2,0} - R\Omega^4 H_3. \tag{4.5.65}$$

The shape-related functions introduced above are

$$H_1 = \frac{\left(1-h_2^2\right)^{\frac{3}{2}} \left(1-h_1^2 h_2^2\right)^{\frac{3}{2}}}{h_1^2 \left(1+h_2^2\right)^{\frac{5}{2}} \left(1+h_1^2 h_2^2\right)^{\frac{5}{2}}} \frac{M_{123}}{16}, \tag{4.5.66}$$

$$H_3 = \frac{\left(1-h_2^2\right)^{\frac{3}{2}} \left(1-h_1^2 h_2^2\right)^{\frac{1}{2}}}{128 h_1^2 \left(1+h_2^2\right)^{\frac{5}{2}} \left(1+h_1^2 h_2^2\right)^{\frac{7}{2}}} \left(4M_{012} - \left(7+5h_1^4-12h_1^4 h_2^4\right) M_{123} \right.$$
$$\left. +2\left(1-h_1^4\right)^2 M_{13}\right), \tag{4.5.67}$$

and the positive coefficient R encapsulates all the constants

$$R = \frac{a_e^4 \rho^2 c \left(1-e^2\right)^{\frac{1}{2}}}{\mu Q \Phi_0} \left(\frac{a}{d_0}\right)^2. \tag{4.5.68}$$

The idea of stability that we employ here is illustrated in Fig. 4.8. In short, two attractors for η can exist in $0 \leq \eta < \eta_{\max}$. The two roots for $\frac{\mathrm{d}\eta}{\mathrm{d}t}$ are $\eta = 0$ and $\eta_r = \sqrt{-\frac{D_1}{D_3}}$ (D_1 and D_3 need to have opposite signs).

The first local stability criterion (Fig. 4.8, left) could be formulated as the requirement that for all $0 < \eta < \eta_{\max}$ and $\Omega > \Omega_{\min}$, we have

$$\dot{\eta} < 0. \tag{4.5.69}$$

Therefore, the derivative of (4.5.63) needs to be negative at $\eta = 0$. This is fullfilled if $D_1 < 0$ and $D_3 < 0$, but also, in case of $D_3 > 0$, we need to add $D_3 < -D_1/\eta_{\max}^2$, so

that the basin of attraction covers the whole postulated interval. We have thus

$$D_1 < 0, \text{ and } D_3 < -\frac{D_1}{\eta_{\max}^2}. \tag{4.5.70}$$

The first of them implies

$$\left(1-3\xi^2\right) Z_{2,0} < 3RH_1\Omega^4. \tag{4.5.71}$$

Substituting $\Omega = \Omega_{\min}$, we have a constant, positive factor on the right-hand side of the equation, but $(1-3\xi^2)$ on the left side still varies during the evolution. As long as $Z_{2,0}$ and $(1-3\xi^2)$ have opposite signs, the requirement is met unconditionally; otherwise, we need further restrictions. We can majorize or minorize the $(1-3\xi^2)$ factor by 1 or -2, respectively, depending on the sign of $Z_{2,0}$. We then have

$$-\frac{3}{2}RH_1\Omega_{\min}^4 < Z_{2,0} < 3RH_1\Omega_{\min}^4, \tag{4.5.72}$$

as the first part of the condition. $D_3 < -D_1/\eta_{\max}^2$ implies

$$\left(\frac{1}{\eta_{\max}^2}+\frac{1}{\beta'}+\frac{1}{\beta}\right)\left(1-3\xi^2\right) Z_{2,0} < 3R\left(\frac{H_1}{\eta_{\max}^2}+H_3\right)\Omega^4, \tag{4.5.73}$$

which, similarly to previous case, leads to

$$-\frac{3}{2}R\left(\frac{H_1}{\eta_{\max}^2}+H_3\right)\Omega_{\min}^4 < pZ_{2,0} < 3R\left(\frac{H_1}{\eta_{\max}^2}+H_3\right)\Omega_{\min}^4, \tag{4.5.74}$$

where

$$p = \frac{1}{\eta_{\max}^2}+\frac{1}{\beta'}+\frac{1}{\beta} = \frac{1}{\eta_{\max}^2}-\frac{7}{4}+\frac{5\alpha_0}{8}+\frac{3\alpha_0\left(X_{2,1}-Z_{2,2}\right)}{2Z_{2,0}}, \tag{4.5.75}$$

with a sign that is not predetermined.

The second condition (Fig. 4.8, right) corresponds to the other root of $\dot{\eta}$, and requires that for all $\eta < \eta_{\max}$ and $\Omega > \Omega_{\min}$, $\dot{\eta} > 0$, the root η_r exist and be smaller than $\eta_{\max}$. Accordingly, we need $D_1 > 0$, $D_3 < 0$, and $D_1 < -D_3/\eta_{\max}^2$. However, the first among these conditions, which translates to

$$\left(1-3\xi^2\right) Z_{2,0} > 3RH_1\Omega^4, \tag{4.5.76}$$

already excludes the applicability of this attractor due to the positive sign of the right-hand side. This means that it cannot be satisfied because $(1-3\xi^2)$ changes sign during its evolution.

Therefore, there is only one possible attractor to consider – the one related to $\eta = 0$. If we now try to evaluate the first condition, we have

$$3RH_1\Omega_{\min}^4 \approx \left[1.04\times10^{-17}\right]\left(\frac{a}{a_{\text{au}}}\right)^4\frac{\rho^2}{\mu Q}\sqrt{1-e_{\text{s}}^2}H_1, \tag{4.5.77}$$

where $a_{\rm au}$ is the semi-major axis expressed in astronomical units, and the remaining physical quantities are given in the SI units. Similarly, the second condition yields

$$\frac{3}{p}R\left(\frac{H_1}{\eta_{\rm max}^2}+H_3\right)\Omega_{\rm min}^4 \approx \left[1.04\times 10^{-17}\right]\frac{1}{p}\left(\frac{a}{a_{\rm au}}\right)^4\frac{\rho^2}{\mu Q}\sqrt{1-e_{\rm s}^2}\,(16H_1+H_3)\,. \tag{4.5.78}$$

Let us adopt the typical values of H_1 and H_3 of order 10^{-2}, and consider an exemplary irregularly shaped asteroid with $Z_{2,0}=0.01$, $X_{2,1}=0.0005$, $Z_{2,2}=0.001$, $\alpha_0=0.85$ and $\rho=2000$ kg m^{-3}, on an orbit with $a_{\rm au}=3$ au and $e_{\rm S}=0$. If we want to keep the commonly adopted value of $\mu Q=10^{11}$ Pa, the effective semi-axis of the ellipsoid corresponding to the asteroid would have to be as large as 1000 km in order to satisfy either of the conditions. For typical sizes of asteroids, $a\approx 10^4$ m, the damping factor μQ would have to be smaller than 10^4 Pa. These results seem to yet again be in disagreement with the observational evidence, as they suggest that the principal axis rotation is not stable.

4.6 Conclusions

In this chapter, we developed a perturbative theory of the YORP effect in both principal and non-principal axis rotation, including also the impact of nutation damping due to the dissipation of inelastic energy. The criterion for the stability of the principal axis rotation in presence of both factors that we formulated shows the PA rotation to be unstable if we consider the values of physical asteroid parameters that are regarded as typical; a body would have to be of improbable size to fulfill that stability requirement. This is clearly in disagreement with observational data which strongly suggest that most of Main Belt asteroids rotate around the shortest axis of their body figure. Therefore, we are not able to resolve this conundrum within the frame of the assumed model. One possibility is that the Rubincam's approximation is too restrictive in this case; including thermal conductivity would reduce the strength of the YORP effect in obliquity. Unfortunately, no YORP model with nonzero thermal conductivity in case of non-principal axis rotation exists so far.

Conclusions

Over the course of this thesis, several different topics were tackled, all belonging to the domain of the dynamics of small Solar System bodies – asteroids or space debris (clearly, space debris dynamics is also applicable to artificial satellites). More specifically, the considered problems could be divided into two domains: thermal effects and dynamics close to resonant tesseral and lunisolar surfaces, along with short discussion of the numerical integration issues related to the latter. One thing all these effects have in common is that they are mostly consequential on long timescales. As far as space debris studies are concerned, such problems are often overlooked as the nature of the subject focuses the attention on short-scale problems.

Long-term influence of the Yarkovsky-Schach effect was studied numerically on some exemplary orbits. Even though the effect is known to be minuscule, it should be accounted for in precise orbit determination studies, as well as on long timescales. It could be particularly relevant for objects on orbits close to resonant zones, where, much like the Poynting-Robertson effect described by Lhotka et al. (2016), it could slowly drive them inside the chaotic regions. With some favorable rotation periods, the effect in semimajor axis could be of several kilometers, or several degrees in orbit iclination, on such long timescales as 200 y.

In the region of medium Earth orbits, we studied several tesseral and lunisolar resonances. A set of MEGNO maps covering various initial conditions was produced, displaying nets of overlapping resonances and chaotic regions of limited predictability. The results were shown to be in accordance with some FLI maps drawn from literature. Better resolution of some of our MEGNO maps allows to discriminate more subtle features within the chaotic seas. Some stable regions that were previously found in Daquin et al. (2015) were also detected; they are most probably related to secondary resonances between overlapping harmonics. The issue is complicated as the amplitudes of these harmonics are of similar magnitude. Therefore, the problem cannot be attacked by measures of usual perturbation approach. Some methods that deal with such 2 degree-of-freedom Hamiltonian problems need to be applied.

The numerical simulations in MEO conducted for single orbits show that numerical trajectories are not accurately computed in long term and depend on the chosen

timestep. Some statistical features were considered and were shown to follow this tendency as well. This is the case for vicinities of both tesseral and lunisolar resonances. However, there is no discrepancy when stability information derived with the use of variational indicators is considered. This result confirms the robustness of the MEGNO criterion.

Lastly, we were interested in the rotational dynamics of asteroids under the YORP torque. The work presented in this thesis aimed to resolve some discrepancies between observational evidence and previous semi-analytical and numerical results. Considering both the YORP effect and inelastic energy dissipation in a tumbling motion, we developed an approximated model for small nutation angles. With it, we formulated some conditions for the principal axis rotation to be a local attractor, although its application to realistic physical parameters of asteroids did not allow for a resolution of the disagreement between observations and models. Most probably, a model of the non-principal axis rotation with the YORP effect and non-zero thermal conductivity could provide a further insight in this problem.

Each of these topics leaves open questions and perspectives. The Yarkovsky-Schach effect could be further developed in terms of more realistic rotation models that would evolve with time, possibly including rotational effects acting on space debris in Earth environment (including, among others, the YORP effect). The considered stability regions within the tesseral chaotic zones require some more advanced analytical treatment that could reveal interesting dynamics. The same could be said about some structures visible in lunisolar maps – some secondary resonances could probably be identified. This shows the complexity of motion in the behaviour of space debris and satellites. Finally, the YORP effect, now considered to be one of the main mechanisms to shape small Solar System bodies evolution of rotation state, is still at the early stages of its advancements, with many efforts still relying on considerable approximations. More realistic asteroids shapes and thermal properties could be considered in the future.

List of articles

During the course of this thesis, the following articles with author's contribution were produced:

- Breiter, S. and Murawiecka, M.. Perturbation approach to the YORP dynamics. *in preparation*
- Murawiecka, M. and Lemaitre, A.. The Yarkovsky-Schach effect on space debris motion. *Advances in Space Research*, 61:3, 935-940, 2018;
- Marciniak et al. (incl. Murawiecka, M.). Photometric survey, modelling, and scaling of long-period and low-amplitude asteroids. *Astronomy and Astrophysics*, 610, A7, 2018.
- Bartczak et al. (incl. Murawiecka, M.), A new non-convex model of the binary asteroid (809) Lundia obtained with the SAGE modelling technique. *MNRAS*, 471:1, 941-947, 2017;
- Devogèle et al. (incl. Murawiecka, M.). Shape and spin determination of Barbarian asteroids. *Astronomy and Astrophysics*, 607, A119, 2017;

Bibliography

G. Afonso, F. Barlier, M. Carpino, P. Farinella, F. Mignard, A. Milani, and A. Nobili. Orbital effects of LAGEOS seasons and eclipses. *Annales Geophysicae*, 7:501–514, October 1989.

A. Albuja. *Rotational Dynamics of Inactive Satellites as a Result of the YORP Effect*. PhD thesis, University of Colorado, 2015.

M. Allen. Introduction to molecular dynamics simulation. *Computational soft matter: from synthetic polymers to proteins*, 23, 2004.

W. F. Bottke, D. Vokrouhlický, M. Broz, D. Nesvorný, and A. Morbidelli. Dynamical Spreading of Asteroid Families by the Yarkovsky Effect. *Science*, 294(5547):1693–1696, 2001.

Y. Boudon, F. Barlier, A. Bernard, R. Juillerat, A. M. Mainguy, and J. Walch. Synthesis of Flight Results of the Cactus Accelerometer for Accelerations Below 10-9G. *Acta Astronautica*, 6:1387–1398, 11 1979. doi: 10.1016/0094-5765(79)90130-9.

S. Breiter. Lunisolar resonances revisited. *Celestial Mechanics and Dynamical Astronomy*, 81:81–91, 2001.

S. Breiter. Fundamental models of resonance. *Monografias de la Real Academia de Ciencias de Zaragoza*, 22:83–92, 2003.

S. Breiter and M. Murawiecka. Tumbling asteroid rotation with the YORP torque and inelastic energy dissipation. *Monthly Notices of the Royal Astronomical Society*, 449:2489–2497, May 2015. doi: 10.1093/mnras/stv433.

S. Breiter, I. Wytrzyszczak, and B. Melendo. Long-term predictability of orbits around the geosynchronous altitude. *Advances in Space Research*, 35:1313–1317, 2005.

S. Breiter, A. Rożek, and D. Vokrouhlický. Yarkovsky-O'Keefe-Radzievskii-Paddack effect on tumbling objects. *Monthly Notices of the Royal Astronomical Society*, 417:2478–2499, Nov. 2011.

S. Breiter, A. Rożek, and D. Vokrouhlický. Stress field and spin axis relaxation for inelastic triaxial ellipsoids. *Monthly Notices of the Royal Astronomical Society*, 427 (1):755–769, 2012.

Celestrak. Breeze-M Rocket Body (38746) Breakup. URL `https://celestrak.com/events/38746-Breakup/`. Accessed: 30.04.2019.

A. Celletti and C. Galeş. On the Dynamics of Space Debris: 1:1 and 2:1 Resonances. *Journal of NonLinear Science*, 24, 2014.

B. Chirikov. A universal instability of many-dimensional oscillator systems. *Physics reports*, 52(5):263–379, 1979.

S. Cicalò and D. J. Scheeres. Averaged rotational dynamics of an asteroid in tumbling rotation under the YORP torque. *Celestial Mechanics and Dynamical Astronomy*, 106:301–337, Apr. 2010. doi: 10.1007/s10569-009-9249-7.

P. Cincotta and C. Simó. Simple tools to study global dynamics in non-axisymmetric galactic potentials - I. *Astronomy and Astrophysics Supplement*, 147:205–228, 2000.

P. Cincotta, C. Giordano, and C. Simó. Phase space structure of multi-dimensional systems by means of the mean exponential growth factor of nearby orbits. *Physica D*, 182:151–178, 2003.

J. Daquin. *Essais sur le mouvement résonant à long terme des débris spatiaux*. PhD thesis, Observatoire de Paris, 2015.

J. Daquin, F. Deleflie, and J. Pérez. Comparison of mean and osculating stability in the vicinity of the (2:1) tesseral resonant surface. *Acta Astronautica*, 111:170–177, 2015.

J. Daquin, A. Rosengren, E. Alessi, F. Deleflie, G. Valsecchi, and A. Rossi. The dynamical structure of the MEO region: long-term stability, chaos, and transport. *Celestial Mechanics and Dynamical Astronomy*, 124:335–366, 2016.

N. Delsate. *Modélisation et analyse de la dynamique orbitale: équilibres, résonances et chaos*. PhD thesis, Université de Namur, 2011.

N. Delsate and A. Compère. NIMASTEP: a software to modelize, study and analyze the dynamics of various small objects orbiting specific bodies. *Astronomy and Astrophysics*, 540, April 2012.

A. Deprit and A. Elipe. Complete reduction of the Euler-Poinsot problem. *The Journal of the Astronautical Sciences*, 41(4):603–628, 1993.

M. Efroimsky. Precession of a freely rotating rigid body. Inelastic relaxation in the vicinity of poles. *Journal of Mathematical Physics*, 41(4):1854–1888, 2000.

T. Ely and K. Howell. Dynamics of artificial satellite orbits with tesseral resonances including the effects of luni-solar perturbations. *Dynamics and Stability of systems*, 12(4):243–269, 1997.

ESA. Space debris mitigation: the case for a code of conduct, a. URL `http://www.esa.int/Our\_Activities/Operations/Space\_debris\_mitigation\_the\_case\_for\_a\_code\_of\_conduct`. Accessed: 22.04.2019.

ESA. Space environment statistics, b. URL `https://sdup.esoc.esa.int/discosweb/statistics/`. Accessed: 24.04.2019.

ESA. Space debris by the numbers, c. URL `https://www.esa.int/Our\_Activities/Space\_Safety/Space\_Debris/Space\_debris\_by\_the\_numbers`. Accessed: 24.04.2019.

ESA. Space debris, d. URL `https://www.esa.int/Our\_Activities/Operations/Space\_Safety\_Security/Space\_Debris/About\_space\_debris`. Accessed: 24.04.2019.

P. Farinella and D. Vokrouhlický. Thermal force effects on slowly rotating, spherical artificial satellites - I. Solar heating. *Planetary Space Science*, 44(12):1551–1561, 1996.

P. Farinella, A. Nobili, F. Barlier, and F. Mignard. Effects of thermal thrust on the node and inclination of LAGEOS. *Astronomy and Astrophysics*, 234(1-2):546–554, 1990.

P. Farinella, D. Vokrouhlický, and W. K. Hartmann. Meteorite Delivery via Yarkovsky Orbital Drift. *Icarus*, 132(2):378–387, 1998.

C. Froeschlé, E. Lega, and R. Gonczi. The fast Lyapunov indicator: A simple tool to detect weak chaos. Application to the structure of the main asteroidal belt. *Planetary and Space Science*, 45(7):881–886, 1997.

I. Gkolias, J. Daquin, F. Gachet, and A. Rosengren. From order to chaos in Earth satellite orbits. *The Astronomical Journal*, 152(5), 2016.

O. Golubov and Y. N. Krugly. Tangential component of the YORP effect. *The Astrophysical Journal Letters*, 752(1):L11, 2012.

O. Golubov, D. J. Scheeres, and Y. N. Krugly. A three-dimensional model of tangential YORP. *The Astrophysical Journal*, 794(1), 2014.

K. Goździewski, E. Bois, A. Maciejewski, and L. Kiseleva-Eggleton. Global dynamics of planetary systems with the MEGNO criterion. *Astronomy and Astrophysics*, 378:569–586, 2001.

T. Henych and P. Pravec. Asteroid rotation excitation by subcatastrophic impacts. *Monthly Notices of the Royal Astronomical Society*, 432(2):1623–1631, 2013.

C. Hubaux. *Long term dynamics of space debris orbits including Earth's shadows*. PhD thesis, Université de Namur, 2013.

C. Hubaux, A. Lemaitre, N. Delsate, and T. Carletti. Symplectic integration of space debris motion considering several Earth's shadowing models. *Advances in Space Research*, 49(10):1472–1486, 2012.

S. Hughes. Earth satellite orbits with resonant lunisolar perturbations. I. Resonances dependent only on inclinations. *Proceedings of the Royal Society of London. A. Mathematical and Physical Sciences*, 372:243–264, 1980.

N. Johnson, E. Stansbery, D. Whitlock, K. Abercromby, and D. Shoots. History of on-orbit satellite fragmentations. Technical report, NASA, 2008.

M. Kaasalainen, J. Ďurech, B. D. Warner, Y. N. Krugly, and N. M. Gaftonyuk. Acceleration of the rotation of asteroid 1862 Apollo by radiation torques. *Nature*, 446 (22):420–422, 2007.

W. M. Kaula. *Theory of satellite geodesy: Applications of satellites to geodesy*. Waltham, Mass.: Blaisdell, 1966.

J. Lambert. Fengyun-1c debris cloud evolution over one decade. In *Advanced Maui Optical and Space Surveillance Technologies Conference*, 2018.

J. Laskar. Frequency analysis for multi-dimensional systems. Global dynamics and diffusion. *Physica D Nonlinear Phenomena*, 67:257–281, 1993.

A. Lemaitre, N. Delsate, and S. Valk. A web of secondary resonances for large A/m geostationary debris. *Celestial Mechanics and Dynamical Astronomy*, 104:383–402, 2009.

C. Lhotka, A. Celletti, and C. Galeş. Poynting-Robertson drag and solar wind in the space debris problem. *Monthly Notices of the Royal Astronomical Society*, 460: 802–815, July 2016.

S. C. Lowry, A. Fitzsimmons, P. Pravec, D. Vokrouhlický, H. Boehnhardt, P. A. Taylor, J.-L. Margot, A. Galád, M. Irwin, J. Irwin, and P. Kusnirák. Direct Detection of the Asteroidal YORP Effect. *Science*, 316, 2007.

S. C. Lowry, P. R. Weissman, S. R. Duddy, B. Rozitis, A. Fitzsimmons, S. F. Green, M. D. Hicks, C. Snodgrass, S. D. Wolters, S. R. Chesley, J. Pittichová, and P. van Oers. The internal structure of asteroid (25143) itokawa as revealed by detection of yorp spin-up. *Astronomy and Astrophysics*, 562(A48), 2014.

G. Métris, D. Vokrouhlický, J. Ries, and R. Eanes. Nongravitational effects and the LAGEOS eccentricity excitations. *Journal of Geophysical Research*, 102(B2): 2711–2729, 1997.

O. Montenbruck and E. Gill. *Satellite orbits: Models, methods, and applications*. Springer - Verlag, Berlin, Heidelberg, New York, 2000.

C. D. Murray and S. F. Dermott. *Solar System dynamics*. Cambridge University Press, 2000.

NASA. NASA space science data coordinated archive, a. URL `https://nssdc.gsfc.nasa.gov/nmc/spacecraft/display.action?id=1958-002B`. Accessed: 19.04.2019.

NASA. Frequently asked questions: space debris, b. URL `https://www.nasa.gov/news/debris\_faq.html`. Accessed: 22.04.2019.

D. Nesvorný and D. Vokrouhlický. Analytic theory for the Yarkovsky-O'Keefe-Radzievskii-Paddack effect on obliquity. *The Astronomical Journal*, 136:291–299, 2008.

NGA. Earth gravitational model 2008. URL `http://earth-info.nga.mil/GandG/wgs84/gravitymod/egm2008/`. Accessed: 25.04.2019.

J. O'Keefe. *Tektites and their origin*. Elsevier, 1976.

E. J. Öpik. Collision probabilities with the planets and the distribution of interplanetary matter. *Proc. R. Irish Acad. Sect. A*, 54:165–199, 1951.

S. Paddack. Rotational bursting of small celestial bodies: Effects of radiation pressure. *Journal of Geophysical Research*, 74(17):4379–4381, 1969.

S. Paddack and J. Rhee. Rotational bursting of interplanetary dust particles. *Geophysical Research Letters*, 2:365–367, 1975.

A. Petit. *Etude de populations observées ou synthétiques de débris spatiaux depuis les données jusqu'aux modèles*. PhD thesis, Université de Namur, 2017.

A. Petit and A. Lemaitre. The impact of the atmospheric model and of the space weatherdata on the dynamics of clouds of space debris. *Advances in Space Research*, 57 (11):2245–2258, 2016.

D. Portree and J. Loftus Jr. Orbital debris: A chronology. Technical report, NASA, 1999.

P. Pravec, P. Scheirich, Ď. J., J. Pollock, P. Kušnirák, K. Hornoch, A. Galád, D. Vokrouhlický, A. Harris, E. Jehin, J. Manfroid, C. Opitom, M. Gillon, F. Colas, J. Oey, J. Vraštil, D. Reichart, K. Ivarsen, J. Haislip, and A. LaCluyze. The tumbling spin state of (99942) Apophis. *Icarus*, 233:48–60, 2014.

J. Radtke, R. Domınguez-Gonzalez, S. Flegel, N. Sanchez-Ortiz, and K. Merz. Impact of eccentricity build-up and graveyard disposal Strategies on MEO navigation constellations. *Advances in Space Research*, 56:2626–2644, 2015.

V. Radzievskii. A mechanism for the disintegration of asteroids and meteoroids. *Astronomicheskii Zhurnal*, 29:162–170, 1952.

A. J. Rosengren, J. Daquin, K. Tsiganis, E. M. Alessi, F. Deleflie, A. Rossi, and G. B. Valsecchi. Galileo disposal strategy: stability, chaos and predictability. *Monthly Notices of the Royal Astronomical Society*, 464:4063–4076, 2017.

A. Rossi, L. Anselmo, C. Pardini, and R. Jehn. Effectiveness of the de-orbiting practices in the meo region. In E. S. Publication, editor, *Fifth European Conference on Space Debris*, volume 672, page 16, 2009.

D. P. Rubincam. LAGEOS orbit decay due to infrared radiation from Earth. *Journal of Geophysical Research*, 92:1287–1294, Februat 1987.

D. P. Rubincam. Radiative Spin-up and Spin-down of Small Asteroids. *Icarus*, 148: 2–11, Nov. 2000. doi: 10.1006/icar.2000.6485.

D. P. Rubincam. Zero secular torque on asteroids from impinging solar photons in the YORP effect: a simple proof. *Icarus*, 209:863–865, 2010.

Space.com. US Military satellite explosion caused by battery-charger problem, a. URL `https://www.space.com/29996-us-military-satellite-explosion-dmspf13-cause.html`. Accessed: 19.04.2019.

Space.com. India's Anti-Satellite Test Created Dangerous Debris, NASA Chief Says, b. URL `https://www.space.com/nasa-chief-condemns-india-anti-satellite-test.html`. Accessed: 10.08.2019.

T. Statler. Extreme sensitivity of the YORP effect to small-scale topography. *Icarus*, 202:502–513, 2009.

P. A. Taylor, J.-L. Margot, D. Vokrouhlický, D. J. Scheeres, P. Pravec, S. C. Lowry, A. Fitzsimmons, M. C. Nolan, S. J. Ostro, L. A. M. Benner, J. D. Giorgini, and C. Magri. Spin Rate of Asteroid (54509) 2000 PH5 Increasing Due to the YORP Effect. *Science*, 316, 2007.

K. Tsiganis, H. Varvoglis, and J. Hadjidemetriou. Stable chaos in high-order Jovian resonances. *Icarus*, 155(2):454–474, 2002.

P. Tupper. A conjecture about molecular dynamics. In *Mathematics and Computation, a Contemporary View*, pages 98–105. Springer, 2008.

D. Čapek and D. Vokrouhlický. The YORP effect with finite thermal conductivity. *Icarus*, 172:526–536, 2004.

J. Ďurech, D. Vokrouhlický, A. R. Baransky, S. Breiter, O. A. Burkhonov, W. Cooney, V. Fuller, N. M. Gaftonyuk, J. Gross, R. Y. Inasaridze, M. Kaasalainen, Y. N. Krugly, O. I. Kvaratshelia, E. A. Litvinenko, B. Macomber, F. Marchis, I. E. Molotov, J. Oey, D. Polishook, J. Pollock, P. Pravec, K. Sárneczky, V. G. Shevchenko,

I. Slyusarev, R. Stephens, G. Szabó, D. Terrell, F. Vachier, Z. Vanderplate, M. Viikinkoski, and B. D. Warner. Analysis of the rotation period of asteroids (1865) Cerberus, (2100) Ra-Shalom, and (3103) Eger - search for the YORP effect. *Astronomy and Astrophysics*, 547(A10), 2012.

P. Ševeček, M. Brož, D. Čapek, and Ď. J. The thermal emission from boulders on (25143) Itokawa and general implications for the YORP effect. *Monthly Notices of the Royal Astronomical Society*, 450:2104–2115, 2015.

S. Valk, N. Delsate, A. Lemaitre, and T. Carletti. Global dynamics of high area-to-mass ratios GEO space debris by means of the MEGNO indicator. *Advances in Space Research*, 43(10):1509–1526, 2009.

D. Vokrouhlický and W. F. Bottke. Yarkovsky and YORP effects, 2010. URL `http://www.scholarpedia.org/article/Yarkovsky_and_YORP_effects`. Accessed: 12.04.2019.

D. Vokrouhlický and D. Čapek. YORP-induced long term evolution of the spin state of small asteroids and meteoroids: Rubincam's approximation. *Icarus*, 159:449–467, 2002.

D. Vokrouhlický, D. Nesvorný, and W. F. Bottke. The vector alignments of asteroid spins by thermal torques . *Nature*, 425(6954):147–151, 2003.

D. Vokrouhlický, S. Breiter, D. Nesvorný, and W. F. Bottke. Generalized YORP evolution: onset of tumbling and new asymptotic states. *Icarus*, 191:636–650, 2007.

D. Vokrouhlický, W. F. Bottke, S. Chesley, D. J. Scheeres, and T. Statler. The Yarkovsky and YORP effects. In P. Michel, F. E. DeMeo, and W. F. Bottke, editors, *Asteroids IV*. University of Arizona Press, 2015.

K. J. Walsh and S. Jacobson. Formation and evolution of binary asteroids. In P. Michel, F. E. DeMeo, and W. F. Bottke, editors, *Asteroids IV*. University of Arizona Press, 2015.

K. J. Walsh, D. Richardson, and P. Michel. Rotational breakup as the origin of small binary asteroids . *Nature*, 454(7201):188–191, 2008.

B. Weeden. 2009 Iridum-Cosmos collision factsheet. Technical report, November 2010.

S. Wiggins and J. Ottino. Foundations of chaotic mixing. *Philosophical Transactions of the Royal Society of London A: Mathematical, Physical and Engineering Sciences*, 362(1818):937–970, 2004.

I. Yarkovsky. The density of luminiferous ether and the resistance it offers to motion (in Russian). self-published by the author, 1901.